Wearable Torso Exoskeletons for Human Load Carriage and Correction of Spinal Deformities

Joon-Hyuk Park

Submitted in partial fulfillment of the
requirements for the degree of
Doctor of Philosophy
in the Graduate School of Arts and Sciences

COLUMBIA UNIVERSITY

2016

ABSTRACT

Wearable Torso Exoskeletons for Human Load Carriage and Correction of Spinal Deformities

Joon-Hyuk Park

The human spine is an integral part of the human body. Its functions include mobilizing the torso, controlling postural stability, and transferring loads from upper body to lower body, all of which are essential for the activities of daily living. However, the many complex tasks of the spine leave it vulnerable to damage from a variety of sources. Prolonged walking with a heavy backpack can cause spinal injuries. Spinal diseases, such as scoliosis, can make the spine abnormally deform. Neurological disorders, such as cerebral palsy, can lead to a loss of torso control. External torso support has been used in these cases to mitigate the risk of spinal injuries, to halt the progression of spinal deformities, and to support the torso. However, current torso support designs are limited by rigid, passive, and non-sensorized structures. These limitations were the motivations for this work in developing the science for design of torso exoskeletons that can improve the effectiveness of current external torso support solutions. Central features to the design of these exoskeletons were the abilities to sense and actively control the motion of or the forces applied to the torso. Two applications of external torso support are the main focus in this study, backpack load carriage and correction of spine deformities. The goal was to develop torso exoskeletons for these two applications, evaluate their effectiveness, and exploit novel assistive and/or treatment paradigms.

With regard to backpack load carriage, current torso support solutions are limited and do not provide any means to measure and/or adjust the load distribution between the shoulders and the pelvis, or to reduce dynamic loads induced by walking. Because of these limitations,

determining the effects of modulating these loads between the shoulders and the pelvis has not been possible. Hence, the first scientific question that this work aims to address is *What are the biomechanical and physiological effects of distributing the load and reducing the dynamic load of a backpack on human body during backpack load carriage?*

Concerning the correction of spinal deformities, the most common treatment is the use of a spine brace. This method has been shown to effectively slow down the progression of spinal deformity. However, a limitation in the effectiveness of this treatment is the lack of knowledge of the stiffness characteristics of the human torso. Previously, there has been no means to measure the stiffness of human torso. An improved understanding of this subject would directly affect treatment outcomes by better informing the appropriate external forces (or displacements) to apply in order to achieve the desired correction of the spine. Hence, the second scientific question that this work aims to address is *How can we characterize three dimensional stiffness of the human torso for quantifiable assessment and targeted treatment of spinal deformities?*

In this work, a torso exoskeleton called the Wearable upper Body Suit (WEBS) was developed to address the first question. The WEBS distributes the backpack load between the shoulders and the pelvis, senses the vertical motion of the pelvis, and provides gait synchronized compensatory forces to reduce dynamic loads of a backpack during walking. It was hypothesized that during typical backpack load carriage, load distribution and dynamic load compensation reduce gait and postural adaptations, the user's overall effort and metabolic cost. This hypothesis was supported by biomechanical and physiological measurements taken from twelve healthy male subjects while they walked on a treadmill with a 25 percent body weight backpack. In terms of load distribution and dynamic load compensation, the results showed reductions in gait and postural adaptations, muscle activity, vertical and braking ground reaction forces, and

metabolic cost. Based on these results, it was concluded that the wearable upper body suit can potentially reduce the risk of musculoskeletal injuries and muscle fatigue associated with carrying heavy backpack loads, as well as reducing the metabolic cost of loaded walking.

To address the second question, the Robotic Spine Exoskeleton (ROSE) was developed. The ROSE consists of two parallel robot platforms connected in series that can adjust to fit snugly at different levels of the human torso and dynamically modulate either the posture of the torso or the forces exerted on the torso. An experimental evaluation of the ROSE was performed with ten healthy male subjects that validated its efficacy in controlling three dimensional corrective forces exerted on the torso while providing flexibility for a wide range of torso motions. The feasibility of characterizing the three dimensional stiffness of the human torso was also validated using the ROSE. Based on these results, it was concluded that the ROSE may alleviate some of the limitations in current brace technology and treatment methods for spine deformities, and offer a means to explore new treatment approaches to potentially improve the therapeutic outcomes of the brace treatment.

Table of Contents

List of Figures

List of Tables

Acknowledgments

First and foremost, I would like to express my sincere gratitude to my advisor and mentor, Professor Sunil Agrawal, for the invaluable guidance, scholarly input and consistent encouragement I received throughout my Ph.D. research. His support and advice have helped me overcome many hurdles and challenges during my study and made it possible to complete this dissertation. I was extremely lucky to meet him, as he has been a great mentor both for my academic and personal life. I will never forget his kindness, enthusiasm and encouragement.

I would like to thank my committee members Dr. Jeffery Kysar, Dr. Gerald Ateshian, Dr. Andrew Gordon, and Dr. David Roye for reviewing my work and giving me constructive feedback. I also want to thank them for making my defense an enjoyable experience. I am especially grateful for Dr. David Roye, as his advice was invaluable at various phases of the Robotic Spine Exoskeleton research.

I would like to thank all my lab members in the Robotics and Rehabilitation Laboratory for their wonderful suggestions and help on my research, especially Dr. Damiano Zanotto, Dr. Vineet Vashista, Paul Stegall, Xin Jin, Jiyeon Kang, Emily Boggs, Moiz Khan, Zhiyu Sheng, Rosemarie Murray, Daisuke Tajima, Brian Bradley, Haohan Zhang, and Onur Denizhan. I am especially grateful for Paul Stegall who has been very kind and helpful and always willing to lend a hand whenever I approached him, and I acknowledge and appreciate him for all his time and efforts. I also want to thank Rosemarie Murray, Riancy Li, Emily Boggs, and Moiz Khan for being kind enough to proofread my dissertation and provide helpful comments.

I would also like to thank Prachi Backrania, Kelly Grimes, Dr. Anna-Christina Bevelaqua, and John Tunney for their advice and help in conducting experiments with scoliosis patients. I am thankful for Dr. Charles Kim and his team for our collaboration on the Robotic Spine Exoskeleton project over the past few years. I am also thankful for Shashank Sharma, Dr. John Tierney, Dr. Shridhar Yarlagadda, and Dr. John Gillespie for our collaboration on the DARPA Warrior Web project.

I gratefully acknowledge the funding sources that made my Ph.D. work possible: the NASA/DESGC graduate fellowship (NNX10AN63H), with grants from the Defense Advanced Research Projects Agency (W911QX-12-C-0042) and the National Science Foundation (NSF IIS-1527087).

I want to thank the staff of the Mechanical Engineering department for their kind support. I particularly thank Sandra Morris, Jean Cadet, and Melbourne Francis for their administrative help with my academics, Rakhi Hossain for getting countless orders through, and Robert Stark and Mohammed Haroun for their assistance in the fabrication of mechanical components for my research.

Most of all, I am forever indebted to my parents Seongik Park and Heeyeon Lee, my sister Yoonjoo Park, my parents-in-law Taekil Kim and Eunsook Yoo, and my sister-in-law Mary Kim. Their almost unbelievable support, prayers, and love have given me strength to carry out this task, and I dedicate my thesis to them.

Finally, words cannot express how grateful I am to my dearest wife Minhee Kim who has been loving, supportive, encouraging, and patient and I appreciate every moment that we have had together. None of this would have been possible without her patience and love, and I can't thank her enough. I also want to thank my beloved son David Sunghyun Park for just being a

sweet little boy who has filled me up with happiness and laughter, and my unborn son Noah for coming into my life as a surprise whom I can't wait to meet.

Above all, I owe it all to my God for granting me the faith, wisdom, health, and strength to undertake this research task and see it through to completion. He has been leading my life and forever will be. I thank you lord for all that you have given to me. Thank you.

Chapter 1

Introduction

The human spine is a versatile and fascinating structure. It serves as a pillar to support the body's weight and external load; protects the spinal cord, nerves and vertebral artery; acts as a natural damper to absorb and distribute shock/load; allows for mobility and flexibility of torso to perform activities of daily living; and maintains balance and postural stability of the body [1, 2, 3, 4, 5]. However, perhaps of the complex structure needed to achieve both rigidity and flexibility for these functions, it is also vulnerable to damage, which can diminish these functions. This can come in the form of spinal injuries, as from prolonged walking with a heavy backpack. It can also come from spinal diseases, such as scoliosis, causing spinal deformities. Neurological diseases, such as cerebral palsy, and spinal cord injury can cause a loss of torso control.

External torso support is needed in these cases to mitigate the risk of spinal injuries, to curtail the progression of spinal deformities, and to support the torso. However, current torso support solutions are limited by rigid, passive, and non-sensorized designs. The main focus of this work is, therefore, to develop the science for design of torso exoskeletons that alleviate these limitations in two domains, backpack load carriage and correction of spine deformities; to evaluate their effectiveness in these applications; and explore novel assistive and/or treatment paradigms.

Regarding the first domain, walking with a heavy backpack increases the risk of musculoskeletal injuries, muscle fatigue, and metabolic cost [7-20]. This is due to the static and

dynamic load of a backpack on human body that compresses the spine and torso from the shoulders, and increases the lower limb joint torque necessary to compensate for the dynamic loads of a backpack. *By distributing the load between the shoulders and the pelvis, and reducing the dynamic load of a backpack during walking, some of these issues can be attenuated.*

Concerning the second domain, various musculoskeletal diseases can cause the human spine to develop abnormal curves. A typical treatment method to correct spinal deformities is the use of torso braces. These braces are generally constructed of a single rigid plastic shell, which imposes several limitations on the current brace treatment method and its outcomes. *By sensing and actively controlling either the position or the forces of the brace as it corrects the spinal curve, some of these limitations can be addressed.*

This work will incorporate these two features into two different torso exoskeleton designs: the Wearable upper Body Suit (WEBS) and the Robotic Spine Exoskeleton (ROSE), present the experimental evaluations on the functions facilitated in each, and discuss their practical implications and potential benefits to human load carriage and spinal deformity correction applications.

In this chapter, issues related to backpack load carriage are reviewed, and both current solutions and their limitations are presented. The motivation and rationale behind the work on the torso exoskeleton design for backpack load carriage is followed. Then, scoliosis, a spine disease causing spinal deformity, is introduced. Current bracing treatment methods and their limitations are addressed to motivate the work on the torso exoskeleton for correction of spinal deformities. The chapter concludes with an overview of subsequent chapters.

1.1 Backpack load carriage: issues and solutions

For most human beings, from school children to fire fighters to military personnel, load carriage is part of daily life. In most cases the load is supported on the shoulders or the back, as shown in Figure 1.1. For a long time, backpacks have been a common way of carrying load. However, walking with a heavy backpack can lead to increased orthopedic injuries, fatigue and metabolic cost. School children on average bear loads of up to 38% of their body weight (BW), a level of which higher chances of muscle fatigue and lower back pain can be associated [6, 7, 8, 9]. Prevalence of lower back pain is higher for people that carry heavy loads on a regular basis, e.g., a USA Marine rifleman's assault load can weigh between 57% - 79% BW, well above the threshold for injury [10]. In 2014, more than 28,100 individuals were treated for backpack related injuries, and more than 8,300 of those injuries were children age between 5 and 18 in the United States [11]. Despite these well-known issues associated with backpack load carriage, current engineering solutions are still limited to the following two strategies: distributing the load across different areas of the torso, or using lower limb devices that either to transfer the load directly to the ground or to provide joint torques to reduce the lower limb muscle work. In the following sections, the effects of backpack load on human walking and related issues are presented. Then, the limitations of the aforementioned strategies are discussed to justify the need for a torso exoskeleton for assisting in backpack load carriage.

Figure 1.1 (top) Human load carriages using a backpack, (bottom) other human load carriages without using a backpack

1.1.1 Issues related to backpack load carriage

Carrying a heavy backpack can increase the risk of musculoskeletal injuries. Such injuries occur on both the upper body (rucksack palsy, lower back pain, spasm, disc tear/herniation, spinal stenosis) and the lower limbs (foot blisters, metatarsalgia, stress fractures, and knee pain) [12, 13, 14, 15, 16, 17, 18]. Higher metabolic costs [19, 20, 21], increased muscle activity and fatigue [15, 22, 6, 23, 24, 25, 26], changes in gait and posture [17, 18, 27, 28, 29, 30], and increased ground reaction forces [15, 16, 17, 28, 31, 30] are typically reported with human load carriage. Injuries on the upper body are mainly caused by accumulated stress on spine and lumbar muscles required to support the additional loads on the shoulders and to maintain postural stability while walking [15, 18, 21]. Lower limb injuries are mainly caused by changes in gait kinematics to compensate for the vertical accelerations of the backpack and the resulting dynamic loads [12, 14, 16, 17]. Human walking can be modeled as an inverted pendulum that induces vertical motions of the pelvis and upper body [32, 33]. Over-ground walking generates vertical accelerations of

the head, thorax and pelvis, with peak accelerations about $\pm 2 \mathrm{m/s^2}$ [34]. These accelerations are periodic functions with roughly twice the frequency of the human gait. The backpack, which is tightly attached to the upper body, undergoes similar vertical motions. Therefore, the periodic vertical accelerations of the backpack exert dynamic loads on the body, in addition to a static load, which is about 20% of the static load for over-ground walking [34].

These static and dynamic loads alter normal gait and posture, and require greater lower limb muscle effort as the human body needs to compensate for the additional forces exerted on it. These effects are most significant during the weight acceptance and the push-off phases of the gait when the body is required to decelerate and accelerate the backpack load. Previous studies have reported the following body adaptations in kinematics and muscle kinetics as a result of a backpack load: higher stance-phase peak knee flexion, reduced swing phase, longer double support phase, increased ankle dorsi/plantar flexion and higher muscle activity in the lower extremities during the weight acceptance and push-off phases [13, 15, 17, 22, 29, 35]. These gait adaptations combined with the increase in lower limb muscle activity reflect the body's attempt to dampen the increased impact forces, due to added mass, at initial contact (heel strike) and to acquire more time to transfer the load between the legs during weight acceptance. Consequently, metabolic rate, muscle fatigue, and ground reaction forces increase with the load. Walking with a backpack has also been found to increase the forward lean of the trunk to maintain the combined center of mass (COM) of the upper body and carried load over the support polygon made by the feet. While such adaptations are necessary to achieve postural stability during loaded walking, it has been hypothesized that it causes foot strain, injury of the legs, and back injuries [12, 13, 14].

The dynamics of the backpack in human load carriage has been studied. Ren *et al.* [36] investigated the load carriage dynamics using a test-rig that simulates different backpack

suspension characteristics in human walking. They reported that by decreasing the suspension stiffness, it is possible to lower the peak vertical force exerting on the torso. This can also potentially decrease the lower limb joint loads. Foissac *et al.* [37] reported reduction in oxygen consumption when the vertical excursion of the backpack is reduced. Lower vertical excursion of the backpack has implications in reduced pressure on the shoulders at the shoulder straps and reduced forces transferred to the waist belt and the lower limbs. Similar results were also shown where the energy expenditure in human load carriage is strongly influenced by the vertical forces exerted [38] and the vertical motion of the body's center of mass [39, 40].

1.1.2 Strategies to assist backpack load carriage and their limitations

The first strategy to alleviate the issues of backpack load carriage is distributing the load across different areas of the torso, such as between the anterior and posterior of the torso or between the shoulders and the waist. It has been shown that locating the load mass close to the body's COM, e.g., by means of double-packs, Figure 1.2(d), results in lower metabolic cost [41] and lower postural deviations from natural walking [17, 42, 43]. This brings the load closer to the normal human COM and allows for a more natural posture without requiring additional stabilizing muscle activation. However, double-packs hinder arm and trunk movements more than backpacks, restrict the field of vision, and even induce ventilatory impairments and heat stress symptoms [35, 44]. Due to these issues, double-packs are not widely used.

Backpacks featuring a frame and a hip belt, Figure 1.2(e), are currently the most viable solution. They have been shown to alleviate stress on the shoulders and decrease lower back pain by partially transferring the load to the hips [12, 14, 21], even though the effectiveness depends on the specific backpack model. Decreased pressures on the shoulders may not only reduce

shoulder discomfort and the nerve compressions that cause rucksack palsy [14], but also reduce the stress on the spine since the rigid structure of the backpack acts as an alternative pathway for transferring loads to the lower body. Moreover, there is less work required for the trunk muscles to stabilize the posture as the net load carried on the shoulders is reduced by partially transferring it to the waist. External load bearing devices that have a similar function of distributing the backpack load between the shoulders and the waist have also been developed. For example, *Exospine* from Emerald Touch, Figure 1.2(f), was designed for situations where significant loads have to be carried outside the backpack (e.g., a military tactical vest weighs up to 13.6kg, nearly 18 % BW [10]) or for carrying loads directly over the shoulders (e.g., moving boxes or construction materials, or other person) [45, 46]. However, none of these backpack load distribution designs incorporates a mechanical design to measure or adjust the load distribution.

The second strategy to alleviate issues of backpack load carriage is to use lower limb exoskeletons, Figure 1.2(a)-(c), e.g., BLEEX from Berkeley Bionics [47]. These designs utilize a rigid leg exoskeleton attached directly to a backpack frame such that the load bypasses the human body and is transferred directly to the ground. This method may effectively reduce the net load carried by the body, but it requires adding rigid structures and joints on the lower limbs which may add bulk and weight to the lower limbs.

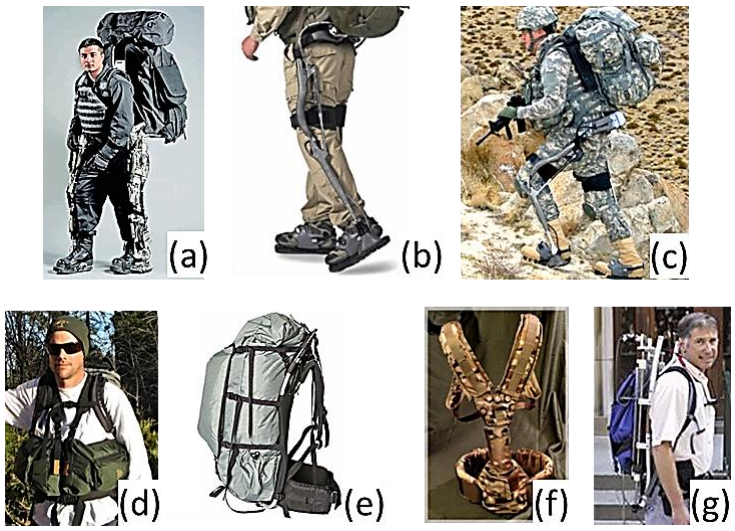

Figure 1.2 (a) BLEEX from Berkeley Bionics, (b) ExoHikers from Berkeley Bionics, (c) HULC from Lockheed Martin, (d) double-pack, (e) backpack frame with a hip belt, (f) *Exospine* from Emerald Touch, and (g) *Lightning Pack*

Another approach that attempts to reduce the dynamic loads of a backpack is to impose differential motions between the backpack and the body by designing a "suspended-load" backpack in which the load is suspended by an elastic cord on the backpack frame. It has been shown to passively reduce the accelerative force of a backpack and lower the associated metabolic cost, Figure 1.2(g), [38]. However, this concept can only be realized through a customized backpack design hence its applicability for general backpack load carriage or other load carriages without using a backpack is limited.

1.1.3 Needs for a torso exoskeleton for human load carriage

These previous studies and efforts in backpack load assistive strategies point out several features that have been targeted to alleviate issues in backpack load carriage. One of the features is the distribution of the backpack load between the shoulders and the waist - this may help relieve

stress on the shoulders and lower back. Another feature is dynamic load compensation of a backpack - this may decrease the lower limb joint loads and muscle efforts. Nevertheless, these features are not yet fully incorporated in any of the current load assistive devices. They are particularly lack sensing and adjusting capabilities of the load distribution between the shoulders and the waist, and cannot actively compensate for the dynamic load based on human motion. Consequently, there is a breach in understanding as to biomechanical and physiological effects of load distribution and dynamic load compensation of a backpack on human body.

Therefore, the first aim of this work is to develop a torso exoskeleton that facilitates load distribution and dynamic load compensation features, and to provide experimental evaluation of the effects of these features on the human body. For this aim, three different designs of torso exoskeletons (Second Spine, Motorized Second Spine, and Wearable upper Body Suit) were prototyped to reduce the body's compensations and the user's effort in backpack load carriage with the following aims: (i) distribution of the external load between the shoulders and the pelvis to reduce postural adaptation while relieving stress on the shoulders and the lower back, and (ii) compensation of the dynamic loads of a backpack by providing external assistive forces to reduce lower limb muscle use. Furthermore, real-time measurement and control of the backpack load exerted on the body were targeted features by which the assistive forces could be regulated for various gait and backpack load conditions. Each version has varying designs but they share the same basic functionality, i.e., measuring and adjusting the load distribution between the shoulders and the waist.

The first design was named "Second Spine" because it adds an alternative load pathway in addition to the human spine which can passively adjust the load transferred from the shoulders to the waist. The second design, Motorized Second Spine, has the same feature of the Second

Spine but with added functionality of dynamic load compensation through incorporating motors, sensors and real-time controllers. The third design, Wearable upper Body Suit (WEBS), improved the portability and wearability of the Motorized Second Spine, presented in detail in Chapter 2. A human subject study was conducted to evaluate the effects of load distribution and dynamic load compensation on backpack load carriage using the wearable upper body suit, presented in Chapter 3.

1.2 Spinal deformities: cause and treatment

1.2.1 *Scoliosis*, a spinal deformity

Spinal deformity occurs when there is unnatural curvature of the spine, as in scoliosis or kyphosis and Scheuermann's disease [48]. It also occurs due to defect (e.g. spondylolisthesis) or damage to the spine [48]. Scoliosis is one of the most common spinal deformities characterized by side-to-side abnormal curvatures of the spine [49]. In the United States, 1-3% of adolescents suffer from idiopathic scoliosis each year [50], and 30,000 children are prescribed braces to treat scoliosis while 38,000 patients undergo spinal fusion surgery [49]. On an x-ray taken from the back, the spine of a person with scoliosis looks more like a "C" or a "S" curve than a straight line. Cobb angle, which refers to the measurement of coronal plane deformity on anteroposterior plane radiographs [51], of 10 degrees or more are diagnosed as scoliosis [52, 50].

This disorder usually appears during adolescent years of growth and progresses until skeletal maturity. More than 80 % of scoliosis is idiopathic, meaning "of undetermined cause" [53]. The remaining 20% of scoliosis is due to congenital spinal column abnormalities, neurologic disorders, genetic conditions, and others [54]. Girls and boys are equally affected by

less severe degrees of scoliosis. Girls however are eight times more likely than boys to develop progressive curves [55, 56]. Such abnormal curves can make the individual's shoulders or waist appear uneven, Figure 1.3. The bones may also be rotated, making one shoulder blade more prominent than the other. It also impacts the quality of life of those affected by limiting their activity, causing pain, reducing respiratory function, and diminishing self-esteem [49]. Severe scoliosis (Cobb angle > 40~45°) can be associated with diminished digestive, hormonal, musculoskeletal and neurological function of the body; spinal fusion is recommended in these severe cases [50, 57], Figure 1.3.

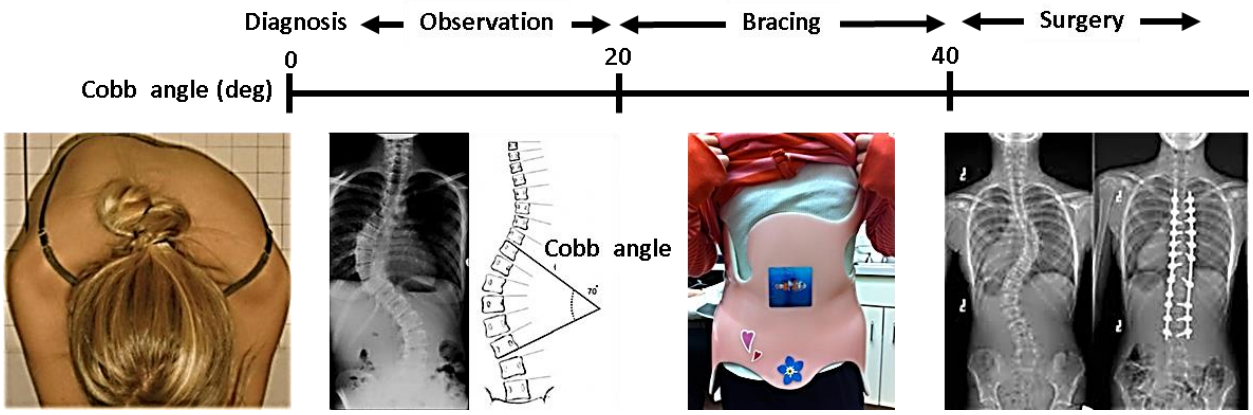

Figure 1.3 Treatment options based on the Cobb angle

1.2.2 Bracing treatment and its limitation

The predominant non-invasive treatment for scoliosis is bracing. A scoliosis brace is typically a rigid plastic shell that fits around the trunk and hips and applies counter-pressure on the abnormal curves of the spine. A typical TLSO (thoraco-lumbo-sacral orthosis) brace is recommended to be worn for up to 18 to 23 hours a day to restore spine alignment. The principle

behind clinical treatment with the brace is that external pressure and support on the curve stimulates more normal growth of the spine inside the body over time [58, 59, 60], which curtails curve progression and thereby mitigates the need for surgery. While bracing has long been a widely accepted practice in treating scoliosis, systematic and randomized group studies on the effectiveness of spine braces have been performed only recently [61]. The results clearly showed that braces help to reduce the progression of abnormal spine curves in adolescents. There was also a significant positive association between hours of brace wear and rate of treatment success. This study justifies scientifically the need for scoliosis intervention with braces.

There are several types of standard scoliosis braces each with slightly varying designs and functions [62, 63, 64, 65], as shown in Figure 1.4(a)-(d). They are all composed of either a single rigid body or multiple bodies rigidly connected to each other. The Milwaukee brace, Figure 1.4(a), was first developed in 1946 [66, 65]. It applies traction on the spine through a steel and leather pelvic base from which one anterior and two posterior arms extend to support the head at the occiput and throat. De-rotational forces are applied at the points of rib prominence through pads attached to the pelvic girdle. This class is no longer used in North America because of its abnormal effect on jaw growth [59]. The Charleston bending brace, Figure 1.4(b), was developed in 1978 to be used primarily during night-time to address compliance issues in patients with scoliosis for whom other treatment options had failed [64, 67, 68, 69]. The Charleston brace operates on the principle that passive bending of the spine without traction can promote correction of spinal deformity by inducing stretching forces on the concavity of the curve and compression at the convexity [64]. The Boston brace, Figure 1.4(c), has gained popularity due to its low profile, ease of application, and high patient satisfaction and compliance [70, 71, 62]. It consists of a prefabricated plastic brace with various sizes of paddings to correct

deformities in lumbar, thoraco-lumbar, and thoracic regions of the spine. It applies 3-point-pressure with rotation [62]. The Cheneau brace, Figure 1.4(d), consists of multiple molded rigid pieces which are screwed on to a central backbone rod to maintain an overall normal curvature of the spine. A 3-point-pressure pushes the peak of the abnormal curve inwards while holding at the two ends [72, 73]. The general principle of correction is de-torsion and sagittal plane normalization.

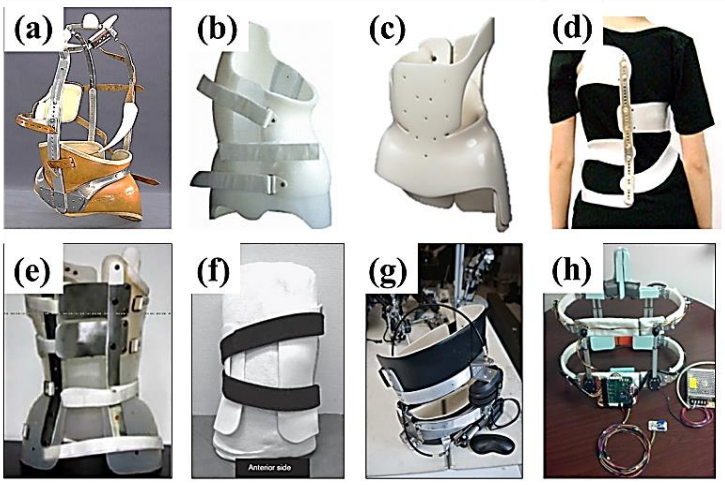

Figure 1.4 (top) Various types of scoliosis brace: (a) Milwaukee [65], (b) Charleston [64], (c) Boston [62], (d) Cheneau [63], and (bottom) (e) Dynamic Derotational Brace (DDB) [74, 75], (f) Dynamic Spinal Brace (DSB) [76], (g) A Hybrid Neuroprosthesis for walking with SCI [77], and (h) ExMS-1 from ExoDynamics [78]

Though these braces differ in their designs and principles, they all share the same goal to correct or stop the progression of abnormal curvature of the spine. However, the underlying brace technology used in these braces has not significantly changed over the last 50 years and still remains archaic because of the following limitations: (i) They are rigid and typically restrict normal activities of daily living (ADL) and are uncomfortable, which makes it difficult to wear for extended periods of time and leads to poor user compliance; (ii) They are passive and

incapable of active modulation or control of corrective forces; (iii) They are static which makes them incapable of adapting to changes in the spine over the course of treatment; (iv) They achieve spine correction by reconfiguring the posture of the torso without knowing how much force is being applied, which could cause undesirable deformation to the bone structure or excessive localized forces on the skin; (v) They do not provide real-time data on the torso that can be used for patient monitoring, data mining, or planning of the clinical treatment. To address some of these limitations and allow for greater mobility, the SpineCor brace was recently proposed which uses a series of elastic straps to correct the curvature [79, 80]. However, this brace showed varying levels of success, and requires extensive training to provide appropriate correction [81] hence, it has not been widely adopted by orthotists. Even with increased mobility, the force application is still passive and cannot be measured.

There have been limited efforts in active bracing. It has been shown by Mac-Thiong et al. that reduced strap tension lowers the brace's pressure against the body and reduces brace effectiveness [82]. This is important as strap tension varies throughout the day as the user moves and settles in the device [83]. Lou et al. created a pneumatic device capable of increasing or decreasing the pressure from a pad internal to the brace in order to achieve proper brace tension [84]. However, this method is limited in how the force between the brace and the human body can be modulated, as the net force does not generally scale with normal pressure. There has been a similar effort towards modulating the force by adding metallic bars to the rigid brace that would act like a spring, Figure 1.4(e) [74, 75] or by adjusting strap tensions, Figure 1.4(f) [76]. However, these, and other types of scoliosis brace introduced in [85], are all passive designs that lack the capability of actively modulating and measuring the pose or the force of the brace. There are some active braces that incorporate motor actuation(s) to provide adjustable stiffness to the

torso, Figure 1.4(g) [77], or to transfer some of the weight of the torso to the hip, Figure 1.4(h) [78]. These designs, however, are incapable of modulating the forces in three dimensions.

1.2.3 Needs for a torso exoskeleton for correction of spinal deformity

The combined stiffness of the muscles, soft tissues, rib cage, and spine determines the elastic behavior of the torso when subjected to external corrective forces provided from the brace. Since the forces applied to the spine, achieved by either force control or by position control, can only be transferred via these intermediate tissues, the outcome of reducing scoliotic curves may be highly dependent upon the stiffness of these surrounding tissues. Therefore, to know what forces or postural correction are required to achieve the desired spine corrections, it is imperative to know the stiffness characteristics of the human torso. For this reason, real time sensing of the pose and forces applied by the brace, and the ability to actively control the corrective forces applied to the human torso are desirable features to increase our understanding of the brace treatment. Moreover, the stiffness of the torso, particularly at regions where curve apices are located, plays a pivotal role in spine correction as it explicitly gives what forces should be applied to the torso to correct the curves. Furthermore, scoliotic curves are three dimensional, which implies that three dimensional correction approaches should be considered [63]. In addition, if the stiffness characteristic of human torso changes over time as a result of changes in the spine throughout treatment, knowing the stiffness of the human torso is necessary to properly plan the right course of treatment.

Based on this reasoning, a torso exoskeleton, Robotic Spine Exoskeleton (ROSE), was developed with the following salient features to address the limitations in current brace designs:

(i) use an underlying principle of the passive brace designs with addition of actuated components that will modulate the brace properties during usage, (ii) improve mobility in the brace by modulating the corrective forces on the spine in desired directions while allowing the users to perform typical ADL, (iii) provide monitoring of the position and force of the brace remotely by built-in sensors, (iv) characterize the stiffness of torso in various pose configurations from force-displacement measurements, and (v) provide effective control of corrective forces in three dimensions on the spine both spatially and temporally. The design and control of ROSE are presented in Chapter 4. Experimental evaluations on some of these features incorporated in the ROSE were conducted with ten healthy individuals and are presented in Chapter 5.

1.3 Overview of chapters

The first goal of this work is to develop a torso exoskeleton that can be used to assist backpack load carriage, particularly by distributing backpack load between the shoulders and the pelvis and compensating for the dynamic loads of a backpack induced by walking, and scientifically study the effects of these strategies on human biomechanics and physiology during loaded walking. The second goal of this work is to develop a torso exoskeleton that can be used in correction of spinal deformity, capable of measuring and controlling either the displacements or the forces on human torso in three dimensions, and to study the stiffness characteristics of the human torso. Overall, the main focus of this work is to develop the science for design of torso exoskeletons, evaluate their effectiveness in backpack load carriage and spinal deformity correction, and develop novel assistive and/or treatment paradigms for these two applications.

These aims are accomplished and organized in the subsequent chapters as follows. Chapter 2 describes the design, modeling, and control methodology used in developing the WEBS. Performance evaluation of the gait-synchronized dynamic load compensation controller is also described in this chapter. Chapter 3 presents experiment with human subjects using the WEBS. Chapter 4 describes the design, modeling, and control methodologies used in developing the ROSE. Two control modes, position and force control, implemented in the ROSE were experimentally evaluated and presented in this chapter. Chapter 5 presents experiment with human subjects using the ROSE. Chapter 3 and Chapter 5 include the details on experiment protocol, data process, results, and discussion of the corresponding experiment. The conclusions drawn from this dissertation are discussed in Chapter 6 with potential future directions.

The following appendices are attached at the end of the dissertation for the reader's reference:

- Appendix A. The Second Spine
- Appendix B. Motorized Second Spine
- Appendix C. Hardware specifications
- Appendix D. Parameterization, kinematics, and trajectory planning of the ROSE
- Appendix E. In vitro spine stiffness measurement and its implication

Chapter 2

Wearable upper Body Suit (WEBS) for backpack load carriage

2.1 Introduction

In this work, three different torso exoskeleton prototypes were developed for assisting backpack load carriage. The first prototype, named the Second Spine, was designed to distribute the backpack load between the shoulders and the pelvis. The load distribution was achieved by three load-bearing columns, connecting the shoulder pads and the waist belt, providing an alternate load pathway to transfer the backpack load from the shoulders to the pelvis, in addition to the human spine. Measurement and adjustment of load distribution were incorporated features of the Second Spine. The design specifications and experimental validation of load distribution capability of the Second Spine is presented in Appendix A.

The second prototype, named the Motorized Second Spine, was designed to actively modulate vertical motions of a backpack to compensate for the dynamic load induced by vertical motions of pelvis during walking, in addition to the load distribution capability. This was achieved by integrating motors, sensors, and real-time controller into the Second Spine. The dynamic load compensation strategy was validated experimentally by controlling the backpack motion nearly stationary with respect to the inertial frame (ground) by which the dynamic force

was minimized. The design specifications, control method, and the experiment apparatus and results of the Motorized Second Spine are detailed in Appendix B.

These two prototypes were used as test-beds to validate the feasibility of incorporating two desired functions, load distribution and dynamic load compensation, into a torso exoskeleton; wearability and portability were not considered in these designs. Therefore, the third prototype, the Wearable upper Body Suit (WEBS), was developed to improve wearability and portability of these prototypes. Improving these features also has allowed us to evaluate the incorporated functions of the WEBS on a group of human subjects.

This chapter presents the design, functions, control strategy, and performance evaluation of WEBS. Section 2.2 describes the design of the WEBS and the two functions of the WEBS, load distribution and dynamic load compensation. Section 2.3 presents the control strategy used in providing assistive force to the human body to reduce dynamic loads of a backpack during walking. Section 2.4 presents the performance evaluation of the WEBS in distributing the load between the shoulders and the pelvis, and reducing the dynamic loads during walking through active control of the assistive force. Section 2.5 summarizes and concludes the chapter.

2.2 Design

The WEBS is conceptualized in Figure 2.1. It consists of a passive module comprised of a shirt, two shoulder pads, two load bearing columns, and a waist belt with the lifting mechanism and an active module comprised of a DC-motor based cable actuator, motor driver, micro-controller, sensor amplifier, and a battery. The suit is designed to be worn between the body and the backpack, Figure 2.2. The backpack load is transferred from the shoulder pads to the load bearing columns and then to the waist belt. The transferred load is modulated either passively or

actively through cables utilized in both modules. A lifting mechanism located between the waist belt and the load-bearing columns is actuated by these cables and achieves two functions: (i) load distribution between the shoulders and the pelvis, and (ii) dynamic load compensation during loaded walking. The system is portable and uses an NI myRio-1900 controller (National Instruments, Austin, TX) programed in Labview (National Instruments, Austin, TX) for real time control of the motors and sensor communications. Details on the hardware specification are provided in Appendix C.1.

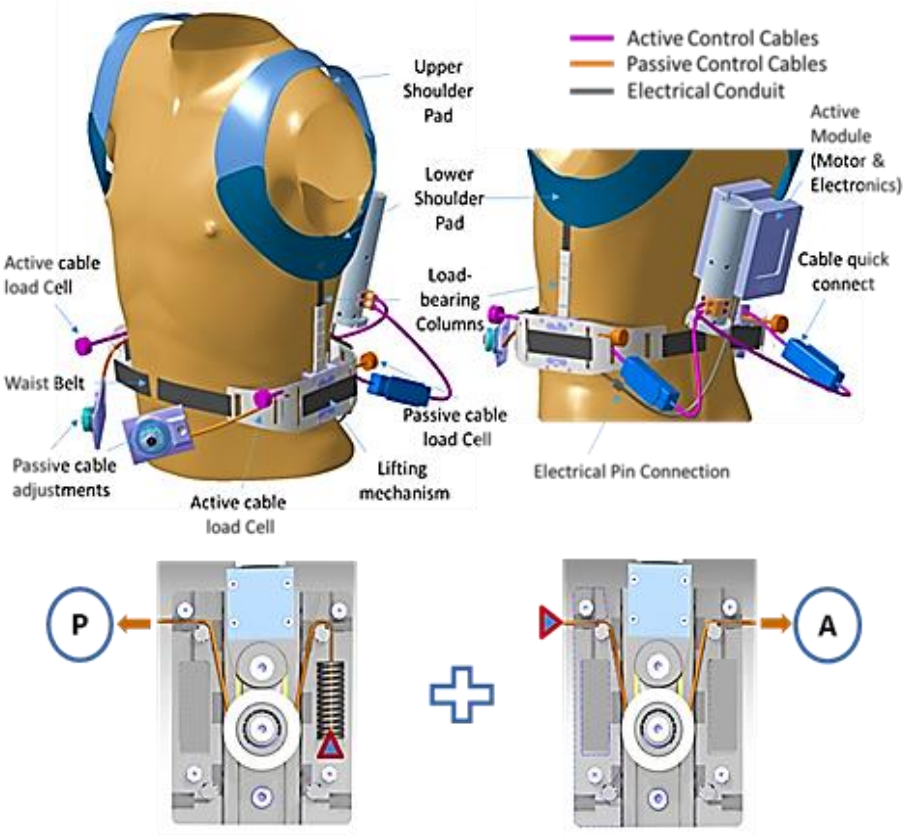

Figure 2.1 Design concept of the WEBS and the lifting mechanism

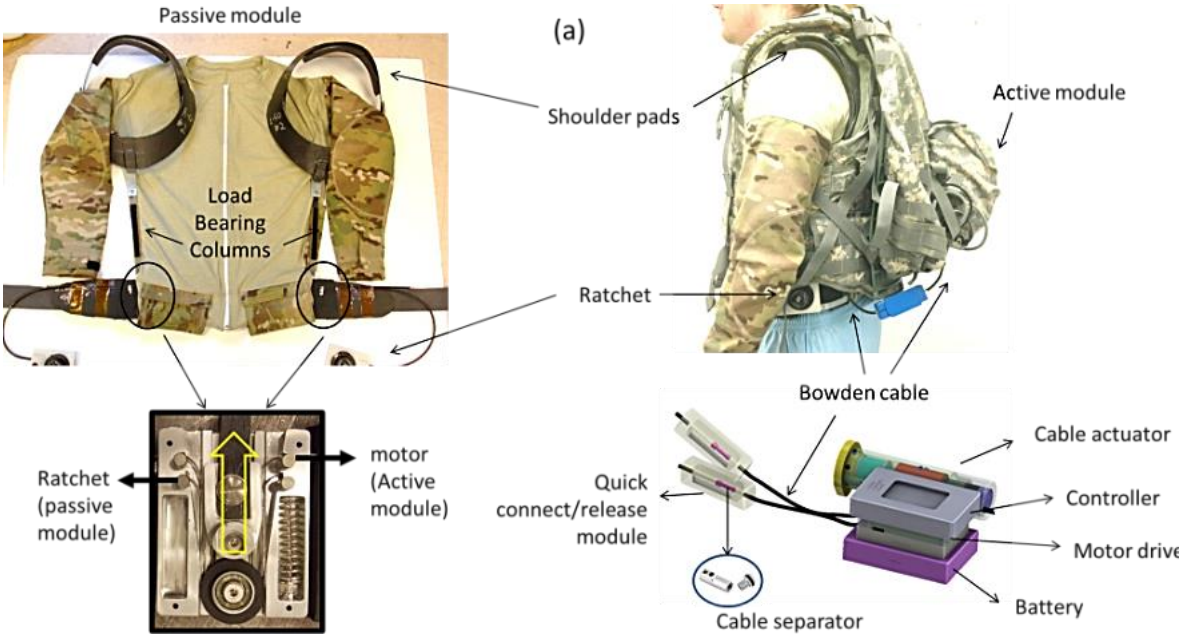

Figure 2.2 The WEBS consisting of two modules: passive (right), and active (left)

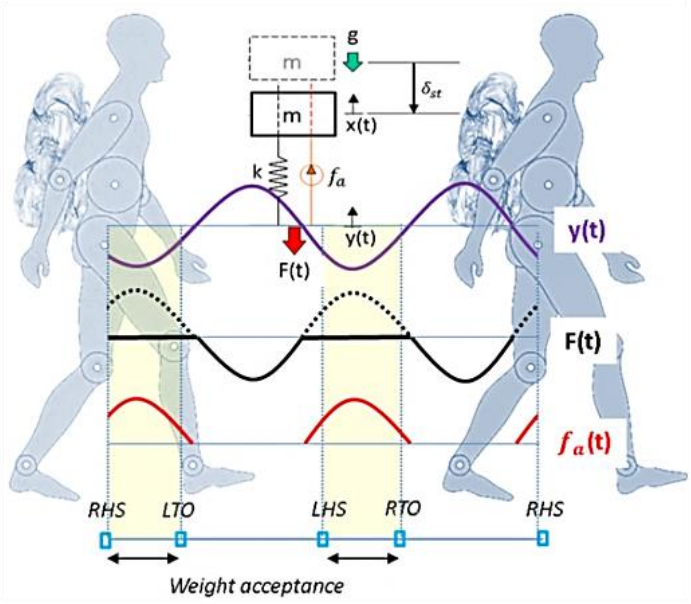

Figure 2.3 Schematic of dynamic load compensation. Backpack with mass m is supported by a spring with stiffness k and a motor provides force f_a. x(t) and y(t) are the vertical displacements of the backpack and the pelvis, respectively. g is the gravitational acceleration and F(t) is the vertical load exerted on the pelvis. The motor supplies assistive force $f_a(t)$ to compensate for the dynamic load of a backpack mostly during the weight acceptance phases of the gait. The solid line in F(t) is the resulting dynamic load in presence of assistive force whereas dotted line represents the case when the assistive force is not provided.

Load distribution (LD): In the passive module, load bearing columns provide an external pathway to transfer the load from the shoulders to the pelvis. The lifting mechanism is placed between a load bearing column and the pelvic belt which provides an interface to modulate the load between the shoulders and the pelvis. A linear slider is an integral part of the lifting mechanism. Its rail is fixed to the belt while its moving carriage is connected to the load bearing column, Figure 2.2. The carriage is driven on the rail by two cables, one from the passive and the other from the active module, working in parallel to elevate the load bearing columns and the shoulder pads. The tension of each cable is measured by a load sensor in line with each cable and attached to it at one end. These sensors are monitored by the micro controller. The cable from the passive module has a spring in series at one end and a ratchet on the other end to tension the cable. As the ratchet is wound, the cable is pulled and lifts the shoulder pads from the shoulders. Then the backpack mass (m in Figure 2.3) is transferred from the shoulder pads to the pelvis via load bearing columns which are supported by cables in series with the springs (k in Figure 2.3). The backpack load, equivalent to $k \times \delta_{st}$ in Figure 2.3, is supported by these springs, which act in parallel to this module, to reduce the power requirement of the motor. The parameter ζ is used to define the user-adjustable load distribution factor ($0 < \zeta < 1$) that describes the percentage of the vertical load transferred from the shoulders to the pelvis achieved through a ratchet mechanism, i.e., $\zeta = 0$ indicates 0% of the vertical load is transferred to the pelvis and 100% is on the shoulders, whereas $\zeta = 1$ indicates 100% of the vertical load is transferred to the pelvis.

Dynamic Load Compensation (DLC): Modulation of the load transferred from the shoulders to the pelvis can also be performed actively, in addition to the load distribution achieved through the passive module, by controlling the tension of the cables in the active

module. This capability allows the device to provide assistive forces to deal with the dynamic components of the transferred load. A gait-synchronized dynamic load compensation strategy was developed to reduce the dynamic loads of a backpack by detecting the body's vertical accelerations, estimating the dynamic load, and controlling the actuator to provide assistive forces. This was achieved with a tri-axis accelerometer (ADXL335, Analog Devices, Norwood, MA) attached to the pelvic belt to obtain feedback on the vertical accelerations of the pelvis, and real time closed-loop control on the cable tension using an in-line tension sensor and a cable actuator through an on-board micro controller. The dynamic load transferred to the pelvis is determined by the partial mass of the backpack (ζm) transferred to the pelvis and the vertical acceleration of the pelvis ($\ddot{y}$). The use of cables as a means to transmit the motor force imposes a unique constraint on the capability of the controlled output force as the cable can only pull not push. Such a property only supplies elevation of the carriage in the lifting mechanism but does not depress it; refer to Figure 2.2. Due to this constraint, only the downward dynamic load can be compensated by the cable force; hence, the following condition logic is implemented.

$$f_d = \begin{cases} \zeta m\ddot{y} + 0.1mg & (\ddot{y} > 0) \\ 0.1mg & (\ddot{y} \leq 0) \end{cases} \tag{2.1}$$

This logic determines the desired cable force (f_d) based on the direction of the vertical motion of the pelvis such that the motor outputs the force during double support periods, mostly during the weight acceptance phases of gait, Figure 2.3. When the measured acceleration is less than or equal to zero, the logic outputs the minimum cable tension to prevent cable slack which was set to be 10% of the backpack load.

2.3 Gait-synchronized force control for dynamic load compensation

The actuator's goal is to apply the assistive forces at the pelvis to compensate for the dynamic loads induced by the vertical motions of the pelvis. A gait-synchronized force controller is designed that uses the motion of the pelvis as an input to detect the gait. With the distributed load and the measured vertical motion of the pelvis, the controller estimates the dynamic load and outputs the actuator forces to cancel that load. This strategy is achieved in two steps: (i) desired assistive force computation and (ii) desired assistive force implementation.

2.3.1 Desired assistive force computation

The force controller was designed to control the actuator force based on the measured acceleration of the pelvis. The model-based controller, a part of the controller that estimates the dynamic load from the measured vertical acceleration of the pelvis ($\ddot{y}$) and the load distributed to the pelvis (ζm), was implemented at 200 *Hz* and is referred to as the high level controller, Figure 2.4. The motor outputs the cable force (f_a) to the platform based on the desired cable force (f_d), and together with the measured spring force (f_s) the total load exerted on the pelvis (F) is the sum of f_s and f_a.

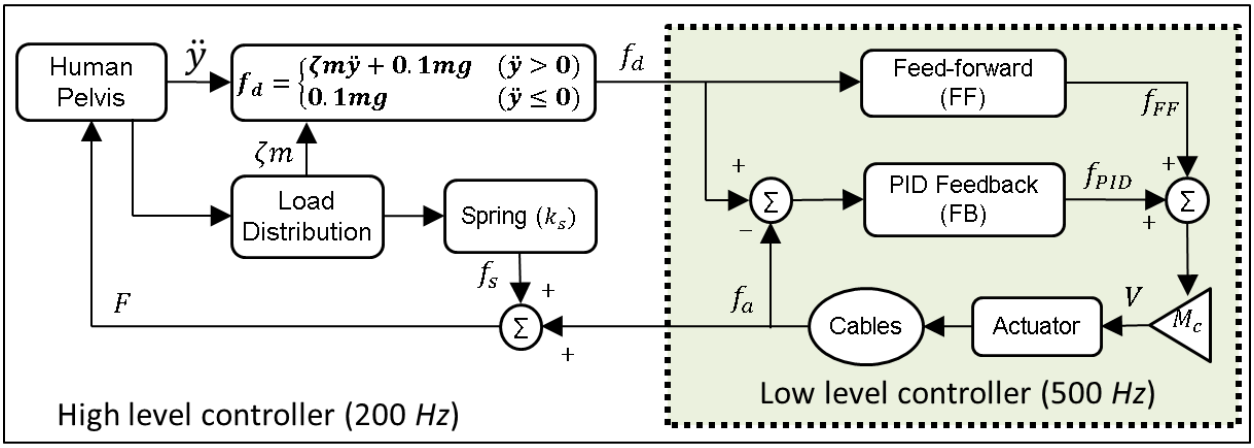

Figure 2.4 The force controller implemented for gait-synchronized dynamic load compensation

2.3.2 Desired assistive force implementation

The closed-loop tension controller was implemented at 500 *Hz* and is referred to as the low level controller, Figure 2.4. A Proportional-Integral-Derivative (PID) controller was used to track the error between the desired cable force (f_d) to the actual cable force (f_a) and outputs the f_{PID} command. An open loop reference feed-forward term f_{FF} with a unit gain is implemented to avoid a high proportional gain in the PID controller. M_c is the motor constant (*V/N*) that relates the commanded voltage (*V*) to the cable force (*N*). The net commanded voltage to the motor, V, is given by the following expression.

$$V = M_c(f_{FF} + f_{PID}) \tag{2.2}$$

$$\text{where} \quad f_{PID} = \left[K_p e + K_i \int e(t)dt + K_d \left(\frac{de(t)}{dt}\right)\right] \tag{2.3}$$

$$\text{and} \quad e = f_d - f \; and \; f_{FF} = f_d \tag{2.4}$$

where M_c is the motor constant (V/N) that relates the commanded voltage (V) to the cable force (N) obtained experimentally and $K_p, K_i,$ and K_d are the gains for the proportional, integral, and derivative terms of PID controller, respectively, which were also experimentally tuned.

2.4 Controller evaluation

Experimental evaluation on the controller was conducted while a person walked on a treadmill in several different configurations of the device. Reflective markers were placed on both the waist belt and the shoulder pads of the WEBS to capture their kinematics through a motion capture system (Bonita, Vicon Motion Systems, Oxford, UK) while an integrated accelerometer on the waist belt simultaneously measured the vertical accelerations of the pelvis. Force transferred from the shoulders to the pelvis was measured through the tension in the cables using load cells.

The first experiment was designed to evaluate the sensor accuracy of the accelerometer and the computational accuracy in calculating the vertical motion of the pelvis using the accelerometer. Those data were compared with the kinematic data obtained from a motion capture system. Five different walking speeds - 60%, 80%, 100%, 120%, and 140%, of self-selected walking pace (SSP) - were tested, for 2 minutes each, to simulate slow and fast walking conditions so that a range of frequencies (0.7–1.15 Hz) and magnitudes (23–48 mm) of vertical motion of the pelvis could be tested, Figure 2.5(left). Figure 2.5(right-top) plots the vertical motion of the pelvis computed using the accelerometer compared with that measured from the motion capture system. The motion computed using the accelerometer showed reasonable accuracy. Except for the slowest and the highest walking speed, the maximum RMS error was

less than 4 mm (10%), which validates the reliability of accelerometer data and real-time computational algorithm used in the controller, Figure 2.5(right-bottom).

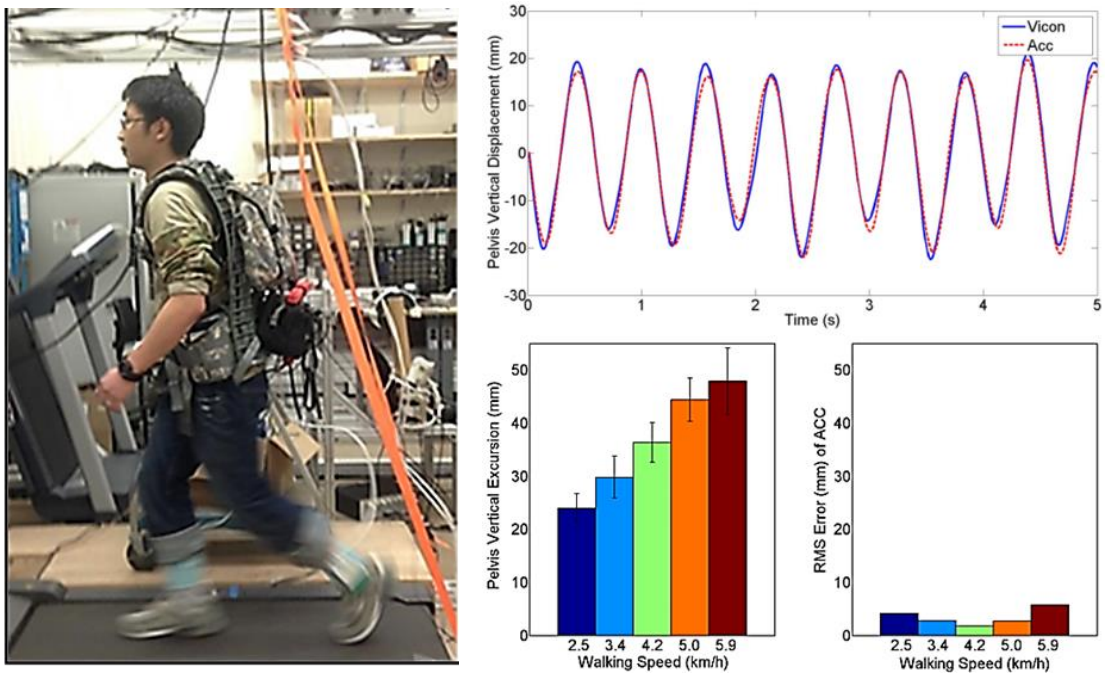

Figure 2.5 Evaluation of the accelerometer sensor accuracy: (left) picture of a subject in experiment, (right-top) comparison on vertical displacements of the pelvis measured from Vicon motion capture system (solid line) with that computed from the on-board accelerometer (dashed line); (right-bottom) pelvis vertical excursion of five different walking speeds and maximum RMSE of those computed using the accelerometer data

The second experiment was designed to evaluate the performance of two functions of the device: load distribution and dynamic load compensation. A subject wore the WEBS and a backpack and walked on a treadmill at SSP for 2 minutes. The backpack load was 25% of the subject's body weight (BW), which falls within the range of typical load tested in other human load carriage studies. Two conditions were compared: session 1 (S1) applied 50% load distribution between the shoulders and the waist and session 2 (S2) applied dynamic load compensation in addition to load distribution.

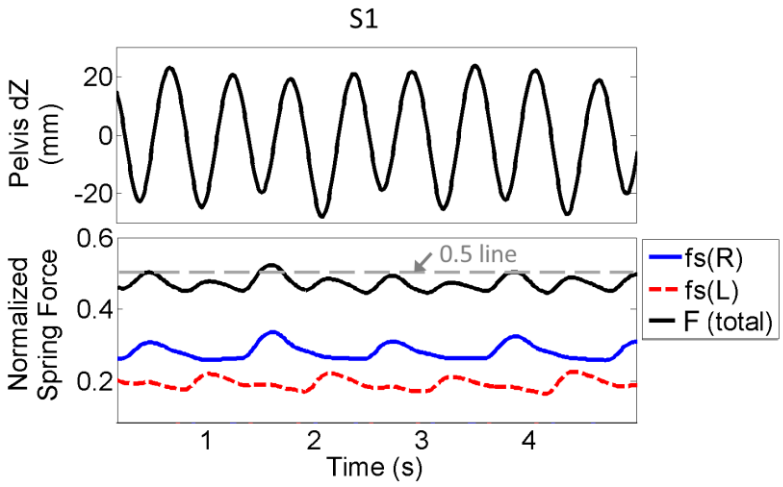

Figure 2.6 Experimental data from S1 during which only the passive module was engaged to transfer 50% of the backpack load from the shoulders to the pelvis: (top) pelvis vertical motion (mm) and (bottom) force transferred from the shoulders to the pelvis measured from the cable; fs(R) and fs(L) are the transferred force from the right and the left side of the device, respectively, and F(total) is the sum of those forces. These forces are normalized to the backpack load

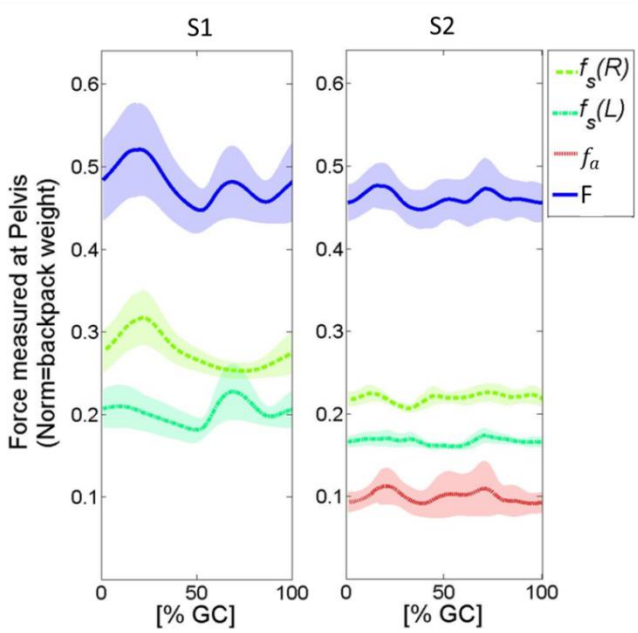

Figure 2.7 Force transmission from the shoulders to the pelvis in S1 (left) compared with S2 (right) averaged over a gait cycle; f_s(R) and f_s(L) denote the transferred force measured from the right and the left side of the passive module; f_a denotes the assistive force provided from the active module; F denotes the total force (sum of the forces from passive and active modules); the assistive forces reduced the peaks of the total transferred force (F) in S2 compare to S1

Figure 2.6 shows the vertical displacement of the pelvis and the cable forces measured from the passive module in S1. Forces are normalized to the backpack weight. The total force (F) was close to 0.5, which indicates that about 50% of load has been transferred from the shoulders to the pelvis. The curves in the force data indicates the dynamic loads induced during walking. The phase difference in peak forces between the right and the left side of the WEBS was observed, which indicates that alternate loading between the right and left side of the shoulders corresponding to the side of heel strike.

Figure 2.7 plots the comparison of forces transmitted from the shoulders to the waist between S1 and S2, both averaged over a gait cycle. f_s(R) and f_s(L) denote the force transferred from the right and left side of the passive module, respectively. Though the passive module was adjusted to evenly distribute the load between the shoulders, symmetry in load transmission between the shoulders was not retained, as can be seen from the differences in the mean values of f_s(R) and f_s(L). This may have been probably due to the backpack settled on the body non-symmetrically between the shoulders during the initial walking cycles. The assistive force f_a reduced the peak dynamic force transferred from the shoulders to the pelvis in the passive cables. Consequently, the peaks of the total transferred force (F) during walking reduced. This result validates the active module in providing assistive forces in response to gait to reduce the dynamic load of the backpack during walking.

2.5 Conclusion

In this chapter, the design, control strategy, and evaluation of the WEBS were presented. The conceptual design, the cable-driven load distribution mechanism, and the two functions of the WEBS were first presented in Section 2.2. The two salient functions of WEBS are load distribution and dynamic load compensation of a backpack. These functions were realized by the design of two modules – passive and active – that are integrated within a custom fitted shirt with motion/force sensors, an actuator, and a real time controller. In Section 2.3, the control strategy to provide gait-synchronized assistive forces to reduce the dynamic load of a backpack during waking was presented. The two functions of the WEBS were experimentally evaluated on a single subject while the subject walked on a treadmill carrying 25% BW backpack, which was described in section 2.4. The results of the evaluation were also presented in this section, showing the WEBS distributed the load between the shoulders and the pelvis, and reduced dynamic loads induced during loaded walking. The next chapter will present the experimental evaluation of these outcomes of the WEBS on a group of healthy subjects, in terms of their effects on kinematics, muscle use, ground reaction force, and metabolic consumption.

Chapter 3

Human load carriage study using WEBS

3.1 Introduction

In the previous chapter, the design, control, and performance evaluation of the WEBS were presented. In this chapter, we present the human subject study to evaluate two strategies to assist backpack load carriage, which are distributing the backpack load between the shoulders and the pelvis, and reducing dynamic load during loaded walking. The experiment is designed as a crossover study involving 12 healthy subjects. The study tested the hypothesis that distributing the load of a backpack between the shoulders and the pelvis during load carriage reduces body adaptations and metabolic cost of loaded walking. We also hypothesized that the dynamic load compensation would further reduce the body adaptations, muscle activity, and ground reaction force; thereby reduce the metabolic cost over both unaided load carriage and carriage with part of the load distributed to the pelvis. The chapter is organized as follows. Section 3.2 describes the experiment protocol and the metrics used in the experiment. Section 3.3 describes the data processing and statistical analysis methods. Section 3.4 presents experiment results. Section 3.5 discusses the results and its implications. Section 3.6 summarizes and concludes the chapter.

3.2 Protocol

Twelve healthy, male adults participated in the experiment (age 29±6 years, stature 1.76±0.08 m, leg length 0.89±0.046 m, and weight 77.2±12.5 kg). The experimental protocol (shown in Figure 3.1(a)) was approved by the Columbia University Institutional Review Board and informed consent was obtained from all participants before the experiment. All subjects were right foot dominant and free of any physical disorders or impairments that might impede their ability to walk. Subjects completed the full protocol during a single session. The subjects carried 25% of their BW, including the weight of the active module, in the loaded sessions. This load was chosen to fall within the weight range normally tested in load carriage studies.

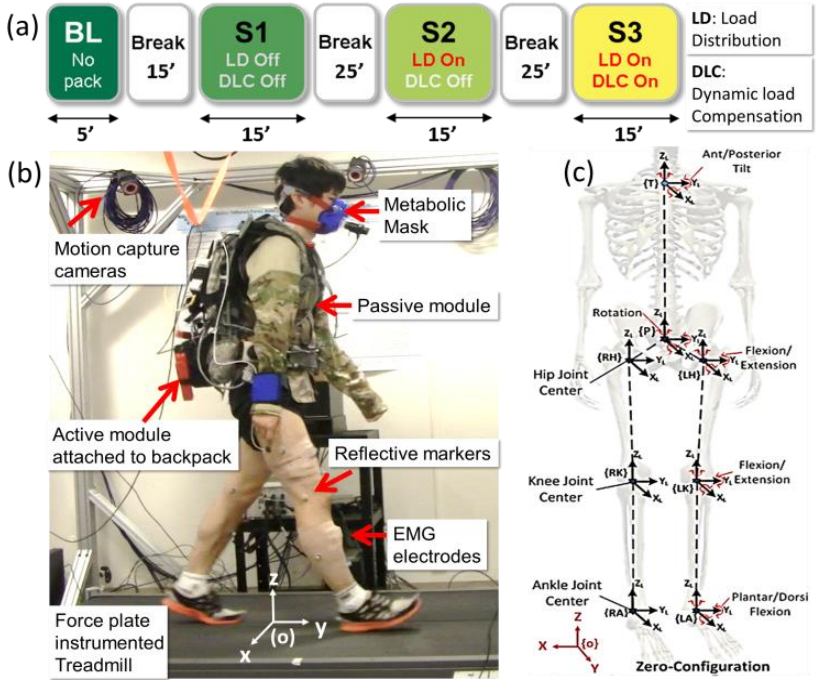

Figure 3.1(a) Experiment protocol used in the study, (b) experiment setup, and (c) body coordinate frames based on the marker locations in zero-configuration (upright standing posture), and the global coordinate frame origin at {O}.

The study consisted of four sessions; (i) *Baseline (BL):* In this session, subject walked on a treadmill for 5 minutes while wearing the device, without carrying any load. (ii) *Session 1 (S1):* In this 15-minute loaded walking session, the subject wore the device and the backpack. Prior to this session, the load bearing columns were detached from the shoulder pads ensuring zero transfer of the backpack load from the shoulders to the pelvis through the device. (iii) *Session 2 (S2):* This was another 15-minute loaded walking session with the same conditions as in S1 except the load distribution between the shoulders and the pelvis was achieved by adjusting the ratchet of passive module until it reached 50% of total load (i.e., load equally distributed between the shoulders and the pelvis). (iv) *Session 3 (S3):* This was the last 15-minute loaded walking session during which the active module was turned on to provide assistive forces to achieve dynamic load compensation, in addition to the same load distribution used in S2. All subjects completed BL first, then S1 to S3 in a randomly assigned order. A 15-min break was given after the BL before start of the first loaded walking session, and 25-min breaks were given in between the subsequent loaded sessions. The self-selected walking speed was used which was determined before the beginning of the experiment and was consistent across all sessions.

The metrics and measurement devices used in the experiment were: kinematics (joint range of motion, trunk inclination angle, pelvis vertical excursion, backpack vertical excursion) using a motion capture system; ground reaction forces (peak, impulse, loading rate of vertical and anteroposterior ground reaction force) using a force-plate treadmill; muscle functions (average muscle activation, change in median frequency of muscle activation over time) using an electromyography sensors; metabolic cost (average oxygen consumption rate normalized to body weight, heart rate) using a metabolic measuring mask; spatiotemporal parameters of gait using the kinematic and ground reaction force data.

Reflective markers were placed on the subject, the device, and the backpack to record their kinematics. A motion capture camera system was used to track these markers (Vicon Motion Systems®, Oxford, UK), sampled at 200 *Hz*. The lower limb marker locations were adapted from [86]. Three markers were placed on the trunk, one on the manubriosternal junction and one on the left and one on the right side of sternoclavicular joint, to get the trunk motions. Backpack motion was captured with the markers placed on top of the rigid frame of the backpack. Surface electromyography (EMG) was used to measure the activity of 9 muscles, sampled at 1 *kHz*: Rectus Femoris (RF), Vastus Lateralis (VL), Biceps Femoris (BF), Gastrocnemius Medialis (GM), Soleus (SOL), Tibialis Anterior (TA), Rectus Abdominis (RA), Upper Trapezius (TRAP), and Erector Spinae (ES). Lower limb EMG was recorded from the dominant leg of each subject (all were right leg dominant). Single-differential signals were high-pass filtered with a 1st order analog filter ($f_c = 10Hz$), digitized and sent to a wireless desktop unit (Noraxon®, Scottsdale, Arizona) which was connected to the Vicon digital acquisition board and synchronized with the motion capture data. A split-belt treadmill with force plates (Bertec®, Columbus, OH) was used to measure the ground reaction forces (GRF) of each leg during the experiment, sampled at 1 *kHz*. Signals were sent to the Vicon digital acquisition board and synchronized with the motion capture data. A mobile cardiopulmonary testing system (Oxycon Mobile®, Carefusion, Yorba Linda, CA) was used to measure the breath-by-breath oxygen consumption rate ($\dot{V}O_2$) and heart rate (HR). Before starting the experiment, subjects sat while relaxed and their resting $\dot{V}O_2$ and HR were measured. All measurements, other than cardiopulmonary measures, were collected twice for one minute each at the 2nd and 4th minute in BL session, three times for one minute each at 4th, 9th, and 14th minute in other sessions. Cardiopulmonary data were recorded during the

entire session but only the steady metabolic data were considered in the analysis. The experimental setup can be seen in Figure 3.1(b).

3.3 Data Processing

Each subject's recorded data (other than cardiopulmonary measurements) from the final minute of data collection was treated as the reference for the corresponding session and used in the analysis, labeled respectively as BL, S1, S2, and S3. Then each parameter was normalized in time to 100% of the gait cycle (GC) based on gait events. Heel strike (HS) and toe off (TO) were detected for each leg from the force plate where a gait cycle was defined from a right heel strike (RHS) to the subsequent right heel strike.

Sagittal plane gait kinematics, pelvis and backpack vertical motions, and torso flexion were analyzed using Vicon Nexus software (Vicon Motion Systems®, Oxford, UK) and Matlab (The MathWorks Inc., Natick, MA). Specifically, stance-phase peak flexion and extension for the lower limb joints (dorsi- and plantar- flexion for the ankle), and torso peak flexion over gait cycle were computed for analysis. Global and local coordinate systems used in kinematic analysis were those illustrated in Figure 3.1(c). Pelvis and backpack vertical motions were measured with respect to the ground coordinate frame based respectively on the pelvic center calculated from the centroid of a triangle formed by three pelvic anatomical markers, i.e., sacrum, right- and left- anterior superior iliac spine (ASIS), and backpack frame center defined as the centroid of a triangle formed by three markers placed on the backpack frame. Those motions were averaged over each gait cycle for their mean value and the mean range, and then normalized to subject's leg length (the distance measured from the greater trochanter marker to

the ground). Based on gait events and self-selected walking speed, spatiotemporal variables were analyzed, which are double stance duration (DS), single stance duration (SS), stance to swing ratio, stride length (mm), and cadence (steps/min). Toe clearance (mm) was also analyzed from the toe marker kinematics data. Spatial parameters with the dimension length (stride length and toe clearance) were normalized to subject's leg length to eliminate differences among participants' data attributable to differences in body height.

Upper body raw EMG signals were processed for ECG noise reduction through adaptive filtering (Noraxon MR3 software). An auxiliary EMG channel was recorded over the left Pectoralis Major and used as a reference for ECG noise reduction. Then, all signals were post-processed using custom MATLAB code: band-pass filtering (4^{th} order Butterworth, 20-500 *Hz*), full-wave rectification, and smoothing using a low pass filter (4^{th} order Butterworth, f_c = 6 *Hz*), then split and time-normalized over the gait cycle to obtain the linear envelope. Then, the integral over the linear envelope was computed and averaged over each session to estimate the level of muscle activity (iEMG). Prior to statistical analysis, iEMG values of each subject were normalized to the corresponding peak values recorded during the baseline session. Power spectral frequency of the muscle EMG signals was analyzed using Fast Fourier Transform (FFT) method to obtain the median power frequency (MPF), i.e., the frequency above and below which the integrated power is equal, to quantify muscle fatigue. The decrease in MPF of the surface EMG profile is a recognized method for determining fatigue of a muscle [87, 88] thus relative changes in the MPF between the sessions were used to detect the fatigue level of the muscle.

The vertical ground reaction force (GRF_Z) and anteroposterior ground reaction force (GRF_Y) data were recorded at 1 *kHz*, normalized to subject weight, low-pass filtered (4^{th} order Butterworth, $f_c = 20$ *Hz*), and time normalized to the gait cycle. In each gait cycle, GRF_Y was

broken into two phases: braking (calculated from the GRF_Y during the early stance phase) and propulsive (calculated from the GRF_Y during the late stance phase). The peak ($F_{V_{peak}}$, $F_{B_{peak}}$, and $F_{P_{peak}}$); impulse (I_V = time integral of the GRF_Z, I_P = time integral of the positive GRF_Y, and I_B = time integral of the negative GRF_Y); and loading rate ($\dot{F_V}$=$F_{V_{peak}}$/{time from HS till $F_{V_{peak}}$}, $\dot{F_B}$ = $F_{B_{peak}}$/{time from HS to $F_{B_{peak}}$}, and $\dot{F_P}$ = $F_{P_{peak}}$/{time from start of positive GRF_Y till TO}) were calculated for each session.

Cardiopulmonary measures ($\dot{V}O_2$ and HR) were low pass filtered (4^{th} order Butterworth, f_c=0.04 Hz) over the duration of each session, discarding the first three minutes of each session to remove large transients, then averaged for each session subject-wise. Then, average values were normalized to their resting value. The average oxygen consumption rate was normalized for subject mass ($\dot{V}O_2$/kg) prior to statistical analysis.

Statistical analysis was conducted on each metric using SPSS v22.0 (IBM Corp, NY, USA). Mauchly's test of sphericity was performed on each dependent variable to check if the sphericity assumption was valid, and either Huynh-Feldt correction (if $\varepsilon > .75$) or Greenhouse-Geisser correction (if $\varepsilon < .75$) was applied if the sphericity assumption was violated. One-way repeated measure ANOVA ($\alpha = 0.05$) was used to test the different conditions on each dependent variable. When a significant effect was detected, pairwise comparisons (Wilcoxon signed rank tests) with Bonferroni-Holm correction were used to determine significance between the conditions ($\alpha = 0.05$). The chosen pairs for the statistical difference comparison were unloaded vs. loaded sessions (BL-S1, BL-S2, BL-S3), and pairs within the loaded sessions, BL-S1 (refer as the effects of backpack), S1-S2 (refer as the effects of load distribution), S2-S3 (refer as the effects of dynamic load compensation), and S1-S3 (refer as the effects of load distribution

with dynamic load compensation). The bar plots in the following section represent the mean ± standard errors. The group mean value and the p value between sessions are presented in the tables for each variable; hence they are not repeated in the text for brevity.

3.4 Results

From this section to the next section, LD and DLC will be used as an abbreviation for load distribution and dynamic load compensation, respectively.

3.4.1 Kinematics

The average sagittal plane hip, knee, and ankle joint angles for a representative subject are shown in Figure 3.2. The group average of the stance-phase peak flexion/extension (or dorsi- and plantar- flexion) angles are also presented. When carrying a backpack load (S1), stance phase hip flexion/extension and knee flexion were significantly different from the other three sessions, and ankle plantar flexion showed a significant increase compared to unloaded walking (BL) and significant decrease with DLC (S3). Interestingly, the ankle plantar-flexion angle was significantly different between DLC (S3) and the other two loaded conditions (S1 and S2). Ankle dorsi-flexion angles were not significantly different between any sessions, Table 3.1.

The vertical excursion of the backpack and pelvis, and sagittal plane torso flexion angle are presented for a representative subject. The mean and range of the vertical motion of the backpack and pelvis, and mean sagittal plane torso flexion angle for the group are also shown. The vertical motion of the backpack over the gait cycle shows the cyclic motion where the troughs occur during the double stance phases of gait, particularly during the early stance, and

the peaks occur in the single stance phases of gait, particularly around mid-stance. The upward shifts in the mean vertical position of the backpack were significantly different between all loaded sessions. This was an expected result, as the load distribution is achieved by lifting the shoulder pads off the shoulders which, in turn, lifts up the backpack vertically. In addition, the dynamic load compensation added from S2 to S3 further pushes up the backpack during the weight acceptance phases of gait, which would explain the additional vertical shift in the mean position of the backpack. Also, the mean range of vertical motion of the backpack decreased from S1 to S2, S2 to S3, and S1 to S3. The mean vertical position of the pelvis was significantly decreased from BL in all loaded sessions. Between the loaded sessions, there was a smaller decrease in mean vertical position of the backpack with DLC (S3) compared to backpack only (S1).

The vertical range of motion of pelvis was also affected by the load, showing a significant increase from unloaded walking (BL) compared to the loaded sessions. This increase in the vertical range of motion of the pelvis significantly reduced with LD (between S1-S2), and DLC (between S1-S3); and DLC showed a difference from LD alone (between S2-S3). The sagittal plane torso flexion motion did not show clear trunk coordination timed with the gait events in the different sessions. The mean torso flexion was significantly higher in S1 and S2, but not in S3 compared to unloaded walking session (BL). With DLC (S3), mean torso flexion angle was significantly reduced from the other two loaded conditions (S1 and S2).

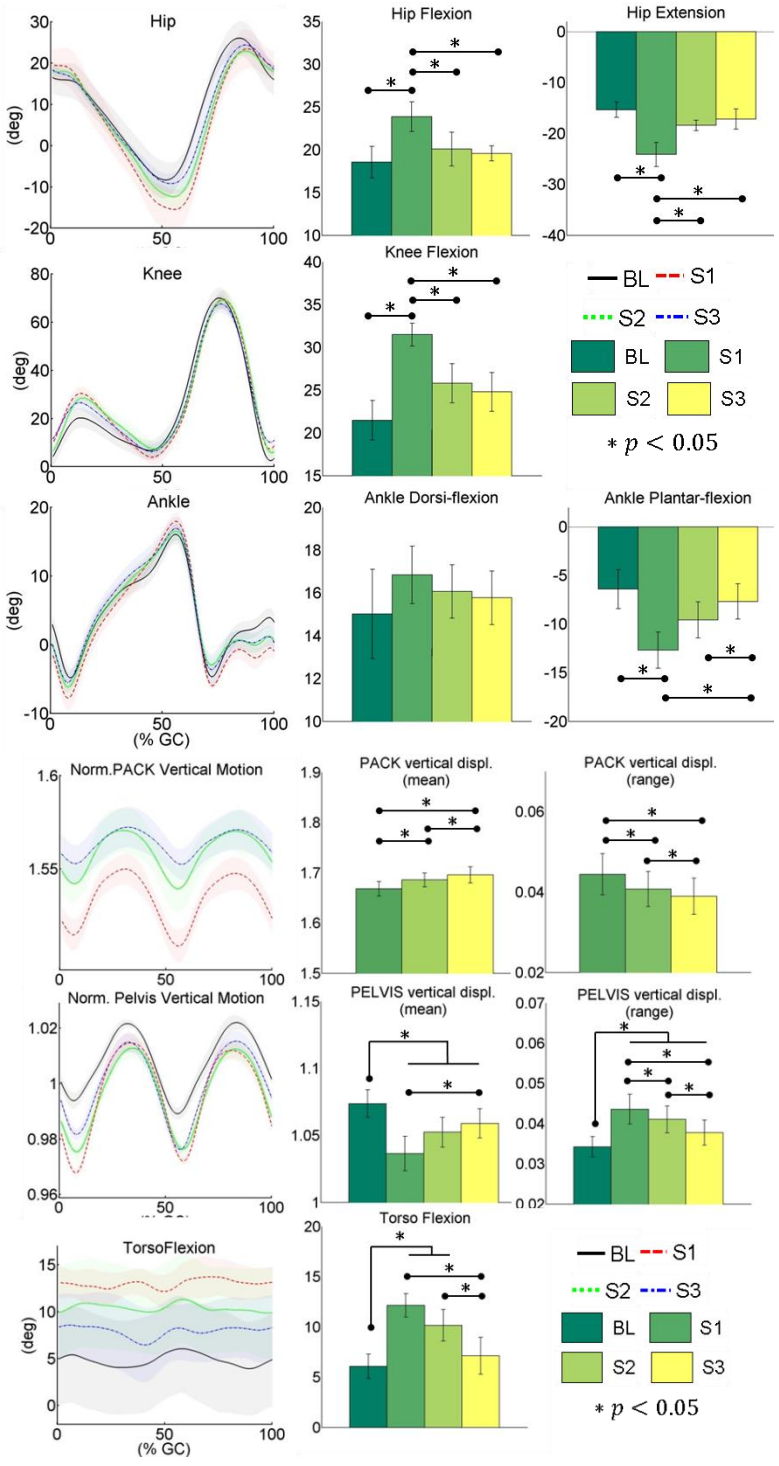

Figure 3.2 (from top row) Hip, knee, and ankle sagittal plane joint angles during different trials for a representative subject (left), and the stance-phase peak joint flexion/extension angles (dorsi-/plantar-flexion for ankle) for the group (right); The average backpack and pelvis vertical excursion, and sagittal plane torso flexion over the gait cycle for different trials for a representative subject (left), and the group average of mean and range of vertical motion of the backpack and pelvis, and the mean torso flexion (right). The asterisk indicate statistically significant effect between the corresponding sessions ($p<0.05$)

3.4.2 Spatiotemporal parameters

The average temporal parameters of gait are shown in Figure 3.3. Carrying a backpack load without DLC (S1 and S2) significantly increased the double support period (DS) over that of unloaded walking (BL). With DLC (S3), DS was significantly reduced from load only (S1). The increase in DS decreased the single support period (SS) for all loaded cases as compared to BL. SS also showed significant difference between all loaded sessions. Stance/swing ratio increased with the backpack load (S1) as compared to BL and the other two loaded cases (S2 and S3). It is worth noting that all of these changes due to the backpack load were significantly attenuated (i.e., less deviation from their baseline values) when subjects carried the same backpack load but with DLC (between S1-S3). Stride length and toe clearance showed a decreasing tendency in S1 compared with BL while cadence had an increasing tendency in S1 compared with BL. These changes due to the backpack load were reduced in S2 and further reduced in S3, with respect to S1, however, these changes were not statistically significant, Table 3.1.

Table 3.1. Comparison on the kinematics and spatiotemporal variables between sessions (n=12)

* $p < 0.05$	BL	S1	S2	S3	p value		
					S1-S2	S1-S3	S2-S3
Hip Flex.[a]	18.6	23.9	20.1	19.6	*	*	0.89
Hip Ext.[a]	-15.3	-24.1	-18.4	-17.2	*	*	0.46
Knee Flex.[a]	21.5	31.5	25.8	24.8	*	*	0.40
Ankle DorsiF.[a]	15.0	16.9	16.1	15.8	1.00	1.45	1.56
Ankle PlantarF.[a]	-6.4	-12.7	-9.6	-7.7	0.09	*	*
Pack V.mean[b]	n/a	1.668	1.686	1.696	*	*	*
Pack V.range[b]	n/a	0.044	0.041	0.039	*	*	*
Pelvis V.mean[b]	1.074	1.036	1.052	1.059	0.05	*	0.08
Pelvis V.range[b]	0.034	0.044	0.041	0.038	*	*	*
Torso Flex.[a]	6.1	12.1	10.2	7.1	0.13	*	*
DS[c]	15.0	16.9	16.5	15.9	0.09	*	0.08
SS[c]	34.9	32.0	33.3	33.7	*	*	*
Stance/Swing[d]	1.834	1.998	1.916	1.886	*	*	0.06

Stride Length [b]	1.197	1.138	1.147	1.181	0.19	0.06	0.21
Cadence [e]	97.6	101.0	99.5	98.2	0.56	0.10	0.52
Toe Clearance [b]	0.130	0.123	0.125	0.128	0.19	0.11	0.11

Units: a) degree(°); b) normalized to subject's leg length (unitless); c) percentage of gait cycle [%GC]; d) stance period/ swing period (ratio); e) steps/min

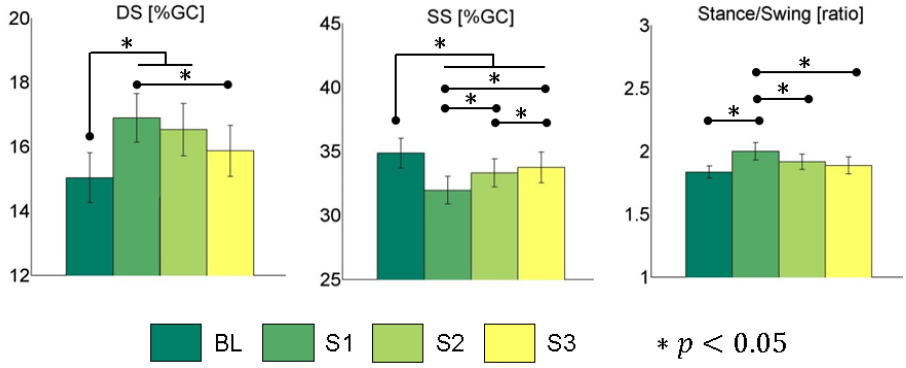

Figure 3.3 Group average temporal parameters: double support (DS), single support (SS), and stance/swing ratio

3.4.3 Ground reaction forces

Vertical ground reaction forces

The weight normalized vertical ground reaction force (GRF_Z) for a representative subject, and a group average of its peak, time integral, and loading rate are shown in Figure 3.4. These parameters were all significantly higher in the loaded sessions compared to BL. These expected results reflect peak vertical forces during the weight acceptance phases due to the added mass on the body. Interestingly, significant differences in these values were observed between different loaded walking trials, i.e., between S1-S2, between S1-S3, and between S2-S3, except for the vertical impulse (I_V) value between S2-S3 which did not show significance, Table 3.2. These results indicate reduced vertical ground reaction force components, in terms of its peak, impulse, and loading rate was achieved with LD, and these were further reduced when DLC was provided.

Anterior-posterior ground reaction forces

The weight normalized anterior-posterior ground reaction force, GRF_Y, were analyzed for two periods (braking and propulsive) as explained in Section 3.3. Peak braking ground reaction force ($F_{B_{peak}}$) and braking loading rate ($\dot{F_B}$) were significantly higher in all loaded sessions (S1, S2, S3) compared to BL. Interestingly, such changes in peak and loading rate of braking ground reaction forces were significantly reduced in S3 compared to both S1 and S2. The loading rate was also reduced from S2 to S3. Braking impulse (I_B) showed a similar trend to $F_{B_{peak}}$ and $\dot{F_B}$ but was not statistically significant. On the other hand, peak propulsive ground reaction force ($F_{P_{peak}}$) and propulsive impulse (I_P) were significantly higher in all loaded sessions compared to BL. However, these values, including propulsive loading rate $(\dot{F_P})$, did not show a significant difference between loaded sessions, as shown in Table 3.2.

Table 3.2 Comparison on the ground reaction force variables between sessions (n=12)

$* p < 0.05$	BL	S1	S2	S3	p value		
					S1-S2	S1-S3	S2-S3
$F_{V_{peak}}$ [a]	1.07	1.31	1.28	1.27	*	*	*
I_V [a]	48.82	62.01	61.06	60.57	*	*	0.114
$\dot{F_V}$ [b]	5.41	7.08	6.59	6.31	*	*	*
$F_{B_{peak}}$ [a]	-0.14	-0.20	-0.19	-0.18	0.059	*	*
I_B [a]	-2.67	-3.16	-2.83	-2.71	0.059	0.059	0.199
$\dot{F_B}$ [b]	-1.08	-1.63	-1.48	-1.39	*	*	*
$F_{P_{peak}}$ [a]	0.11	0.17	0.17	0.16	0.33	0.21	0.33
I_P [a]	1.72	2.90	2.87	2.85	2.02	0.89	0.89
$\dot{F_P}$ [b]	0.65	0.82	0.75	0.77	0.16	0.68	0.22

Units: a) group average of weight normalized values; and b) group average of weight normalized value/time (s)

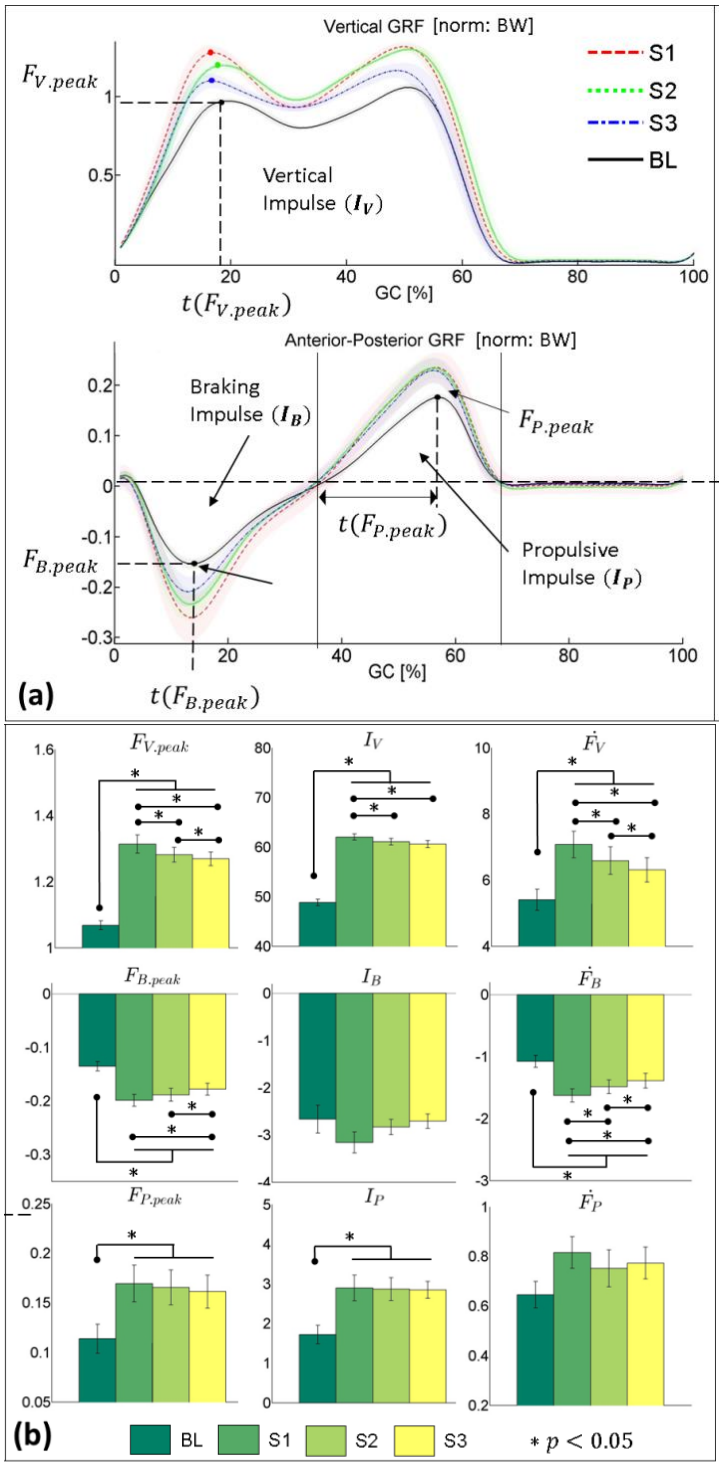

Figure 3.4 (a) Weight normalized vertical (GRF_Z) and anterior-posterior (GRF_Y) ground reaction force during different trials for a representative subject; (b) peak GRF_Z ($F_{V_{peak}}$), time integral of GRF_Z (I_V, vertical impulse), and vertical loading rate ($\dot{F}_V$) ; peak braking GRF_Y ($F_{B_{peak}}$), time integral of negative GRF_Y (I_B, braking impulse), and braking loading rate ($\dot{F}_B$); peak propulsive GRF_Y ($F_{P_{peak}}$), time integral

of positive GRF_Y (I_P, propulsive impulse), and propulsive loading rate ($\dot{F}_P$) values during a gait cycle are presented for the group.

3.4.4 Muscle activity and fatigue

The average iEMG and median power frequency (MPF) values of 6 recorded muscles across the walking conditions are plotted in Figure 3.5. Activity of the rectus femoris (RF), which is responsible for eccentric control of the knee flexion during weight acceptance, was higher when subjects walked with a backpack load without DLC (S1 and S2), reflecting an increased effort to control knee flexion during weight acceptance, but no significant difference was found between BL and S3. The activity of RF and VL was reduced using DLC (S3) compare to S1. MPF of RF reduced from BL in all loaded sessions. Differences in MPF were observed for RF and VL between S1 and S3. Gastrocnemius medialis (GM), which provides foot plantar flexion and knee flexion during push-off, showed higher activity when subjects walked with load, reflecting increased efforts to provide a power-burst at push-off. Such an increase was reduced from S1 for the other two loaded sessions. S1 showed an increase in muscle activation of the soleus (SOL) compared to all other sessions. Changes in MPF of GM and SOL were not significant between sessions, Table 3.3.

The activity of tibialis anterior (TA) was not significantly different when carrying the load. Nonetheless, MPF of TA significantly decreased in S1 from BL, indicating muscle fatigue induced by load carriage. MPF also indicates the fatigue on TA was less in LD and DLC compare to the backpack only session. Three subjects' erector spinae (ES) data were contaminated possibly due to the interference from the backpack; hence, they are excluded in the analysis. The activity of the ES was significantly lower for S1 than all the other sessions but no

significant differences were observed in the MPF of the ES between different sessions. The activity of biceps femoris (BF) did not show a significant difference in both iEMG and MPF values between different sessions, while the signal quality of the rectus abdominis (RA) and upper trapezius (TRAP) were poor due to artifacts caused by fat deposits (RA) and the interference from the shoulder straps (TRAP); hence they are not presented.

Table 3.3 Comparison on the muscle activity (iEMG) and mean power frequency (MPF) between sessions (n=12)

$* p < 0.05$		BL	S1	S2	S3	p value		
						S1-S2	S2-S3	S1-S3
iEMG [a]	RF	0.59	0.97	0.89	0.84	0.19	0.33	*
	VL	0.72	1.10	1.01	0.94	0.11	0.06	*
	GM	0.74	0.96	0.89	0.85	*	0.13	*
	SOL	0.74	0.99	0.85	0.82	*	0.67	*
	TA	0.69	0.94	0.83	0.78	0.08	0.07	0.08
	ES	0.80	0.58	0.65	0.72	*	0.17	*
MPF [b]	RF	109.1	87.5	98.5	99.6	0.09	0.40	*
	VL	91.8	78.0	83.3	85.3	0.42	0.37	*
	GM	121.3	103.0	116.4	117.2	0.07	0.07	0.62
	SOL	139.2	133.8	138.8	141.0	0.11	0.36	0.14
	TA	102.2	96.3	101.2	101.5	*	0.81	*
	ES	89.0	57.8	68.6	68.2	0.49	0.49	0.93

Units: a) normalized on corresponding peak baseline value (unitless), and b) mean power frequency (*Hz*)

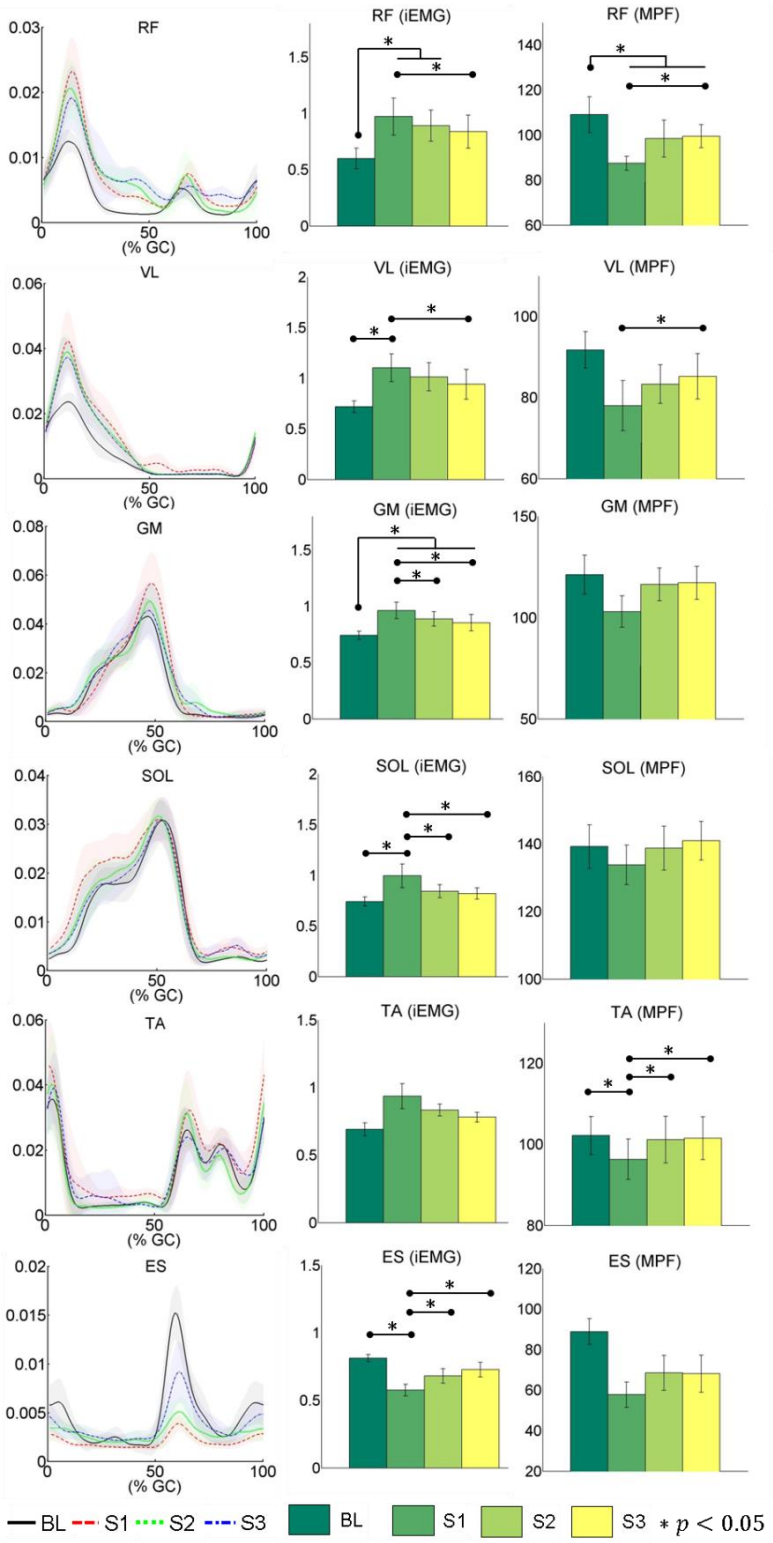

Figure 3.5 Average linear envelopes of EMG during different trials of a representative subject for 6 muscles (RF, VM, GM, SOL, TA, and ES), and group average of their integral (iEMG) and median power frequency (MPF)

3.4.5 Metabolic cost

The mass normalized oxygen consumption($\dot{V}O_2$/kg) and heart rate (HR) of the group average are presented in Figure 3.6. $\dot{V}O_2$/kg was significantly higher during loaded sessions compared to BL, thus reflecting subjects' increased metabolic expenditure when they carried the backpack load. When DLC was provided (S3), $\dot{V}O_2$ significantly reduced (percentage mean reduction of 8.7%) compared to S1. The heart rate increased in S1 compare to BL, but there was no significant difference observed between the other sessions, Table 3.4.

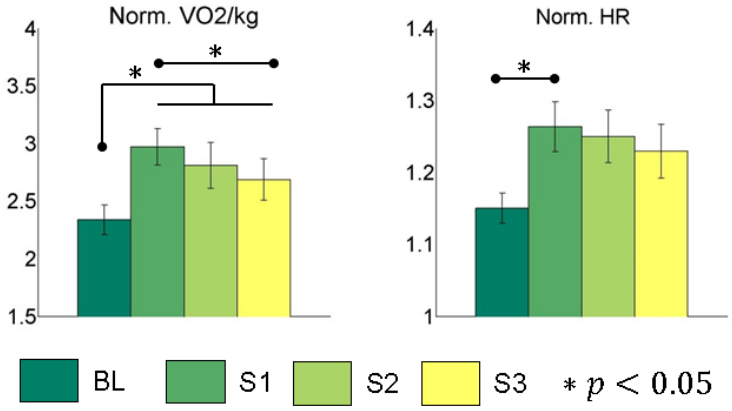

Figure 3.6 Group average of mass normalized volumetric oxygen consumption rate ($\dot{V}O_2$/kg) and heart rate (HR) during different trials over 16 minute time window. $\dot{V}O_2$/kg and HR were normalized on their corresponding values measured during rest (unitless)

Table 3.4 Comparison on the cardiopulmonary variables between sessions (n=12)

* $p < 0.05$	BL	S1	S2	S3	p value		
					S1-S2	S2-S3	S1-S3
$\dot{V}O_2$/kg [a]	2.485	3.133	2.964	2.863	0.12	0.07	*
HR [b]	1.150	1.264	1.249	1.229	0.31	0.20	0.35

Units: a) mass normalized then normalized on the value measured during resting subject-wise and b) HR is a dimensionless ratio of the value of the corresponding session to that from resting

3.5 Discussion

3.5.1 Reduced vertical excursion of backpack load

The peak vertical excursion of backpack was reduced between each loaded session, as was the goal of the device. This effect is the result of the passive suspension and is further improved with active compensation of the dynamic load. The device also resulted in an elevation of the mean vertical position of the backpack as it creates a gap between the shoulders and the shoulder pads, and DLC reduced the vertical excursion of the backpack while not affecting the peak vertical position from LD. The effect of this reduction in backpack motion is the main source of the changes discussed in the following sections.

3.5.2 Changes in gait and postural adaptations

While walking with load may necessitate changes in gait to produce stable walking, it may also be assumed that for each individual, their gait pattern has reached some optimization based on their body size, joint stiffness, susceptibility to injury, etc. From this statement, it can be reasoned that being able to reduce the effect of the load on the person and return them to a gait pattern closer to unloaded walking may reduce problems associated with load carriage. In line with previous studies on carrying a backpack load [12, 17, 28, 29, 35], subjects significantly increased stance-phase peak knee flexion and hip flexion of the leading leg, and hip extension of trailing leg when they walked with the backpack compared to unloaded walking. Gait kinematics support the idea that LD and DLC are capable of creating a gait more similar to unloaded walking as both S2 and S3 had peak angles of the hip and knee which were significantly different than S1 in the direction of BL. This can be most heavily attributed to LD as these

values of S2 and S3 were not significantly different from each other. However, the contribution of DLC is the primary factor in reducing ankle plantar flexion angle which occurs just following heel strike. This is tied to the reduction in peak vertical GRF at heel strike which was reduced with LD and further reduced with DLC, and which contributes to ankle plantar-flexion. The TA slows the change in ankle angle after heel strike to prevent excessive plantar-flexion, and so the reduction of TA fatigue in S2 and S3 may also be the result of reduced peak vertical GRF.

The increase in vertical pelvic excursion in the loaded sessions is related to the hip extension angle assuming an inverted pendulum model, as well as increased knee flexion at heel strike. Increased knee flexion at weight acceptance is associated with applying a braking force and distributing it over a longer time to reduce high impact loading of the body, causing a less rapid deceleration of the mass and as a result reducing the force seen by the body. This is in line with previous findings that the vertical excursion of pelvis increased with load carriage mainly due to lowering of the COM of the body during weight acceptance phase to increase body stability while absorbing the impact forces at heel strike [89]. These adaptations are shock absorbing strategies used by the human motor system to attenuate the increased impact forces at initial contact due to the added mass [17, 18, 19, 89, 90] and, in part, smoothen the transition of the weight in the forward direction during the early mid-support phase [16, 17, 22, 89]. With the load moving with the body (S1), the increased knee flexion achieves this purpose, which results in an increase in double support period, consistent with the previous studies [17, 22, 27, 89].

When the load is able to move separately, this compensation at the knee is reduced in S2 as the deceleration of the load is, to some extent, taken by the spring suspension, and further reduced in S3 when dynamic load was compensated. This is the result of the pack load having a smaller vertical excursion over the same frequency of walking; thereby less force is needed to

accelerate and decelerate the mass. This is further supported by the vertical and braking GRF, both in terms of the peak and loading rate. The reduction in these values could be caused by increasing knee flexion angle and double support period. However, knee flexion and double support period are reduced for S3, as are the peak and loading rates for the vertical and braking force. These reductions can then be accounted for by the use of the device and not through compensation at the knee. This is further supported by the reduction in knee extensor activity in S3. The trend of reduced stride length indicates that the increased hip extension is a result of the increased knee flexion for braking and also accounts for the vertical excursion of the pelvis. As the knee flexes with both feet on the ground, the contralateral hip must extend to account for the change which, in turn, lower the pelvis.

Reduced changes in temporal parameters also reflect a return towards unloaded gait characteristics. The addition of loads, both gravitational and dynamic, requires additional time to shift the loads over the base of support, thus, an increased stance time is typical in load carriage which is caused by increasing the double support period while decreasing the single support period [17, 22, 31, 89]. Such adaptations help shifting the load from one leg to the contralateral leg during the transition from the double support to single support phase (mid-stance), thereby enhancing body's stability during load carriage [16, 17, 27, 90]. In accordance with the literature, subjects significantly increased their double support period while decreasing single support period when they carried the backpack thereby resulting in a higher stance to swing ratio.

This increase in time to shift loads may be linked with the reduction in the unilateral activation of the ES, i.e., the left and right side of the ES do not activate at the same time. In unloaded walking, there is a large spike in the ES on the side of the push-off leg, as the pelvis shifts over and tilts obliquely to the stance leg. The ES acting unilaterally, as can be seen by the

single spike in activation during push off, is responsible for lateral flexion of the spine which helps keeping the posture upright to account for the pelvic tilt and shift. When loaded only (S1), the unilateral ES activation is decreased. This may be the result of having the weight supported solely by the shoulders, in which case lateral flexion of the spine would cause motion of the load and require increased energy to shift it from side to side as well as balance the moving load. When the device is used, the load is partially supported by the pelvis allowing the shoulders to more freely move. This freedom from load would then reduce the effect of the load on the torso reducing the penalty for swinging. Previous study have reported a bilateral reduction in ES activation (both left and right ES activations reduced) with backpack carriage and attributed it to the backpack producing a torque as would be supplied by the ES [35]. While they report reduction in ES activation, it is not clear if the activation was bilateral (both muscles activate at the same time). Hence, the above claim made on the changes in the ES activation stands only as a theory.

Similarly other studies have reasoned along the same lines, where walking with a backpack increases forward lean of the trunk to bring the backpack mass close to the body COM to maintain the combined COM of the upper body and carried load over the feet [12, 18, 27, 90], and to keep the backpack COM lower to increase the stability of the body-plus-load system [17, 27, 89]. Our results do not seem to reflect this idea. With LD and DLC, torso flexion was decreased while the mean pack position also increased as well, which are in line with the previous findings [35, 91]. On the other hand, the change in the mean vertical position of backpack between sessions was 1 to 2 cm, and this small change does not seem to account for the changes in torso flexion angle we observed. It is more likely that the load distribution and load pathway play a greater role on the changes in torso flexion. Bloom et al. observed that the

use of a hip belt with a pack reduces flexion angle [91]. A hip belt alone would not change the COM location or the extension torque about pelvis created by the posterior offset of backpack COM. Then, the change in flexion angle could be due to the reduction of the force transmitted through the spine. Small torso flexion reduces lordosis of the lumbar spine, which changes how load is transmitted between vertebrae. It has been shown that compressive follower loads, i.e., loads tangent to the curve of the spine, increase the load capacity of the spine in-vitro [92]. With a reduction in lordosis due to torso flexion, the vertical component of the backpack load acts more tangent to the curve of the spine increasing the load carrying capacity without straining the soft tissue. This strategy can be thought of as an alternative reason why one might flex more when loaded through the shoulders. By reducing the force transmitted through the spine by distributing it with the pelvis, and then further reducing the dynamic loads, subjects do not need to change postures to increase the load carrying capacity of their spine.

3.5.3 Metabolic benefits

One of the hypotheses of this experiment was that by using the device to reduce the dynamic loads of a backpack we would be able to see a metabolic benefit from the user, even if the session was only 15 minutes long. This hypothesis is based on previous work which found that backpack load induces significant peak dynamic forces on the body and increases the metabolic cost of walking [13, 20]. Recent studies showed that reducing suspension stiffness of a backpack reduces the peak dynamic forces acting on the body [37, 93, 36]. Rome et al. also showed a decrease in the peak vertical dynamic force (82%) and metabolic cost (6.2%) by reducing the vertical motion of a backpack with respect to the human body [38]. Depending on the suspension stiffness values, it induces in-phase (very compliant) or out-of-phase (stiffness

tuned to be in near-resonance with walking) motion of the backpack with respect to the body motion. Studies have shown a reduction [38] or an increase [37] in metabolic cost as a result.

This is consistent with our finding of an 8.7% reduction in $\dot{V}O_2$ consumption between S1 and S3 with reduced backpack vertical excursion. This is higher than what was reported with using a "suspended-load" backpack (6.2%) [38] or a flexible pack (3.8%) [37]. Such a difference may be attributed to the load distribution between the shoulders and the pelvis. A backpack frame and hip belt was shown to transfer 30% of load from the shoulders to the pelvis regardless of load magnitude between 14 and 41 kg [94]. If a hip belt was used in a "suspended-backpack" design, the load distribution between the shoulders and the pelvis would still be similar to that of a frame backpack with a hip belt. Thus, the higher metabolic saving presented in this study may suggest that more equally distributed load between the shoulders and the pelvis can further increase the metabolic efficiency. This reinforces the findings of Grabowski *et al.* where the vertical excursion of upper torso in human gait requires work from the lower limb to redirect and accelerate body mass. This extra work incurs a significant metabolic cost during normal walking and the additional load on the upper torso further necessitates a higher energy cost [95].

Contributing factors to this reduction are the reduction of knee extensor activation at weight acceptance and reduced activation of the ankle plantar flexors. While reduction in plantar flexors did not show a change in propulsive ground reaction forces, their lower activation would still contribute to reduced oxygen consumption. The HR increased BL to S1, but only a decreasing trend was found from S1 to S3, hence, HR will not be further discussed as it adds little to the overall discussion of the metabolic benefits.

3.5.4 Reduced risk factors for injury

Reducing injury is a major concern with load carriage, particularly in applications for which this device was designed. The most direct risk factor for injury which has been reduced with the use of the device is the reduction in peak and loading rate of the vertical and braking GRF. This has the implication of lower impact force on the feet and the joint loading rate which can potentially reduce repetitive strain injuries on the lower limbs, such as stress fractures, foot blisters, muscle soreness, etc. [12, 14, 16, 17]. Similarly, reduced lower limb muscle activity and muscle fatigue while using the device can reduce the potential muscle strain and overuse injuries. Fatigue of the TA reduces ground clearance which may lead to tripping. TA fatigue is reduced with the device which can lower the possibility of this occurring. Additionally, the fact that the lower limb muscle fatigue was reduced with the device in addition to the net metabolic benefit implies general fatigue would lessen as a result of physical exertion.

Another important result is the reduction in torso flexion. It is thought that the reason for this change in torso flexion is to bring the combined COM over the base of support [12, 27, 90]. However, an increase in forward lean has been hypothesized to cause stress on the back muscles, ligaments, thereby leading to back injuries [12, 15, 6, 89]. With LD, torso flexion was reduced from S1 and this was further reduced by DLC. This may reduce the prevalence of back injuries. Distributing the load between the shoulders and pelvis attenuates the pressure on the shoulders and spine. This may reduce incidence of rucksack palsy, lower back pain, etc. [12, 13, 18].

3.6 Conclusion

In this chapter, the WEBS was tested on twelve human subjects to address the following research question, "What are the biomechanical and physiological effects of load distribution and dynamic load compensation of a backpack on the human body during backpack load carriage?" It was hypothesized that load distribution and dynamic load compensation during backpack load carriage, gait and postural adaptations typical in backpack load carriage, and the user's muscular effort and metabolic cost would be reduced. This hypothesis was supported by biomechanical and physiological measurements on a group of young healthy subjects, as they walked on a treadmill under 4 different conditions: unloaded, with a backpack load of 25% of their body weight supported on the shoulders, with the same load distributed between the shoulders and the pelvis, and with dynamic load compensation in addition to load distribution.

The experiment protocol was described in Section 3.2. Section 3.3 presented statistical analysis method carried out on dependent variables using a repeated measure ANOVA technique to determine the statistically significant differences of dependent variables between conditions. The results presented in Section 3.4 revealed the effects of load distribution and dynamic load compensation: reduction in gait and postural adaptations, muscle activity, vertical and braking ground reaction forces, and metabolic cost. Based on these results, Section 3.5 discussed the potential of the wearable upper body suit to reduce the risk of musculoskeletal injuries and muscle fatigue associated with heavy backpack loads, as well as reducing the metabolic cost of loaded walking.

Chapter 4

Robotic Spine Exoskeleton (ROSE) for correction of spine deformities

4.1 Introduction

In this work, the torso exoskeleton, Robotic Spine Exoskeleton (ROSE), was designed to overcome the limitations of current spine braces due to their rigid, static, and non-sensorized designs. The ROSE consists of two parallel robotic platforms connected in series that can snugly fit to different cross-sections of a human torso. It has a total of twelve active degrees of freedom and can dynamically modulate either the posture of or the forces applied to different cross sections of the human torso. The chapter is organized as follows. Section 4.2 describes the architecture and the design process of the ROSE. Section 4.3 details the position and force controller implemented in the ROSE. Section 4.4 demonstrates the performance of the two controllers through experimental evaluation. Section 4.5 summarizes and concludes the chapter.

4.2 Design

The ROSE consists of three rings which can be adjusted to fit snugly on the human body, at the pelvic, thoracolumbar, and thoracic regions of the torso, Figure 4.1(a). A six degree-of-freedom

parallel-actuated module is attached between the pelvis and the thoracolumbar rings, and between the thoracolumbar and the thoracic rings, Figure 4.1(b). Each module contains six limbs with UPS configuration, i.e., a universal joint at the bottom, an actuated prismatic joint, and spherical joint at the top, Figure 4.1(c). Each actuated limb integrates position and force sensors which can be used for force or position control of one ring with respect to its adjacent ring. Each module is independently capable of translating and rotating in 3-dimensions (maximum ±2 cm in translation and ±10 degrees in rotations). It can also exert 3-dimensional forces and moments (±100 N in forces and ±10 N-m in moments). With this architecture, the thoracolumbar ring can be controlled with respect to the pelvic ring either in force or position mode. Similarly, thoracic ring can be controlled with respect to the thoracolumbar ring in either position or force mode. This architecture is designed for treatment of C-type scoliosis curves, where the apex of the curve lies underneath the thoracolumbar ring. The system is portable and uses an NI myRio-1900 controller (National Instruments, Austin, TX) programed in Labview (National Instruments, Austin, TX) with three custom-made electronics boards for real time control of the motors and for sensor communications. The detailed hardware specifications are provided in Appendix C.

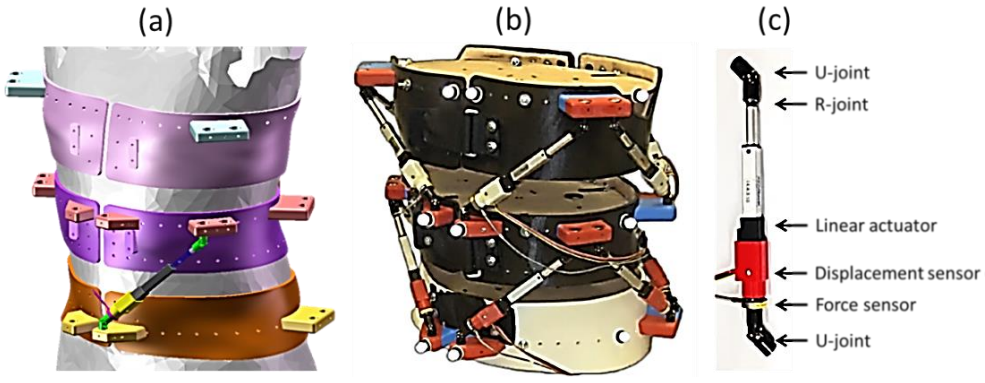

Figure 4.1. (a) 3D CAD model of the ROSE, (b) physical model of the ROSE, and (c) actuated limb design

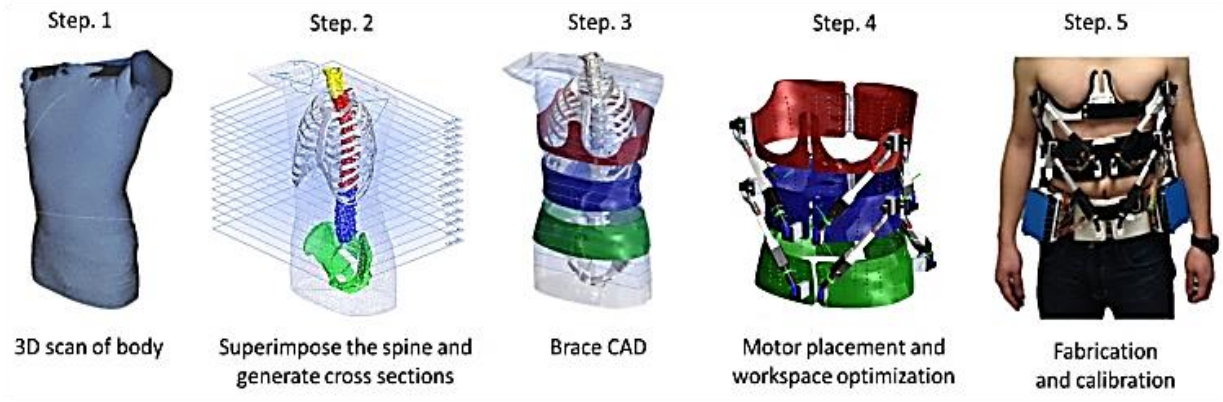

Figure 4.2 The design process of the robotic spine brace; Step 1: 3D scan of the body, Step 2: superimpose the spine 3D CAD to the 3D scan of the body, Step 3: design the rings of the ROSE, Step 4: determine the location of the rings and actuators and optimizing the workspace, Step 5: fabrication and calibration

Figure 4.2 illustrates the design process of the ROSE. In Step 1, a 3D scan of the human torso is obtained by optical scanning. In Step 2, a 3D CAD model of the human torso is constructed using the 3D scan data. Then, a 3D CAD model of the spine is scaled and superimposed to obtain the approximate location of the spine vertebrae on the torso model. In Step 3, the locations and sizes of the three rings are determined. Then, 3D CAD models of the rings are designed to fit snugly on to the human torso at the pelvis, thoracolumbar, and thoracic regions. In Step 4, the placements of the six limbs on the rings are optimized to achieve the desired workspace between the rings. In Step 5, the rings and other mounting components are fabricated (3D printing using ABS plastic material) and assembled. Finally, the ROSE is calibrated on a person by adjusting the initial positions of the rings and tuning the control gains.

4.3 Control

Two control modalities – position control and force control – are implemented at the joint space. Sensors on each limb give real time joint position and force feedback to the controller that allows for closed-loop control in either mode. The upper and lower parallel platforms are controlled independently. The control topology for position and force control are shown in Figure 4.3 and Figure 4.4, respectively. Parameterization, kinematics, and trajectory planning of the ROSE are described in Appendix D.

The position controller consists of a high level controller and a low level controller, Figure 4.3. The trajectory planner first generates the desired motion of the platform. The high level controller then maps the desired motion of the platform in Cartesian space ($\mathbf{X_d}$) into the joint space variable ($\mathbf{q_d}$) at 200 *Hz* using inverse kinematics. $\mathbf{X_d} = [P_x, P_y, P_z, \psi, \theta, \phi]^T$ is the vector of pose variables of the moving platform and $\mathbf{q_d} = [q_i, q_2, \dots, q_6]^T$ is the vector of actuated joint. Part of the high level controller also computes the Cartesian position and force vectors, **X** and **F,** of the platform using the joint position/force feedback via forward kinematics and the robot's Jacobian. This allows the Cartesian forces of the platform to be measured during position control. The low level controller, consisting of individual PID controllers for each joint, receives the desired joint position $\mathbf{q_d}$ from the high level controller and performs the closed-loop control on the joint position at 500 *Hz*. The error is measured as the difference between the desired joint position and the actual joint position. The controller gains of each actuator were experimentally tuned.

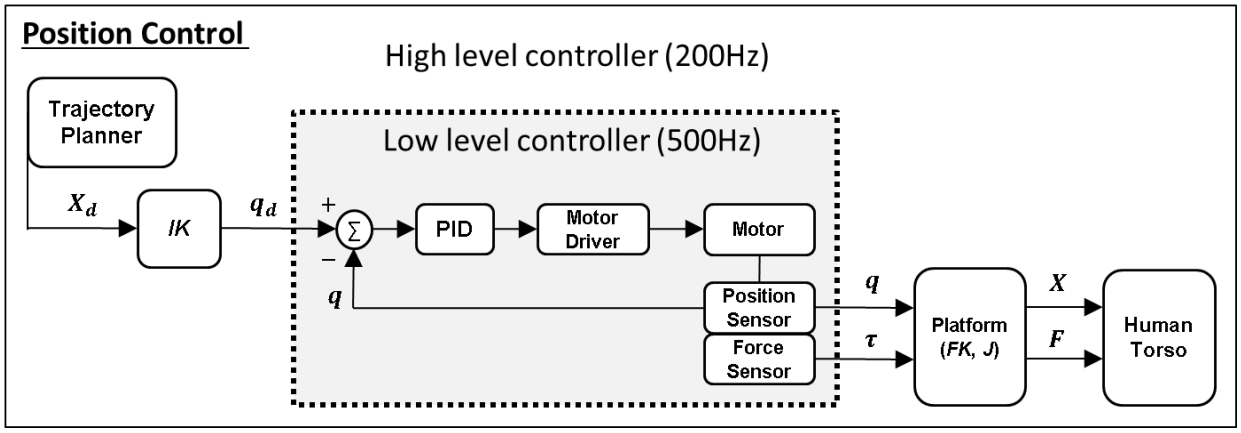

Figure 4.3 Position controller implemented in the joint space; *IK* and *FK* represent inverse kinematics and forward kinematics, respectively, and *J* represents Jacobian

The force controller, Figure 4.4, consists of a high level and a low level controller similar to the position controller topology. The high level controller, implemented at 200 *Hz*, maps the desired force in task space ($\mathbf{F_d}$) to the desired joint forces ($\boldsymbol{\tau_d}$) using the formula $\boldsymbol{\tau_d} = (\mathbf{J}^{\mathbf{T}})^{-\mathbf{1}}\boldsymbol{F_d}$, assuming non-singular configurations within the operating workspace where $\boldsymbol{\tau_d} = [\tau_1, \tau_2, \ldots, \tau_6]^{\mathrm{T}}$ is the vector of actuator forces, and $\mathbf{F}_{\mathrm{d}} = \left[\mathrm{F_x}, \mathrm{F_y}, \mathrm{F_z}, \mathrm{T_x}, \mathrm{T_y}, \mathrm{T_z}\right]^{\mathrm{T}}$ is the vector of output Cartesian forces from the robot. Such a mapping uses the robot's Jacobian in its current configuration which is calculated in real time using joint position feedback. This allows the Cartesian forces to be controlled based on the pose. The low level controller receives the desired joint forces computed in the high level controller, and uses an open loop reference feed-forward (FF) term ($\boldsymbol{\tau}_{\mathrm{FF}}$) with unit gain and a closed-loop PID term ($\boldsymbol{\tau}_{\mathrm{PID}}$) to follow the desired forces of each joint. The unit gain for the FF term and PID gains were experimentally tuned.

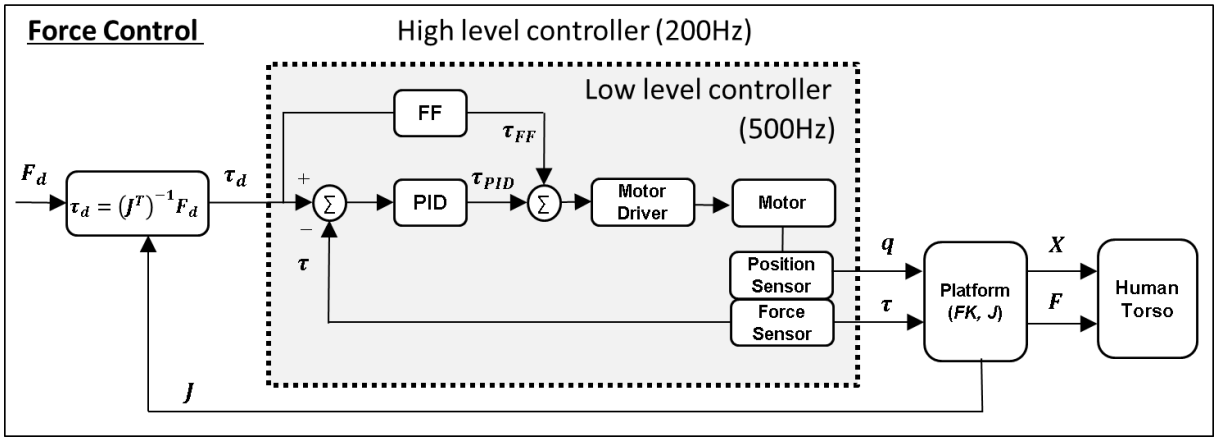

Figure 4.4 Force controller implemented in the joint space; *FK* and *J* represent forward kinematics and Jacobian, respectively.

4.4 Controller Evaluation

This section presents experimental evaluations of position and force controllers implemented in the ROSE. The linear actuator in each limb of the ROSE has an integrated potentiometer that feedback the joint displacement from which the Cartesian pose of each ring is computed using forward kinematics. Infrared markers were placed on the rings to measure their position and orientation with a motion capture system (Vicon Motion Systems®, Oxford, UK). The position controller was evaluated by moving the ROSE through seven different modes of motions: 3-point-pressure motion, flexion, lateral bending, rotation follow, rotation mirror, translation follow, and translation mirror. The 3-point-pressure mode mimics the traditional 3-point-pressure correction method used in the spine braces which involves rotation about *z* and translation about *x* in the transverse plane. Flexion and lateral bending modes evaluate the bending motion capability in a brace. The last series of modes were carried out for isolated translations and rotations. In these modes, the upper parallel-module performed either the same task (follow) or the opposite task (mirror) as the lower parallel-module.

The motion was recorded through potentiometers on the motors as well as the motion capture system where the translation and rotation of the middle and top segments relative to the neutral position were recorded and analyzed with respect to the bottom coordinate frame. Figure 4.5 shows motion tracking results verified using a motion capture system for 3-point-pressure motion trial. The position controller was able to follow all paths with less than 0.98° of average error for all tested trajectories, Table 4.1. For translational motions, the average positioning errors were in the sub-millimeter range.

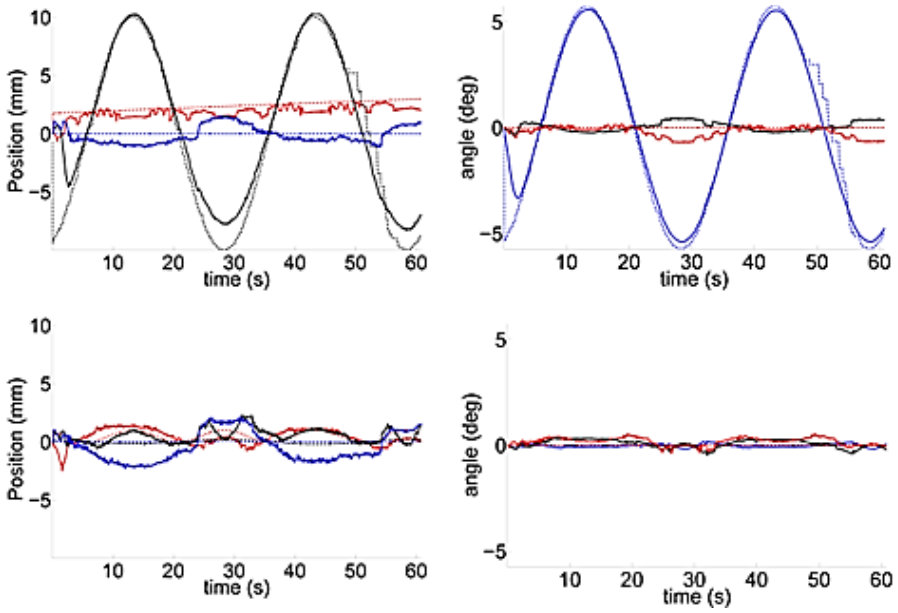

Figure 4.5 Graphical representation of the command (dashed) and Vicon (solid) results from the 3-point motion test. Rotations and translations about x, y, and z are represented by black, red and blue respectively; (top row) the lower parallel-module and (bottom row) the upper parallel module

Table 4.1 Position and orientation error of the middle and lower segment origin from seven motions tested

Middle	x (mm)	y (mm)	z (mm)	ϕ (deg)	θ (deg)	ψ (deg)
three-point	0.52 ± 0.34	1.13 ± 1.22	0.65 ± 0.36	0.37 ± 0.43	0.18 ± 0.12	0.23 ± 0.21
flexion	0.59 ± 0.31	1.28 ± 0.71	0.57 ± 0.38	0.07 ± 0.05	0.15 ± 0.10	0.43 ± 0.27
lateral bending	1.35 ± 0.73	0.28 ± 0.16	0.85 ± 0.54	0.14 ± 0.08	0.29 ± 0.27	0.21 ± 0.16
rotation follow	0.67 ± 0.67	0.83 ± 0.47	0.55 ± 0.27	0.09 ± 0.08	0.15 ± 0.13	0.18 ± 0.13
rotation mirror	0.73 ± 0.67	0.88 ± 0.52	0.72 ± 0.35	0.07 ± 0.05	0.17 ± 0.14	0.18 ± 0.14
translation follow	0.26 ± 0.12	0.42 ± 0.20	0.32 ± 0.18	0.08 ± 0.04	0.04 ± 0.03	0.12 ± 0.08
translation mirror	0.23 ± 0.12	0.47 ± 0.26	0.32 ± 0.25	0.10 ± 0.02	0.05 ± 0.02	0.10 ± 0.06
Top						
three-point	0.53 ± 0.39	0.61 ± 0.48	1.18 ± 0.57	0.07 ± 0.04	0.18 ± 0.11	0.22 ± 0.13
flexion	0.54 ± 0.44	6.99 ± 3.77	1.55 ± 0.89	0.16 ± 0.09	0.09 ± 0.06	0.98 ± 0.63
lateral bending	6.74 ± 3.90	0.84 ± 0.52	1.46 ± 1.23	0.40 ± 0.21	0.55 ± 0.51	0.46 ± 0.22
rotation follow	2.02 ± 1.22	2.54 ± 1.29	0.80 ± 0.39	0.15 ± 0.15	0.23 ± 0.20	0.17 ± 0.24
rotation mirror	1.29 ± 0.72	1.51 ± 0.82	1.06 ± 0.47	0.11 ± 0.09	0.12 ± 0.10	0.15 ± 0.09
translation follow	0.85 ± 0.60	0.93 ± 0.49	0.46 ± 0.26	0.06 ± 0.04	0.05 ± 0.05	0.18 ± 0.13
translation mirror	0.31 ± 0.26	0.25 ± 0.24	0.73 ± 0.39	0.14 ± 0.03	0.06 ± 0.06	0.14 ± 0.08

The force controller evaluation utilized a test bed wherein the middle and bottom segments were attached to each other using a 6-axis force/torque sensor (Mini45, ATI) in the brace's neutral position to measure the relative force and moment in a given pose of the middle segment relative to the bottom segment, Figure 4.6. The brace was then driven to follow a force/torque profile: (1) unidirectional force or torque; -30 N < F_x, F_y, F_z < 30 N and -1.5 Nm ≤ $M_x, M_y, M_z \leq$ 1.5 Nm, 2) and (2) three dimensional force and torque (F_x, F_y, M_z). The calculated force/torque from the load cells in the brace were then compared to the force/torque sensor data to determine sensor error, and were also compared to the commanded force/torque profile to evaluate tracking error. Figure 4.7 shows a representative force tracking result when a set of planar desired forces and moments were commanded to the system. Both uni-directional and three dimensional force control demonstrated good tracking performances with less than 4% and 7% tracking errors, respectively.

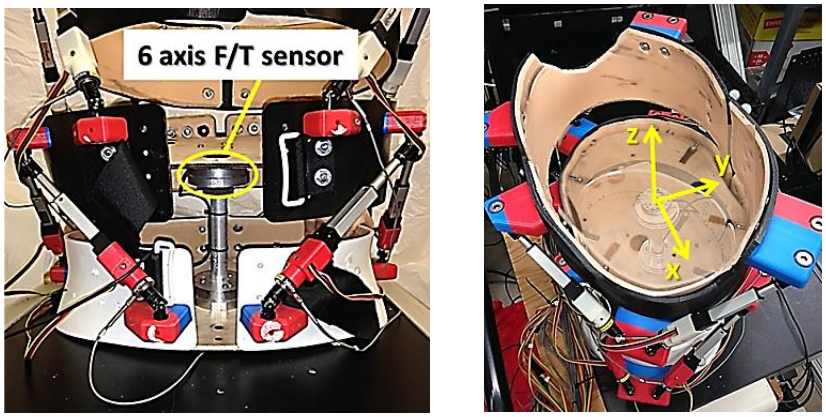

Figure 4.6 Test-bed for force controller evaluation

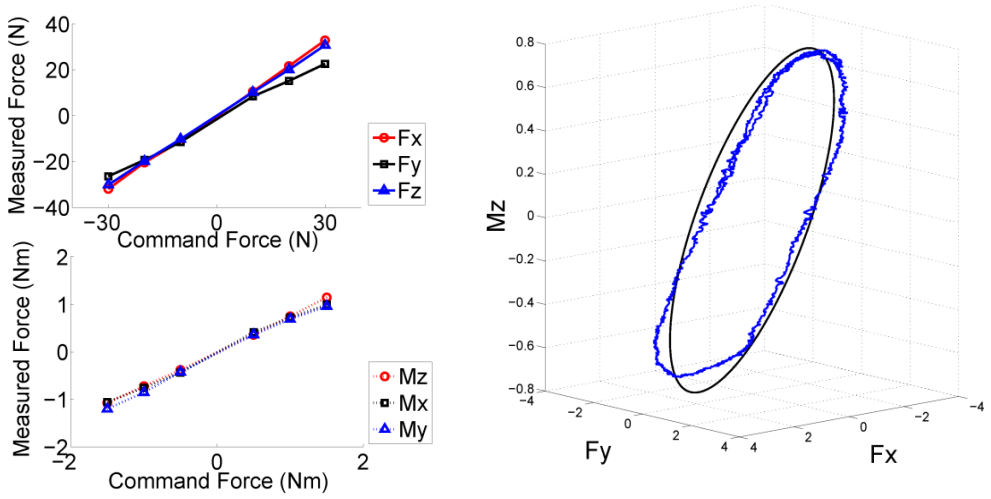

Figure 4.7 (right) Graphical representation of the command force (dashed-black) and measured force (solid-blue) from ATI F/T sensor; (a) One dimensional force, and (b) three dimensional force

4.5 Conclusion

In this chapter, the design, control, and evaluation strategies of the ROSE are presented. The ROSE is capable of controlling and monitoring either the forces or the poses that it imposes on the body in 3-dimensions. It consists of a series of rings that are snugly attached to the human body and conform to cross sections in the torso. Forces and moments are applied to each ring using actuators mounted on adjacent rings. The rings are parallel-actuated using the Stewart-

platform design with closed-loop control of the actuators using joint position/force data measured by integrated sensors. These were described in Section 4.2 and Section 4.3. The accuracy of tracking the commanded position or forces through two control modes was evaluated experimentally using a camera based motion capture system and using six axis force-torque sensor which showed good tracking performance (demonstrated in Section 4.4). The next chapter will present the human subject study conducted using ROSE to evaluate the feasible range of in-brace torso motion, the ability to control forces applied on the human torso at various postures, and the feasibility of characterizing the three dimensional stiffness of the human torso.

Chapter 5

Experiment of ROSE with human subjects

5.1 Introduction

This chapter presents the human subject experiment using the ROSE to evaluate the feasible range of torso motion while wearing ROSE, controlling a constant force at various postures, 3-point-pressure correction, and characterizing three-dimensional torso stiffness. Ten healthy male adults (age 29±6 years, height 1.73±0.05 m, torso length 0.31±0.046 m, and weight 73.2±4.5 kg) participated in this study. The experimental protocol was approved by the Columbia University Institutional Review Board and informed consent was obtained from all participants before conducting the experiments. All subjects were between 18 and 35 years of age without any history of back pain or spine injuries, cardiopulmonary conditions, neurological or physical impairments, or other orthopedic conditions that could affect natural motions of the torso and the spine.

The chapter is organized as follows. Section 5.2 presents the protocol and methods used in the experiment. Section 5.3 presents the results. Section 5.4 discusses the results and limitations of the study. Section 5.5 concludes the chapter.

5.2 Protocol

The study consisted of four sessions with the length of each session and breaks between sessions shown in Figure 5.1(a), and the coordinate frame used in the study shown in Figure 5.1(b). All sessions were performed with the subjects in a relaxed, seated position. Before the beginning of the first session, the size of the brace was adjusted to fit the subject, and then any gaps between the brace and the body were filled with padding.

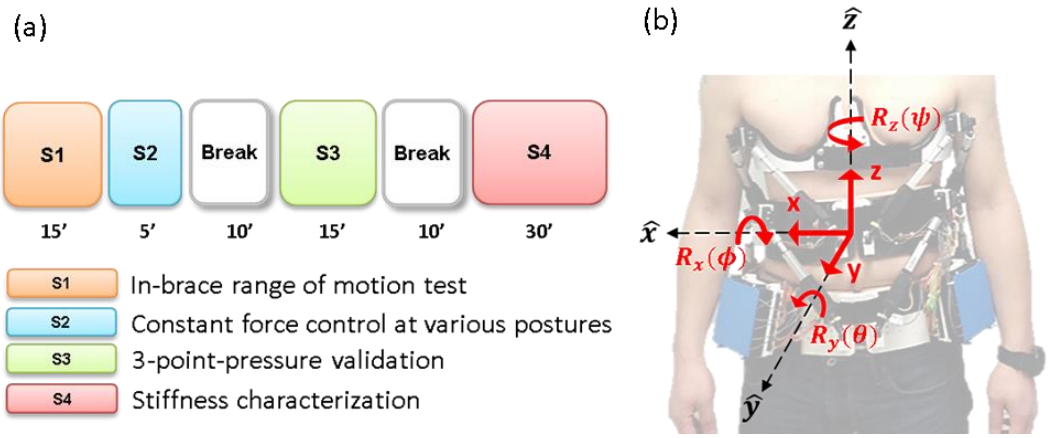

Figure 5.1. (a) Human subject experiment protocol and (b) torso coordinate frame used in this study

Session 1 (S1) measured the feasible range of torso motion during in-brace and no-brace conditions. A motion capture system (Vicon Motion Systems®, Oxford, UK) was used to record torso kinematics, Figure 5.2. Reflective markers were placed on the subjects' anterior superior iliac spines, sacrum, sternoclavicular joints, and the inferior border of the manubrium. For each of the two conditions, subjects were asked to move their torso as far as they could in frontal (lateral bending), sagittal (flexion/extension), and transverse (vertical rotation) planes. During in-brace range of motion (ROM) testing, the brace was nearly transparent to users and applied

minimal forces on their body. The maximum angle between the pelvis and the sternum for six directions were compared between in-brace and no-brace conditions.

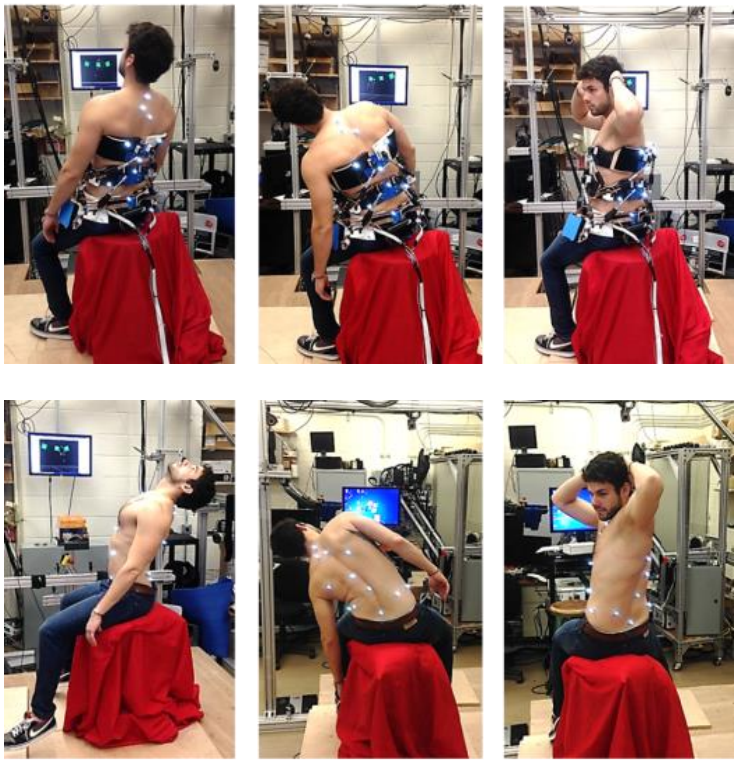

Figure 5.2 Session 1: the range of motion test with and without the ROSE

The second session (S2) evaluated constant force control at various postures of the torso. While allowing for a wide range of natural motion of the torso without exerting a force is a good feature to have to allow user's activities of daily living (ADL), it doesn't correct scoliotic spines. Therefore, if corrective forces can be provided to the torso in various pose configurations, treatment effect can also be achieved. To validate this idea, a constant force ($F_x = -50N$) was commanded while the subject was wearing the brace and performing the same range of motion

test in S1. Forces were measured during these motions and compared with those measured during S1 (transparent mode).

The third session (S3) evaluated a spine correction method called "3-point-pressure", which is used in most rigid braces [63]. This method applies corrective forces at the apex of the abnormal curves of the spine, particularly by applying translational and rotational displacements in the transverse plane. Our aim was to apply the same method on healthy individuals using ROSE, and evaluate the forces exerted on the torso. To do this, the middle segment (thoracolumbar ring) of the brace was positioned at the subject's T-10 vertebrae level and the brace controlled the displacement of this segment about the transverse plane (x, y) and the rotation about the z axis (ψ) with respect to the bottom segment. The top segment was controlled to be held in a stationary position with respect to the bottom segment, Fig. 8. Six different values of displacements were applied at the same time in x, y, and ψ : translation from -7.5 to 7.5 mm in 2.5 mm intervals, and rotation from -0.075 to 0.075 radian in 0.025 radian intervals, Figure 5.3. Each set of measurements was repeated three times and the measured forces were averaged over the group.

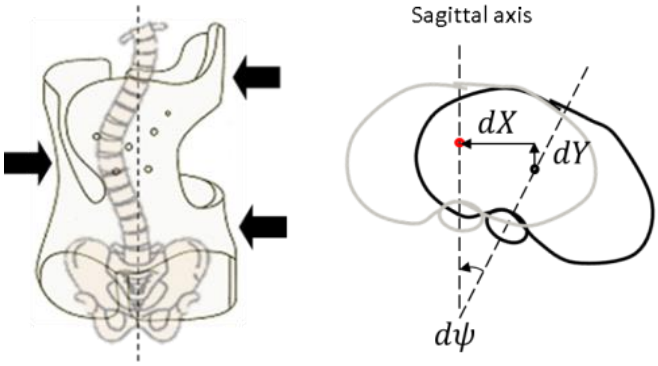

Figure 5.3 3-point-pressure method evaluated using the ROSE; planar displacements were applied with varying magnitude and directions, and forces were measured

The capabilities of the ROSE allow us to explore the elastic behavior of human torso to determine the force/displacement relationship of the human torso. To validate this idea, the fourth session (S4) characterized the stiffness of the torso through a set of force-displacement measurements. The ROSE applied unidirectional displacements at the T-10 vertebrae level of the torso on the subject while the subject was sitting comfortably on a chair. Displacements were applied individually for each degree of freedom from -15 to 15 mm in 5 mm intervals for translation, and from -0.15 to 0.15 radians in 0.05 radian intervals for rotation. All other degrees of freedom were fixed to the neutral position. As these displacements were applied, both position and forces were measured simultaneously, for one second at 100 *Hz*. The collinear stiffness terms were calculated by measuring the force collinear to the applied displacement. Each displacement was repeated three times, and the mean and standard deviation of measured forces were then calculated. The rate of displacement used in each test was 7 seconds per cycle, consisting of 3 seconds of ramp (zero initial position to the desired displacement), followed by 1 second recording (at the desired displacement), then 3 seconds of ramp (desired displacement to zero initial position) which was approximately 0.15 *Hz* per cycle to obtain quasi-static force-displacement relationships. This speed is close to the lower range of the test speed (0.1 *Hz*) recommended for spinal in vitro force-displacement testing [96]. The means and standard deviations of collinear stiffness were obtained over the group.

5.3 Results

5.3.1 Feasible range of motion with the brace

The range of motion of the torso between in-brace and no- brace conditions were compared, and the percentage of the subjects' range of motion during in-brace test was calculated with respect to the no-brace test. The results show that the subjects were able to achieve a majority of their natural range of motion while wearing the brace, Figure 5.4. This implies that the brace can accommodate many normal activities of daily living (ADL), such as tying one's shoes or picking something up from the ground.

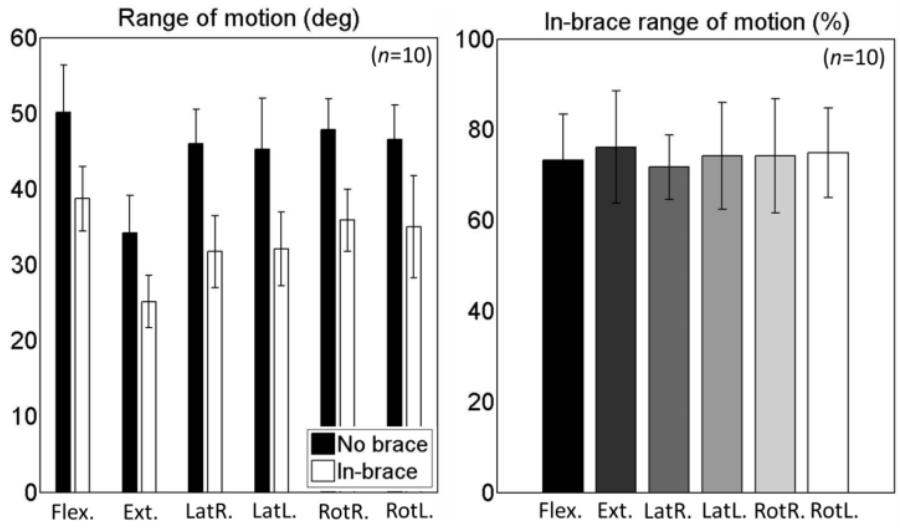

Figure 5.4 Feasible range of motion while wearing the brace compared to subjects' natural range of torso motion; (left) mean and standard deviation between the two conditions, and (right) average in-brace range of motion expressed as a percentage of no-brace range of motion

5.3.2 Constant force control during motion

In session 2, a constant force ($F_x = -50N$) was controlled during motions and compared with the forces measured during the same motions in the transparent mode (S1). The results showed that in transparent mode (S1), the brace allowed torso motions while maintaining applied forces close to zero. With constant force control (S2), the brace was able to maintain constant forces at various torso poses and during transitional periods between poses. Some forces that were controlled to be zero increased at the start and at the end of the motion but these were expected transient responses. Once the motion reached steady-state (quasi-static pose), those forces started decreasing and were reduced to zero, Figure 5.5. The mean values of the forces during the motions under these two modes were averaged over the group, and mean and standard deviations are shown in Figure 5.6. It was shown that for all subject tested, the magnitude of the controlled forces was close to what was commanded, which validates performances of both the transparent mode and constant force control mode. This result also suggests that the ROSE can correct abnormal postures of the torso while allowing for a range of motions.

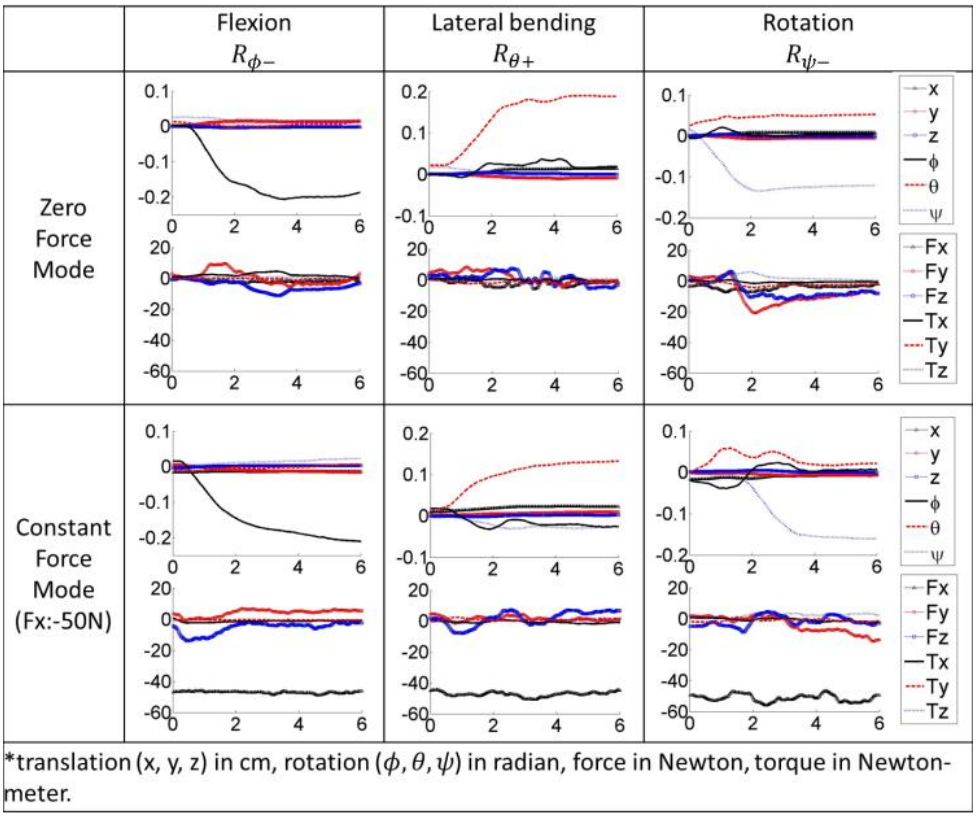

Figure 5.5 Comparison on forces exerted on the body during in-brace motions between transparent mode and constant force control mode of a representative subject

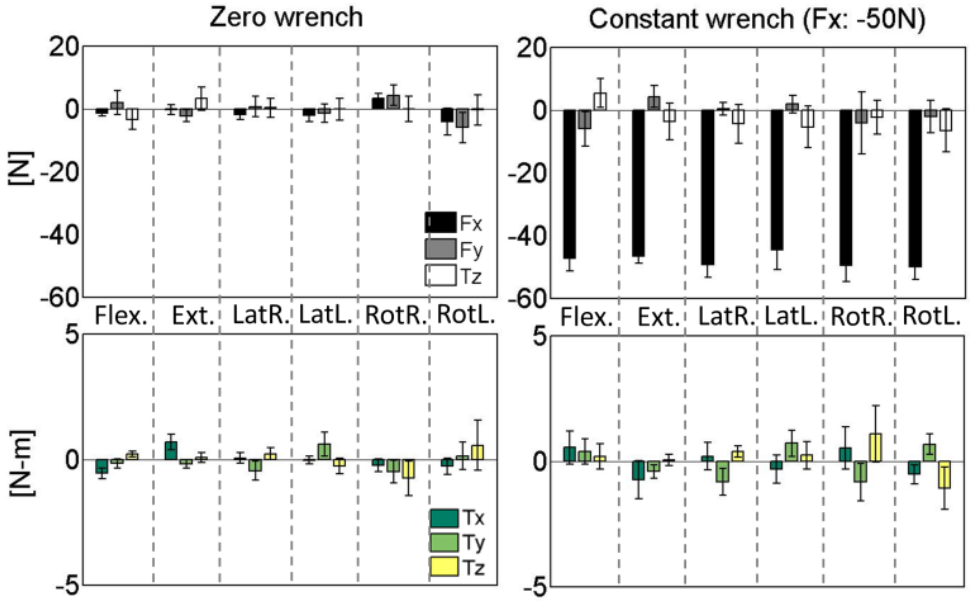

Figure 5.6 Group mean and standard deviation of the forces during six different in-brace motions between transparent mode and constant force mode

5.3.3 3-point-pressure validation

The group average for 3-point-pressure validation using the ROSE is shown in Figure 5.7. As expected, the direction and magnitude of forces collinear to the input displacements (F_x, F_y, T_z) were proportional to those of the input displacements. Interestingly, the planar displacements not only resulted in collinear forces but also induced forces in other directions, specifically the moment about x and y axes of the applied translational input displacements. This indicates "coupling effects" of the forces between the degrees-of-freedom which suggests the need to investigate 3-dimensional elastic behavior of the human torso when it is subjected to external displacements.

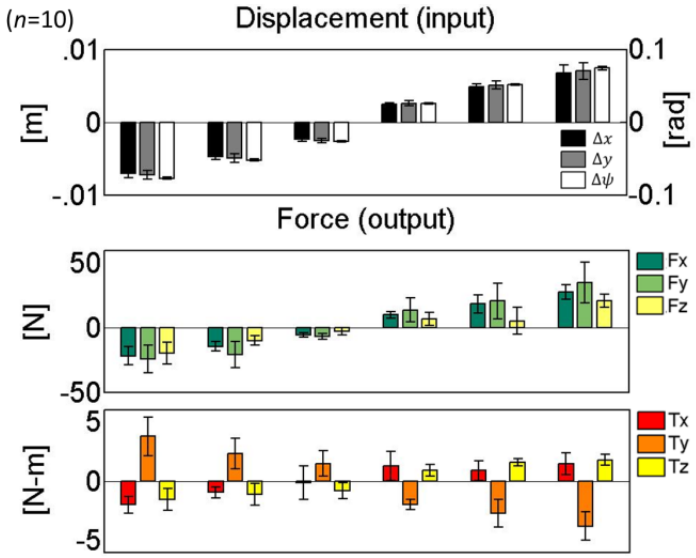

Figure 5.7 3-point-pressure validation; planar displacements (x, y, ψ) induced 3-dimensional forces

5.3.4 Stiffness characterization

The force-displacement relationship over the range of applied displacements was nearly linear for all degrees-of-freedom. Figure 5.8(a) shows a representative subject. The collinear stiffnesses averaged over the group are shown in Figure 5.8(b). The translational stiffness was highest in the z direction (superior/inferior) followed by the stiffness in the x direction (medial/lateral) and then the stiffness in the y direction (anterior/posterior). The rotational stiffness was highest in θ direction (lateral bending) followed by the rotational stiffness in ϕ direction (axial rotation) then the rotational stiffness in ψ direction (flexion/extension). These trends found in the relative magnitudes among the translational stiffnesses ($K_z \gg K_x > K_y$) and rotational stiffnesses ($K_\theta \gg K_\phi > K_\psi$) were in accordance with those reported in the literature where the collinear stiffness was experimentally computed through in-vitro human spine force-displacement measurement [97, 4], Table 5.1. The agreement in these trends suggests that the human spine - as it is the primary load bearing element of the torso - may be the biggest contributing factor in determining the stiffness of the human torso.

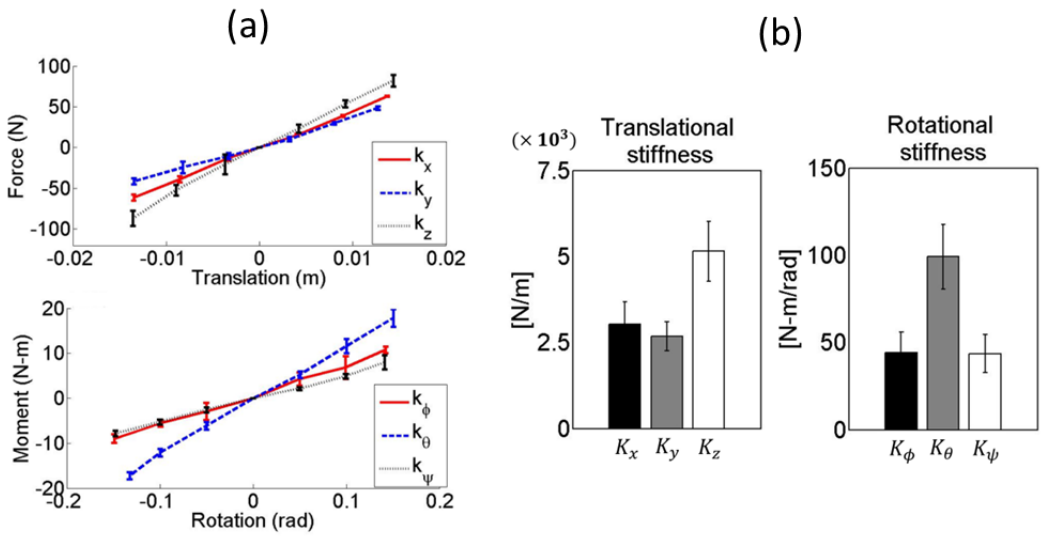

Figure 5.8 (a) Force-displacement mapping of a torso at T-10 vertebrae level of a representative subject; subscript followed by k indicates the stiffness about the corresponding degree of freedom, and (b) Group mean and ± 1 standard deviation of collinear stiffnesses of human torso at T-10 vertebrae location (n=10)

Table 5.1 Relative magnitudes of the translational stiffness terms and rotational stiffness terms measured from human torso in this study, compared with those measured from the spine vertebrae in other studies [97, 4]

	Tension (+Fz)	Compression (-Fz)	Ant. Shear (+Fy)	Post. Shear (-Fy)	Lat. Shear (Fx)	Flexion (-Mx)	Extension (+Mx)	Lat. Bend. (My)	Axial Rot. (Mz)	
Stiffness Coefficient (Lumbar)	770	2000	121	170	145	1.36	2.08	1.75	5.00	White et al.
	-	4737	157	181	299	3.0	3.0	4.1	2.7	Costi et al.
* N/mm for forces and Nm/deg for moments										
Stiffness Trend	$k_z > -k_y > k_x > +k_y$					$k_{R_z} > +k_{R_x} > k_{R_y} > -k_{R_x}$				White et al.
	$k_z > k_x > k_y$					$k_{R_y} > k_{R_x} > k_{R_z}$				Costi et al.
	$k_z > k_x > k_y$					$k_{R_y} > k_{R_x} > k_{R_z}$				Present Study

The comparison of the magnitude of the collinear stiffnesses from the positive displacement and the negative displacement may also suggest whether the body is symmetrical about the neutral axis, e.g., asymmetry of lateral stiffness (k_x) between two points mirrored

about the neutral pose (zero displacement) may be explained by asymmetry in spine or muscle stiffnesses. If the slope of the stiffness curve doesn't change over the neutral position, it may indicate the symmetric stiffness of the torso about the body center.

Based on observed "coupling effects" between the degrees-of-freedom shown in the 3-point-pressure validation results, it was logical to further investigate the three-dimensional stiffness characteristics of the torso, which can be represented as a 6x6 stiffness matrix. The stiffness matrix can be experimentally obtained by measuring the forces and moments associated with each of the six orthogonal translations and rotations. For example, once the locations of the pelvic and thoracolumbar rings are selected at a particular level of the human torso, the ROSE can control the displacements of the thoracolumbar ring and measures the resulting forces. The behavior is given by the formula $\mathbf{F} = \mathbf{K}\Delta\mathbf{X}$, where F is a vector of forces and moment applied to the body through the brace ($\mathrm{F} = \left[\mathrm{F_x}, F_y, F_z, T_x, T_y, T_z\right]^T$), ΔX represents a small position and orientation displacement of the ring in Cartesian space ($\Delta\mathbf{X} = [\Delta\mathrm{x}, \Delta\mathrm{y}, \Delta\mathrm{z}, \Delta\phi, \Delta\theta, \Delta\psi]^{\mathrm{T}}$), and **K** is the stiffness matrix to be experimentally determined. By conducting a series of experiments, where known forces **F** are applied and Δ**X** are measured or known Δ**X** are applied and resulting forces are measured, one can estimate the stiffness matrix **K** computationally through a linear regression method (least square fit). Each measurement results in one linear equation relating force to displacement, thus at least 36 different measurements are required to solve for 36 unknown entries of **K**, (5.1).

$$\begin{bmatrix} F_x^{(1)} & \cdots & F_x^{(n)} \\ \vdots & \ddots & \vdots \\ T_z^{(1)} & \cdots & T_z^{(n)} \end{bmatrix} = \begin{bmatrix} k_{11} & \cdots & k_{16} \\ \vdots & \ddots & \vdots \\ k_{61} & \cdots & k_{66} \end{bmatrix} \begin{bmatrix} \Delta x^{(1)} & \cdots & \Delta x^{(n)} \\ \vdots & \ddots & \vdots \\ \Delta\psi^{(1)} & \cdots & \Delta\psi^{(n)} \end{bmatrix} \tag{5.2}$$

where superscript (i) denotes the i^{th} experiment where n ≥ 36. Each experiment has a different magnitude of displacement being applied.

In order to predict the characteristics of the stiffness matrix and to better understand the coupling effects, a simplified torso model was constructed, Figure 5.9(b). It consists of equivalent truss and beam elements, in which the beam element represents the vertebral column posteriorly offset from the center of the torso and the truss element represents the soft tissues. Both elements are fixed at the waist level in all directions while external forces or displacements are applied at the thoracolumbar level. This model is analogous to spine mechanical models developed in other works, Figure 5.9(a) [98, 99, 100, 101].

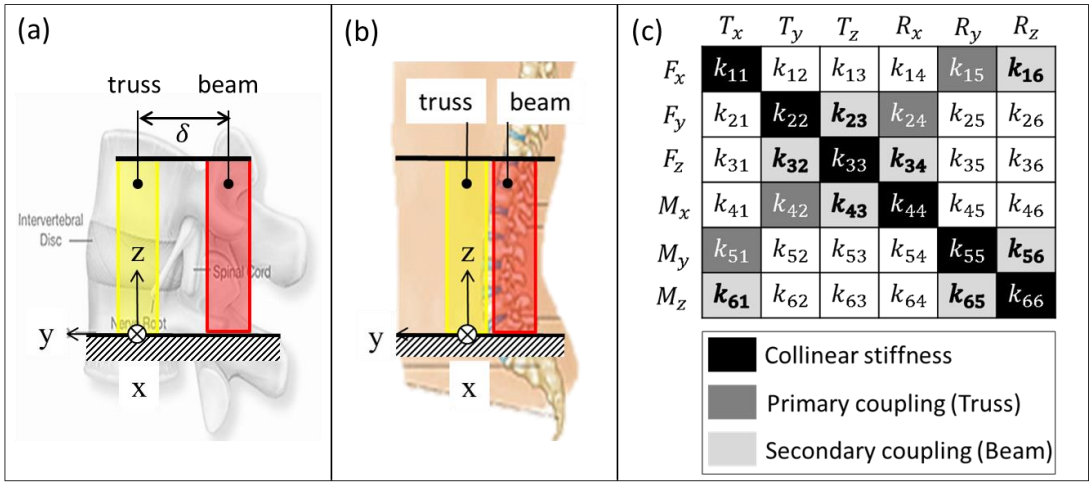

Figure 5.9 (a) spine vertebrae modeled as an equivalent truss/beam structure [99]; (b) human torso model as an equivalent truss/beam structure analogous to (a); and (c) A 6x6 stiffness matrix

Based on this model, the coupling effects can be intuitively explained by the stiffness matrix, as shown in Figure 5.9(c). It captures three dimensional elastic behavior of the human torso, including the collinear elastic behavior and other coupled and uncoupled elastic behaviors. The collinear stiffnesses (diagonal terms) relate forces and moments to the corresponding

collinear displacements (or vice versa). The dark-gray colored, off-diagonal terms are primary coupling stiffnesses, which are induced by the truss element. For example, lateral force (F_x) will cause a translation in the X, which is related to k_{11}, and a rotation about the Y as the spine bends, which is related to k_{15}. The light-gray colored, off-diagonal terms are secondary coupling stiffnesses which are induced by the beam element (spine) that offsets posteriorly from the center of the torso. From the above example, the lateral force (F_x) creates rotation about the Z axis due to the beam effect, and this relationship is defined by k_{16}. The un-shaded elements are more minor couplings which would presumably be much smaller than the rest of stiffness terms.

Using the aforementioned method, 36 independent coefficients were calculated by simultaneously solving 36 sets of linear equation using the *linsolve* function in Matlab (MathWorks, Inc., Natick, MA, USA). Figure 5.10 shows the stiffness matrix computed from a single subject. In a linear elastic conservative system, the stiffness matrix is symmetric on the basis of Maxwell's Reciprocity Theorem. The stiffness matrix of the human torso, however, was not symmetric. This might be partly due to the nonlinear visco-elastic properties of the spine, ligaments and soft tissues, and partly due to the non-isometric properties of human torso. This is in line with recent studies [102, 103] where the experimentally obtained stiffness of the spinal segment was non-symmetric.

	Tx	Ty	Tz	Rx	Ry	Rz
Fx	2735.971	103.859	-123.689	-10.406	-258.074	53.110
Fy	-26.223	2509.828	-296.968	78.334	-22.854	-60.106
Fz	-123.187	-353.219	3895.518	-15.722	94.558	7.766
Mx	-14.501	60.464	11.120	55.054	1.961	3.728
My	-244.783	-12.135	77.004	0.804	80.012	-10.389
Mz	-29.924	-65.695	6.213	-3.852	17.953	43.961

Figure 5.10. Stiffness matrix derived from a single subject.

The stiffness matrix was computed for each subject. The general trends of the stiffness matrix seen across the subjects are: (i) the primary coupling stiffness terms, those induced from the truss effect, were most marked, (ii) the k_{15}/k_{51} pair was generally higher than the k_{24}/k_{42} pair which indicates that the lateral shear force to the lateral rotation motion coupling is higher than the anterior-posterior shear force to the flexion/extension motion coupling, (iii) the secondary coupling stiffness terms, those induced from the beam effect, were less marked than the primary-coupling stiffness terms, and showed inconsistencies in terms of relative magnitudes and signs across the subjects, and (iv) the off-diagonal stiffness terms that were expected to be negligible indeed showed much smaller magnitudes as compared to other terms.

In order to obtain more generalizable results that represent the stiffness matrix of the whole group and to find the general tendency between terms, the stiffness matrices need to be averaged. However, averaging each stiffness term individually will fail to capture the general stiffness characteristics of the torso in terms of relative differences between the terms and

coupling effects for variations in stiffness between subjects were rather high. Therefore, each stiffness matrix needs to be normalized to eliminate inter-subject variability with respect to the magnitude of stiffness before computing an average. Several indices can be taken into consideration in evaluating the stiffness matrix, e.g. determinant, trace norm, and eigenvalues of the matrix. These indices can be used to normalize each element of the stiffness matrix.

However, the elements of the stiffness matrix are not dimensionally uniform; the upper left 3x3 portion represents translational stiffness with the dimension of force/length, the lower right 3x3 portion represents rotational stiffness with the dimension of force multiplied by length, and the remaining portions of the matrix have the dimension of force. Because the stiffness values are dimensionally non-uniform, normalizing the matrix before making it dimensionally uniform is not mathematically valid. A method to derive a dimensionally uniform stiffness matrix has been proposed in [104]. In this study, a similar approach was taken to obtain a dimensionally uniform stiffness matrix. We first obtained the dimensionally uniform force vector **F** and position vector **X**. The first three components of **F** have the dimension of force, whereas the last three components have the dimension of force multiplied by length. On the other hand, the first three components of **X** have the dimension of length, whereas the last three components are dimensionless (radians). In order to make **F** and **X** dimensionally uniform, we define conversion matrix D_F and D_X respectively, which are 6 x 6 diagonal matrices given by

$$\begin{aligned} \mathrm{D_F} &= diag(1,1,1,L^{-1},L^{-1},L^{-1}) \\ \mathrm{D_X} &= diag(1,1,1,L,L,L) \end{aligned} \tag{5.3}$$

When $\mathrm{D_F}$ is pre-multiplied to **F**, and similarly $\mathrm{D_X}$ is pre-multiplied to **X**, we obtain dimensionally uniform force vector $\bar{\mathbf{F}}$ and position vector $\bar{\mathbf{X}}$ as follow:

$$\begin{aligned}\bar{\mathbf{F}} &= \mathrm{D_F}\mathbf{F} \\ \bar{\mathbf{X}} &= \mathrm{D_X}\mathbf{X}\end{aligned} \tag{5.4}$$

by which the dimension of $\bar{\mathbf{F}}$ elements become force and the dimension of $\bar{\mathbf{X}}$ elements become length. Then the formula $\mathbf{F} = \mathrm{K}\Delta\mathbf{X}$ can be converted into $\bar{\mathbf{F}} = \bar{\mathrm{K}}\Delta\bar{\mathbf{X}}$ and the dimensionally uniform stiffness matrix $\bar{\mathbf{K}}$ is obtained, whose elements are all in dimension of force/length. The characteristic length L in the conversion matrix $\mathrm{D_F}$ and $\mathrm{D_X}$ was defined as the maximum radius of the brace calculated from its center to the limb attachment points, so as to capture the physical dimensions of the robot platform. The relation between $\mathbf{F} = \mathrm{K}\Delta\mathbf{X}$ and $\bar{\mathbf{F}} = \bar{\mathrm{K}}\Delta\bar{\mathbf{X}}$ gives us the following conversion between two stiffness matrices, K and $\bar{\mathrm{K}}$.

$$\begin{aligned}\mathrm{K} &= \mathrm{D_F^{-1}}\bar{\mathrm{K}}\mathrm{D_x} \\ \bar{\mathrm{K}} &= \mathrm{D_F}\mathrm{K}\mathrm{D_x^{-1}}\end{aligned} \tag{5.5}$$

Such a conversion offers a convenient way to convert the stiffness matrix from dimensionally non-uniform to dimensionally uniform with simple matrix multiplication. Once the stiffness matrix is converted to a dimensionally uniform stiffness matrix, matrix normalization can be performed. In this study, the trace norm $\hat{k}$ of the matrix was considered, (5.6), which is the square root of the sum of squares of all the elements.

$$\hat{k} = \sqrt{tr(\bar{K}^T\bar{K})} = \sqrt{\sum_{i=1}^{6}\sum_{j=1}^{6} k_{ij}^2} \tag{5.6}$$

Using $\hat{k}$, the normalized dimensionally uniform stiffness matrix $\widehat{\bar{K}}$ was obtained.

$$\widehat{\bar{\mathrm{K}}} = \left[\frac{k_{ij}}{\hat{k}}\right] \ (i,j = 1,\dots,6) \tag{5.7}$$

Then, the normalized stiffness matrix from each subject was averaged over the group. The results are more consistent with the predicted characteristics of a stiffness matrix, where the primary coupling terms were in agreement with the model, Figure 5.9(c), while mixed results were seen in the secondary coupling terms (only k_{23}/k_{32} terms showed consistency). The remaining off-diagonal stiffness terms were comparably smaller, Figure 5.11(a). Once we obtained the group-averaged normalized stiffness matrix, this matrix can be multiplied by the group mean of the trace norm to retrieve the physical meaning of the stiffness matrix, then (5.5) is used to convert it to the dimensionally non uniform stiffness matrix, Figure 5.11(b). This matrix represents the three dimensional stiffness of the torso for our tested group.

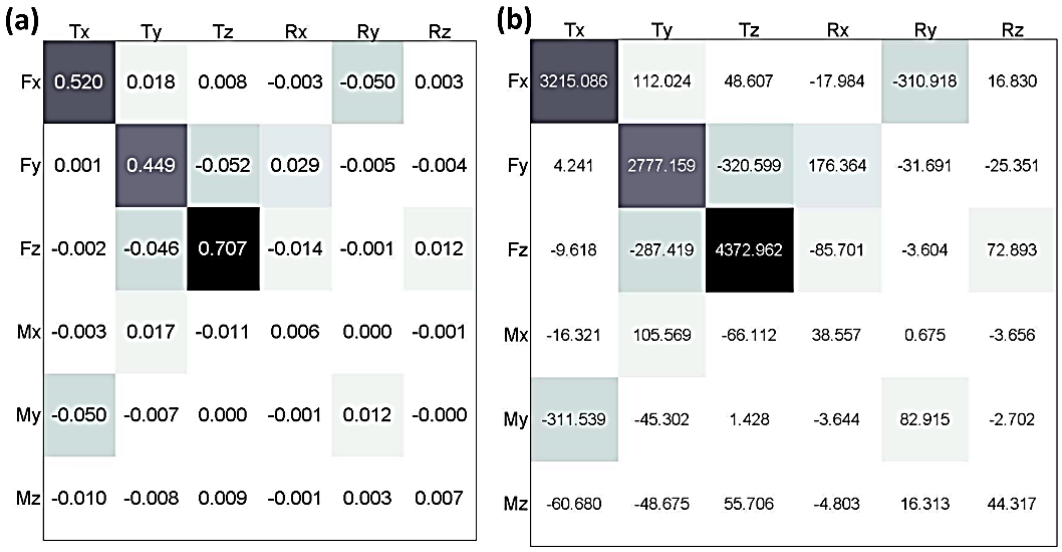

Figure 5.11 (a) Normalized stiffness matrix $\overline{K}_{avg}$ (n=10); (b) stiffness matrix: $K_{avg} = D_F^{-1}\left(\overline{K}_{avg} \times mean(\hat{k})\right)D_X$

5.3.5 Sensitivity and Robustness of Stiffness Measurement

Stiffness variation in sitting and supine position

The collinear stiffness of the human torso measured from the above study were calculated while the subject was in a seated position. Intuitively, the stiffness may vary depending on the pose during which the measurements were taken as the gravitational force directed along the torso would be different, for example between the seated and supine postures. Therefore, we hypothesized that the torso stiffness measured through the brace is pose-dependent. To validate this hypothesis, the same set of force-displacement experiment was repeated while the same subject was in a supine position (T1 in Figure 5.12). In order to avoid the errors from any contact forces other than human torso during force-displacement measurement, only the shoulders and the waist were supported from the ground while the moving part (the mid ring) was not making any contact with the external environment. Then the collinear stiffness were measured and compared with those from the sitting posture (Baseline in Figure 5.12).

The results validate our hypothesis, showing significant differences in five out of six collinear stiffnesses between the two pose configurations, Figure 5.13(a). This result proves that the torso stiffness is indeed pose-dependent. The reductions in k_z and k_ψ from seated to supine posture can be explained by unloading the spine from the gravitational force whereas the differences in other stiffness might be due to changes in the direction of the gravitational force. Changes in other stiffness terms, which increased in the supine posture may be the result of the subject engaging postural muscles to support their body between the contact points at the shoulders and waist.

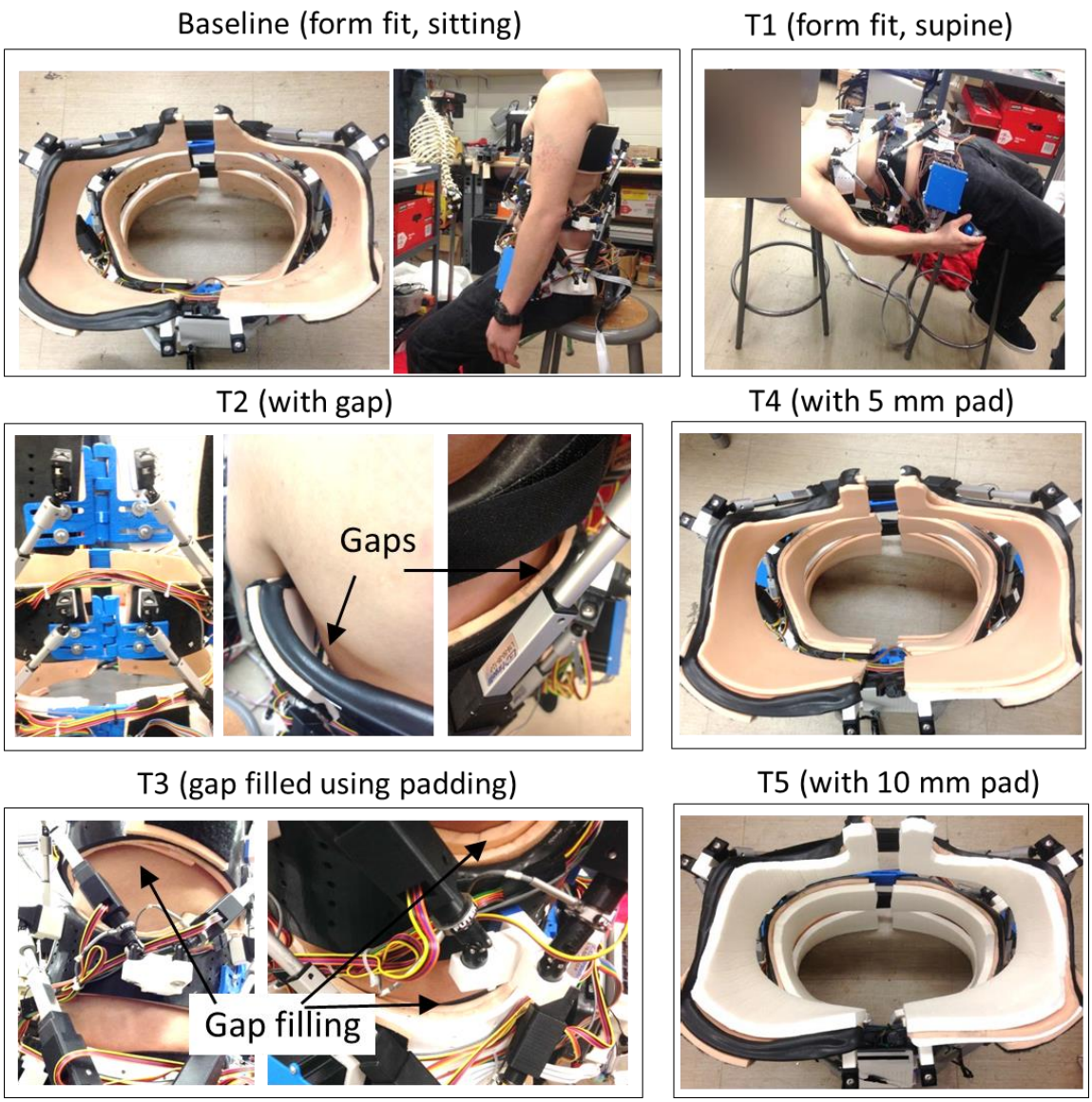

Figure 5.12 Five sessions with different conditions used to test the effects of two poses (sitting-BL and supine-T1), gaps (no gap-BL, with gap-T2, gap filled using padding-T3), and different paddings applied (form fit-BL, with 5 mm padding-T4, and with 10 mm padding-T5) on stiffness measurement

For the following trials, repeated measure ANOVA and pairwise comparisons were used with Bonferroni-Holms correction to detect the statistical significance ($p < 0.05$) of the difference between conditions.

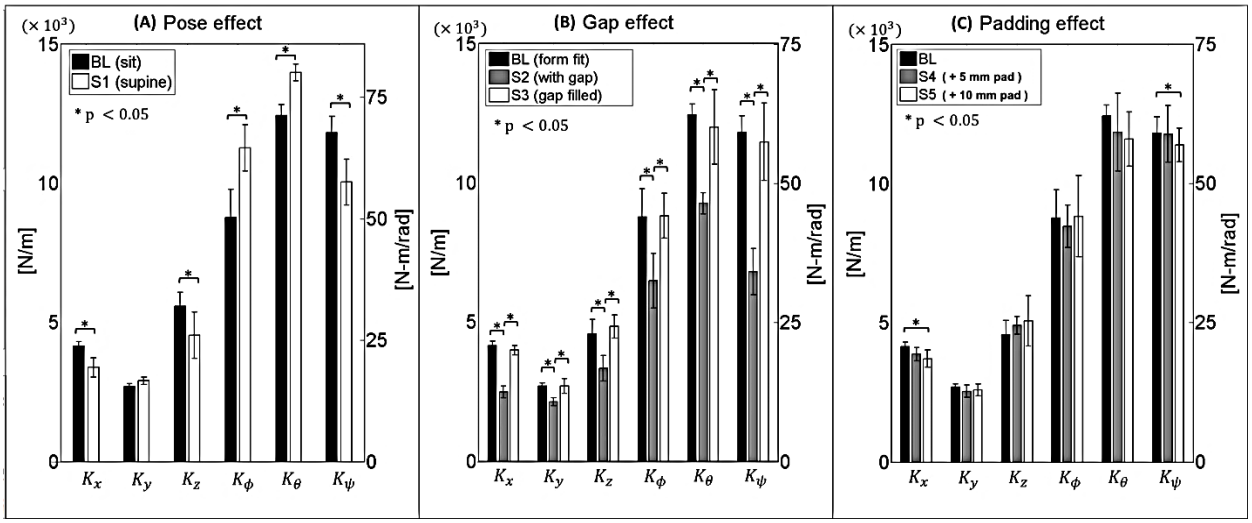

Figure 5.13 (a) Collinear stiffness variation between sitting and supine posture; (b) Collinear stiffness variation due to gaps and gap filling; (c) Collinear stiffness variation due to additional layer of padding added to the brace.

Stiffness variation due to gap

Another factor that may influence the stiffness measurement is fitting. If there is a gap between the brace and the body, it can create an error in the force-displacement measurement. Since the study was intended to measure the torso stiffness of multiple subjects, and because the brace was made to custom fit a single subject, it is expected that the brace may not form fit to other subjects due to the differences in body sizes and curvatures. In fact, small gaps were identified in multiple areas between the brace and the body when it was put onto subjects. These gaps then should be filled with padding to reduce the errors in the measurement. Hence, a second set of experiments was performed to test the following hypothesis: stiffness measurement error increases with the gaps between the brace and the body, and such errors are reduced when the gaps are filled with padding. The same force-displacement measurement was repeated on the same subject: Trial 2 (T2) was when the gaps were imposed by misaligning the rear connecting part of each ring (Figure 5.12), and Trial 3 (T3) was done after filling those gaps with padding

(plastazote®, a padding material commonly used in orthosis). For both sessions, stiffness measurements were taken while the subject was sitting in a comfortable position. The measured stiffness were compared with the baseline values to investigate the effects of gaps and gap filling, Figure 5.13 (b).

The results showed that in T2, the measured stiffness were significantly smaller than BL. This was expected as gaps reduce the contact between the body and the brace, and permit relative motion of the body with respect to the brace, which would result in the reduction in force measurement, and as a result the stiffness values as well. Interestingly, when the gaps were filled with padding (T3), the stiffness values were significantly different than those with gaps (T2), becoming closer to the baseline values. These results indicate that gaps indeed induce errors in stiffness measurements but such errors can be reduced if the gaps are filled with padding. Therefore, it was concluded that (i) the stiffness measurement is sensitive to gaps between the brace and the body, and (ii) errors due to gaps can be reduced with the use of proper padding.

Stiffness variation due to padding

There could be situations where additional layer of padding around the entire brace become necessary to ensure proper fit. Such cases occur when the shape of the torso is very different than the one that the brace was made to fit or if the torso is much smaller than the brace. In such cases, thicker padding would be needed to fill the gaps and ensure proper fit, which could lead to an error in the stiffness measurement as the elastic property of padding could have higher effect on the stiffness measurement. Therefore, we hypothesized that stiffness varies with an additional layer of padding and such variation is proportional to the padding thickness. To test this hypothesis, two conditions were evaluated on the same subject: Trial 4 (T4) was with an

additional 5 mm thick layer of padding added around the brace, and Trial 5 (T5) was with an additional 10 mm thick layer of padding, Figure 5.12. The stiffness measurement procedure used in previous evaluations was repeated in these two conditions and the collinear stiffness terms were calculated and compared with those of the baseline.

The results showed that the stiffness values in T4 didn't show significant difference; however, in T5 two of the stiffness values were significantly different than those of the baseline, Figure 5.13(c). This indicates that the errors from using an additional layer of padding are likely to increase if the padding is thicker than 5 mm. There was also a trend of higher standard deviation in stiffness values as the padding thickness increased. Therefore, it may not be desirable to use the brace on a subject who would need more than 5 mm of additional layer of padding due to poor fit. If we consider the additional layer of padding as soft tissues, this result may also imply that the soft tissue may play a significant role in torso stiffness characteristics

5.4 Discussion

In session 1, the ROSE was shown to allow a majority (more than 70%) of normal range of torso motion while being nearly transparent to the user. Not only does it allow a wide range of torso motion, but it could also control the forces at different postures and during the transition from one posture to another in session 2. This implies that the corrective forces can be applied and controlled to correct the spine without sacrificing the wide range of torso motion. In current static braces, in order to correct lateral curvature of the spine, all degrees-of-freedom of the torso are restrained by a rigid plastic shell. Therefore, the ROSE capable of constraining the curve while allowing a range of torso motions has advantages over the current static design as it can

accommodate different activities of daily living (ADL). Such activities may include bending over to tie one's shoes, sitting, and stretching, etc. In these activities, low stiffness in non-corrective directions is desirable whereas remaining directional stiffness can remain high. Non-rigid braces which use elastic straps, e.g., SpineCor, could also provide larger flexibility to accommodate ADL, however, forces applied at various postures cannot be measured or controlled. Hence, the robotic spine brace differentiates itself from other spine braces, both rigid and non-rigid designs, by being able to accurately measure the torso posture and control the forces to either be nearly transparent to the user or to apply corrections to the spine.

Static spine braces can only provide a fixed configuration to the torso in terms of the magnitude and the direction of correction. Applying varying shapes and thicknesses of padding to the interior side of the brace has been a common practice to change the correction profile. However, this approach heavily relies on the experiences of orthothist and has been practiced without quantitative measurements of its impact on the correction profile. Non-rigid braces could potentially alleviate this limitation through the adjustment of strap placements and strap tensions as needed, but these designs are still limited by the same problem of uncertainty in how the correction is affected by those adjustments. Therefore, the static nature of current braces imposes considerable limitations on the ability of the brace to respond to changes in the human torso and spine over the course of treatment.

By dynamically modulating the corrective actions, either through postural correction or by applying forces, the ROSE can fully address this limitation and potentially increase the adaptability and effectiveness of bracing over the duration of treatment when compared to traditional braces. An additional problem stemming from the uncertainty in the magnitude of the force applied with conventional methods is that it may result in excessive pressure being applied

to underlying skeletal structures, which can cause undesirable bone deformations, typically at the rib cage. The measurement and dynamic modulation of the forces offered by the ROSE can mitigate this issue by ensuring that the forces exerted on the torso are regulated within a safe range.

The 3-point-pressure method for correcting abnormal curves of the spine is a treatment paradigm widely adopted in many static brace designs. It applies translational and rotational displacements at the cross sections of the torso where the curve apices are located. The rationale behind this method is that the spine is a three-dimensional curve, thus correction along only the mediolateral direction may not be sufficient to restore spine alignment. However, the effects of this method have not been quantifiable as it was impossible to measure the forces induced by cross sectional displacements used in this method. The ROSE was able to replicate this method with reasonable consistency across ten subjects while measuring the three dimensional forces exerted on the torso. The applied displacements were controlled at reasonable accuracies for all the subjects, as can be seen by the small standard deviations in all three directional displacements for all tested conditions. On the other hand, the resulting forces do not seem to be consistent across all subjects, a finding evidenced by the higher standard deviation of the forces as compared to that of the applied displacements. This indicates variability in the stiffness of the torso between people. More precisely, the magnitude of the forces resulting from a displacement of a cross section of the torso varies from person to person due to differences in torso stiffness.

Despite such differences, subjects showed similar tendencies in terms of relative magnitude and direction of forces between the applied displacements. More interestingly, even though the planar displacements were applied, there were significant out-of-plane forces exerted on the torso. This was consistently observed across the subjects. It implies that the human torso

presents multi-axis force-displacement coupling effects which are later explained in more detail with a truss-beam-like torso model and by the stiffness matrix. Arguably, the current 3-point-pressure method may not be the most optimal approach as it does not fully address all of the three dimensional elastic behaviors of the human torso. Further investigation is needed to understand if these out-of-plane coupling forces may present any adverse effects on treatment outcome. Since there have never been devices to validate this methodology in terms of the force-displacement relationship, these results are both novel and unique since they address, for the first time, the forces associated with 3-point-pressure. In addition, by replicating the 3-point-pressure method with the ROSE, we validated that the ROSE can provide the same functionality offered by the static braces along with additional controllability and measurement capabilities.

The ability of the robotic spine brace to measure both the posture and forces of one segment with respect to the other segment allows us to investigate the stiffness of the human torso, which has led us to obtain the three dimensional stiffness matrix of the human torso. This is an important finding, as it informs user specific treatment methods according to individual's stiffness characteristics, which can potentially improve the therapeutic outcome of bracing. The stiffness matrix is derived at a specific cross sectional level of the torso (in this study it was the T-10 vertebrae) and the stiffness characteristics may vary at other locations of the torso. For example, the upper thoracic area may be more stiff than the lower thoracic or the lumbar region due to the presence of the rib cage. Also, the stiffness matrix represents only the local stiffness of the measured cross section of the torso. Moreover, the stiffness matrix characterized in this study does not have direct correlation with spine stiffness since stiffness measurements were taken from the surface, not directly from the spine. Therefore, the stiffness matrix captures the combined stiffness of the intermediate tissues and the underlying spine, which cannot be

decoupled through in vivo experiments. Nevertheless, it was shown that the torso stiffness characteristics follow similar patterns to those of the human spine, which suggests that spine stiffness may be the main contributing factor that determines the torso stiffness. It remains possible for the soft tissue to have a larger effect on the torso stiffness, but such a hypothesis cannot be tested easily as it requires independently measuring the stiffness of either the spine or the soft tissue. However, to some extent, this should be possible if experiments are performed in conjunction with radiographic images. The main limitation of this study is that there is no other data in literature to validate results. Previous experimental studies only report the stiffness matrices of the spine segment of human or porcine, often under the axial compressive preload, which makes their results incomparable to our data

Two control modes have been implemented to allow modulation of either the position or the force of the brace. Both control schemes used a quasi-static approach using the kinematic model and the robot's Jacobian where the transient forces induced from brace and limb dynamics were not taken into account. This was based on the assumption that the joint forces required to manipulate the brace and the limbs are much smaller than those required to generate the forces on the torso to displace it. The rationale behind this approach was also based on its application where very low bandwidth is sufficient (less than 1 *Hz*) and the brace segments are light-weight. Hence, dynamic terms that involve mass, velocity, and acceleration of the brace have considerably small effects on the motor forces when it interacts with the human torso. This quasi-static approach also has the advantage of reducing the level of complexity of the controller and reducing the computational cost as it does not necessitate real-time computation of the inverse kinematics and multiplication of the inertia, coriolis, and centripetal matrices of the robotic platform, which are highly non-linear.

It was also assumed that the compliant displacement of the robotic spine brace under external load is significantly lower than that of the human torso such that the forces generated by the motors do not cause compliant deformations of the structure. Based on this assumption, it is expected that the human torso stiffness dictates the stiffness matrix computed from the force-displacement measurement. To further claim this assumption as valid, the brace was designed in a way to minimize changes in geometry under loads through reinforcement of the mechanical connections between the motors and the brace, and rigidizing the buckles and hinges.

5.5 Conclusion

In this chapter, the experimental evaluation of the ROSE was presented which aimed to address the following research question, "what are the three dimensional stiffness characteristics of human torso and their implications for correction of spinal deformity" It was hypothesized that by sensing and actively controlling either the position or the forces of the torso exoskeleton, the research question and limitations in current spine braces can be addressed. The human subject experiment conducted with ten healthy male subjects tested this hypothesis by evaluating the feasible range of torso motion while wearing the ROSE, controlling a constant force at various postures of the torso, applying 3-point-pressure correction, and characterizing three-dimensional stiffness of the torso.

The experimental protocol was described in Section 5.2. The results were presented in Section 5.3 which showed that the ROSE allows the majority of range of torso motion while being nearly transparent to users. ROSE is capable of controlling the forces at various postures of the torso, which implies that it can potentially achieve correction of spinal deformity while allowing mobility. It was also shown that ROSE can apply 3-point-pressure correction while

measuring three-dimensional forces exerted on the torso. Additionally, it can be used in characterizing three dimensional stiffness of the torso. These results indicate that the ROSE can alleviate some of the limitations in current brace treatment for spinal deformities and offers a means to explore new treatment paradigms from characterizing the torso stiffness, which can potentially improve the outcomes of current treatment methods to correct spinal deformities. This was discussed in detail in Section 5.4.

Chapter 6

Conclusion

6.1 Contributions of the current work

This dissertation presented the motivation, prototype design, control algorithms, and experimental evaluations of two types of torso exoskeletons: the Wearable upper Body Suit (WEBS) and the Robotic Spine Exoskeleton (ROSE). Two scientific questions were addressed by conducting human experiments using these exoskeletons: (i) What are the biomechanical and physiological effects of load distribution and dynamic load compensation of a backpack on the human body during load carriage? and (ii) How can we characterize three dimensional stiffness of the human torso for quantifiable assessment and targeted treatment of spinal deformities? The major contributions of this dissertation are summarized in the following sections.

6.1.1 Development of a Wearable upper Body Suit

One of the technological contributions of this work is the development of a novel cable-driven torso exoskeleton, the Wearable upper Body Suit, for assisting backpack load carriage. The load assistive strategies incorporated are: measurement and distribution of the load between the shoulders and the waist, and dynamic load compensation achieved by providing assistive forces synchronized with gait (described in Section 2.2). These strategies have not been realized in

previous backpack load assistive designs. In Chapter 3, the effects of these strategies were experimentally evaluated, showing reductions in gait and postural adaptations, muscle effort, and the metabolic cost of walking with a backpack. The benefits of load distribution and dynamic load compensation can be achieved not only for backpack load carriage but potentially also for cases where significant loads are carried outside the backpack, such as with a tactical vest. By distributing the load between the shoulders and the pelvis, this device also outperforms a framed backpack with a hip belt as it offers a wider range of load distribution between the shoulders and the pelvis (maximum load distribution of a framed backpack with a hip belt is 30%). Additionally, it is comprised of two modules with different functionalities, making it modular and configurable. The technical designs and features of this device incorporate wearability, versatility, and user comfort. In this regard, the components of this suit can be used as sub components of other active exoskeleton designs as well.

6.1.2 Effects of load distribution and dynamic load compensation of a backpack

The WEBS was used to study the effects of load distribution and dynamic load compensation on human biomechanics and energetics. Results from the human experiment revealed several benefits of these strategies: reduction in gait and postural adaptations typically exhibited during load carriage, and reduction in user effort in terms of lower limb muscle activity, muscle fatigue, and metabolic cost. Results also showed that the device can potentially mitigate lower limb musculoskeletal injuries associated with high impact forces by reducing peak normal and peak braking ground reaction forces. These results provide valuable references for future designs of backpack and load assistive devices through unique quantifications of the effects of these load assistive strategies on human biomechanics, gait, and metabolic cost.

6.1.3 Development of a Robotic Spine Exoskeleton

Another technological contribution of this work is the development of a novel Robotic Spine Exoskeleton (ROSE) for quantification and treatment of spinal deformities. The ROSE could overcome the limitations found in current rigid, static, and non-sensorized spine brace designs, by incorporating the following capabilities: (i) allowing a large range of torso motions while being nearly transparent to users, (ii) providing corrective forces at various locations on the torso which can potentially achieve postural corrections while allowing motion to perform ADLs, (iii) quantifying the stiffness characteristics of a cross-section of the torso in different directions for a given pose, (iv) potentially providing user specific correction on the torso based on the individual's torso stiffness characteristics which would optimize therapeutic outcomes of the spine brace treatment. An experimental study was performed with the ROSE on ten healthy male subjects which validated these proposed capabilities of the ROSE (described in Chapter 5).

These capabilities have implications on a number of engineering and clinical questions for future research: (i) Do stiffness characteristics differ between individuals with healthy spine and individuals with spinal deformity? (ii) Could stiffness characteristics be used as markers for early detection of risks for scoliosis in children? (iii) How should the stiffness characteristics of a brace for specific subjects be uniquely determined? (iv) How should the brace be programmed to allow users to perform some necessary activities of daily living, on an as-needed basis, while maintaining the stiffness of the device at other times? (v) How should actuators be placed on the rings to optimize functional measures such as operational workspace, actuator force transmission characteristics, and stiffness over the workspace?

6.1.4 Characterizing the stiffness of human torso

The ROSE was used to study the three dimensional stiffness characteristics of human torso which gives unprecedented insights into its three dimensional elastic behavior. This information could be used in clinical settings to estimate user specific corrective forces for spinal correction, and inform decisions regarding what forces are appropriate to achieve desired postural corrections and address an appropriate course of treatment. This data can also detect asymmetry in torso stiffness. Detection of asymmetry in the stiffness matrix may be beneficial in diagnosis or prognosis of spinal deformities and can potentially improve the clinical outcomes of bracing.

The methodologies used to obtain a dimensionally uniform stiffness matrix and mean stiffness matrix over a group are novel and can be extended to other studies that require similar procedures. This study also validates the testing procedure and analysis methods in studying human torso stiffness, which will serve as a guideline for future clinical studies involving minors with spinal deformities. The ROSE was primarily targeted for studying and treating spinal deformities, but it can be used in other settings, such as providing spinal support for individuals who lack torso control due to neuromuscular diseases or muscle atrophy. It can also be used as a rehabilitation device post spinal surgery or for spinal traction.

6.2 Suggestions for the future work

6.2.1 WEBS and backpack load carriage study

In this work, the Wearable upper Body Suit (WEBS) was designed and its performance for load distribution and dynamic load compensation was evaluated. Although the current design serves

its purpose, there are many aspects of the WEBS that could be improved with future work. The load transmission interface between the backpack and the human body, particularly the waist belt design, could be improved. The current interface concentrates load at the waist belt, specifically under the load bearing columns, which caused discomfort for subjects and hindered their walking abilities. This is an issue that can be addressed by: (i) increasing the contact area around the waist to improve pressure distribution, (ii) stiffening the external side of the waist belt around the load bearing column interface to reduce load concentration, (iii) improving padding materials on the internal side of the belt to prevent peak pressure points and to promote user comfort. Design optimizations on other structural components (shoulder supports, load bearing columns, etc.) could be also considered to improve the compatibility of the device with conventional backpacks or military gear (e.g., military tactical vest or rifles), which would increase its practicality.

Results from the human subject experiments confirmed that load distribution and dynamic load compensation produce positive results by reducing body compensations under loaded walking and provide some metabolic benefits. However, these results come from a single load distribution configuration (50%) and a single load condition (25% body weight backpack). This load distribution might not be optimal choice and could be further studied. A 50% load distribution was chosen in this study as values exceeding this, i.e., more load is carried by the pelvis than the shoulders, seemed to cause excessive local pressures on pelvis and hip areas where the belt made contact. Hence, once the design improvements are made on the waist belt to reduce local pressure and improve user comfort and wearability, load distributions higher than 50 % could be tested. Then, answers to three research questions could be sought: (i) How do different load distribution strategies provided by the device affect the biomechanical and physiological performance of the wearer as he walks with a backpack? (ii) Is there an optimal

load distribution strategy maximizing beneficial outcome measures? (iii) Should the optimal load distribution strategy vary according to the magnitude of the applied load? To address these questions, human responses in loaded walking, in terms of kinematics, ground reaction forces, metabolic costs, and muscle activations could be studied by conducting a similar human subject study as presented in this work, with different load distribution schemes and different magnitudes of load.

In this study, we explored the effects of actively compensating for dynamic loads; however, pack load remained the same throughout these sessions. However, the hardware required to achieve this strategy adds additional mass to the backpack load. For the system to be advantageous in a real world situation the metabolic gains from dynamic load compensation must offset the penalty caused by carrying the added mass of the system and this still needs to be validated. Nevertheless, the mass of the active module attached to the backpack takes up only 12 to 14% of total applied load (i.e., 2 to 3% BW among 25% BW load); hence, it is anticipated that the metabolic benefits seen with dynamic load compensation would be moderate yet still present.

Additionally, if the device can compensate for the upward dynamic loads in addition to the downward dynamic loads, it could further improve the findings of the study. Despite the small sample size, significant changes in biomechanical, physiological and subjective parameters were detected. Therefore, it is expected that some of the parameters which only demonstrated trends rather than statistical significance could be confirmed if they were validated with prolonged load carriage with heavier loads and a larger sample size. It is anticipated that with heavier backpack loads and prolonged carriage duration, the advantages of using the device would be more pronounced. While not addressed in this study, further studies should be able to answer these questions.

6.2.2 Robotic Spine Exoskeleton

While the current design of the ROSE is well-suited to research purposes, it is not necessarily intended to replace traditional bracing in its current role. It would be more suited to be used as a testing tool for identifying torso stiffness characteristics of patients, or as an in-home therapy device to provide assistance in self-correction exercises or novel treatment paradigm (e.g., dynamic force correction). One reason is that the weight of the system (weighing close to 4kg) is heavier and bulkier than a simple plastic shell, which may not be favorable for daily use. In addition, the brace has a total of twelve active degrees of freedom. While these degrees of freedom allow users to maintain the majority of their natural range of torso motion and are required to investigate the three dimensional stiffness characteristics of the human torso, their incorporation greatly increases the bulkiness and the weight due to the necessity of twelve actuators, twelve load cells, and associated electronics. Therefore, its practicality could potentially be increased by reducing the number of motors and thus the active degrees of freedom through incorporating a cable driven mechanism or compliant elements.

Further studies using the ROSE needs to be done on individuals with spinal deformities to address the following research questions: (i) How their stiffness characteristics differ from those of healthy individuals, (ii) How to modulate the brace on an individual basis to attain desired corrective forces in some directions and mobility in others, and (iii) How different control strategies, such as dynamic modulation of corrective forces, affect treatment outcomes as compared to those of traditional bracing techniques. To evaluate treatment outcomes in the correction of spinal deformities, radiography could be used in conjunction with the correction provided by the ROSE, to capture whether the correction on the torso has been transferred to the

spine, and to measure the position and forces of the ROSE at which the spine alignment was achieved.

There are several design improvements that could be considered in the future. Compliance with bracing regimens continues to be a hurdle as many individuals do not comply with the prescribed 12-16 hours of wear per day. The current design of the ROSE is not as low profile as traditional braces, which are made out of sheets of thermo-molded plastic. This was unavoidable due to addition of actuators, sensors, and electronics. The electronics could be made compact and light-weight by replacing the current custom made perf boards with PCBs, but many other components cannot be made smaller or lighter. While a bulkier brace seems to be more visible and therefore less likely to be adopted, it is hoped that through appropriate control strategies the time the brace needs to be worn can be reduced without negatively impacting outcomes. If a wearer can receive the same treatment outcomes while only wearing the brace at home, rather than wearing conventional braces for a majority of the day, then compliance may increase and individuals may be more likely to benefit from bracing.

Additionally, most of the plastic parts of the ROSE are currently 3D printed using ABS material, which is too brittle for day-to-day wear. One of the next steps will be adapt designs to sheet formed polyethylene in line with current fabrication techniques. Finally, the device could be made more comfortable by placing force sensing resistors around the inner surface of the brace to measure the interaction forces between the device and the body during operation. This could help prevent excessive local pressure being applied to the body from the device via real time monitoring of pressure data.

Bibliography

[1] "Anatomy and Function: A Patient's Guide to Anatomy and Function of the Spine," University of Maryland Medical Center, [Online]. Available: http://umm.edu/programs/spine/health/guides/anatomy-and-function. [Accessed 25 3 2016].

[2] J. Johnson, "Functions of the Spine," Back Pain Expert, [Online]. Available: http://www.backpainexpert.co.uk/functionsofthespine.html. [Accessed 25 3 2016].

[3] "The Structure and Function of a Healthy Spine," Cleveland Clinic, [Online]. Available: http://my.clevelandclinic.org/health/diseases_conditions/hic-the-structure-and-function-of-a-healthy-spine. [Accessed 22 3 2016].

[4] A. White and M. M. Panjabi, Clinical Biomechanics of the Spine, 2nd ed., J.B. Lippincott Company, 1990.

[5] S. Eldelson, "Spinal Column: An Integral Part of the Human Body," Spine Universe, [Online]. Available: http://www.spineuniverse.com/anatomy/spinal-column-integral-part-human-body. [Accessed 20 3 2016].

[6] Y. Hong, J. Li and D. Fong, "Effect of prolonged walking with backpack loads on trunk muscle activity and fatigue in children," *Electromyography and Kinesiology*, vol. 18, no. 6, pp. 990-996, 2008.

[7] F. Trevelyan and S. Legg, "Back pain in school children: where to from here?," *Applied Ergonomics*, vol. 37, no. 1, pp. 45-54, 2006.

[8] W. Mackenzie, J. Sampath, R. Kruse and G. Sheir-Neiss, "Backpacks in children," *Clinical orthopedics and related research*, vol. 409, pp. 78-84, 2003.

[9] Y. Hong and C. Cheung, "Gait and posture responses to backpack load during level walking in children," *Gait and Posture*, vol. 17, no. 1, pp. 28-33, 2003.

[10] J. Bachkosky, M. Andrews, R. Douglass, J. Feigley, L. Felton, P. Fernandez and A. Fratarangelo, "Lightening the Load," US Naval Research Advisory Committee, 12, 2007.

[11] U. C. P. S. Commission, "National Electronic Injury Surveillance System (NEISS)," 2014.

[12] J. Knapik, E. Harman and K. Reynolds, "Load carriage using packs: A review of physiological, biomechanical and medical aspects," *Applied Ergonomics*, vol. 27, no. 3, pp. 207-216, 1996.

[13] J. Knapik, K. Reynolds and E. Harman, "Soldier load carriage: historical, physiological, biomechanical, and medical aspects," *Military medicine*, vol. 169, no. 1, pp. 45-56, 2004.

[14] K. Reynolds, "Prolonged treadmill load carriage: acute injuries and changes in foot anthropometry," DTIC document, 1990.

[15] E. Harman, K. Han, P. Frykman, M. Johnson, F. Russell and M. Rosenstein, "The effects on gait timing, kinetics, and muscle activity of various loads carried on back," *Medicine and Science in Sports and Exercise,* vol. 24, no. 5, p. S129, 1992.

[16] S. Birrell, R. Hooper and R. Haslam, "The effect of military load carriage on ground reaction forces," *Gait & Posture,* vol. 26, no. 4, pp. 611-614, 2007.

[17] H. Kinoshita, "Effects of different loads and carrying systems on selected biomechanical parameters describing walking gait," *Ergonomics,* vol. 28, no. 9, pp. 1347-1362, 1985.

[18] R. Attwells, S. Birrell, R. Hooper and N. Mansfield, "Influence of carrying heavy loads on soldier's posture movement and gait," *Ergonomics,* vol. 49, no. 14, pp. 1527-1537, 2006.

[19] P. Quesada, L. Mengelkoch, R. Hale and S. Simon, "Biomechanical and metabolic effects of varying backpack loading on simulated marching," *Ergonomics,* vol. 43, no. 3, pp. 293-309, 2000.

[20] G. Bastien, P. Williams, B. Schepens and N. Heglund, "Effect of load and speed on the energetic cost of human walking," *European Journal of Applied Physiology,* vol. 94, no. 1-2, pp. 76-83, 2005.

[21] M. Holewjin, "Physiological strain due to load carrying," *European journal of applied physiology and occupational physiology,* vol. 61, no. 3, pp. 237-245, 1990.

[22] G. Ghori and R. Luckwill, "Responses of the lower limb to load carrying in walking man," *European Journal of Applied Physiology and Occupational Physiology,* vol. 54, no. 2, pp. 145-150, 1985.

[23] J. Bobet and R. Norman, "Effects of load placement on back muscle activity in load carriage," *European Journal of Applied Physiology and Occupational Physiology,* vol. 53, no. 1, pp. 71-75, 1984.

[24] T. Cook and D. Neumann, "The effects of load placement on the EMG activity of the low back muscles during load carrying by men and women," *Ergonomics,* vol. 30, pp. 1413-1423, 1987.

[25] K. Simpson, B. Munro and J. Steele, "Backpack load affects lower limb muscle activity patterns of female hikers during prolonged load carriage," *Journal of Electromyography and Kinesiology,* vol. 21, no. 5, pp. 782-788, 2011.

[26] Y. Al-Khabbaz, T. Shimada and M. Hasegawa, "The effect of backpack heaviness on trunk-lower extremity muscle activities and trunk posture," *Gait & Posture,* vol. 28, no. 2, pp. 297-302, 2008.

[27] P. Martin and R. Nelson, "The effect of carried loads on the walking patterns of men and women," *Ergonomics,* vol. 29, no. 10, pp. 1191-1202, 1986.

[28] D. Tilbury-Davis and R. Hooper, "The kinetic and kinematic effects of increasing load carriage upon the lower limb," *Human Movement Science,* vol. 18, no. 5, pp. 693-700, 1999.

[29] S. Birrell and R. Haslam, "The effect of military load carriage on 3-D lower limb kinematics and spatiotemporal parameters," *Ergonomics,* vol. 52, no. 10, pp. 1298-1304, 2009.

[30] K. Simpson, B. Munro and J. Steele, "Effects of prolonged load carriage on ground reaction forces, lower limb kinematics and spatio-temporal parameters in female recreational hikers," *Ergonomics,* vol. 55, no. 3, pp. 316-326, 2012.

[31] S. Birrell and R. Haslam, "The effect of load distribution within military load carriage systems on the kinetics of human gait," *Applied Ergonomics,* vol. 41, no. 4, pp. 585-590, 2010.

[32] R. Alexandar, "Energy-saving mechanisms in walking and running," *Journal of Experimental Biology,* vol. 160, pp. 55-69, 1991.

[33] G. Cavagna, N. Heglund and C. Taylor, "Mechanical work in terrestrial locomotion: two basic mechanisms for minimizing energy expenditure," *American Journal of Physiology,* vol. 233, no. 5, pp. R243-261, 1977.

[34] D. Winter, The biomechanics and motor control of human gait: normal, elderly and pathological, University of Waterloo Press, 1991.

[35] C. Devroey, I. Jonkers, A. d. Becker, G. Lenaerts and A. Spaepen, "Evaluation of the effect of backpack load and position during standing and walking using biomechanical, physiological and subjective measures," *Ergonomics,* vol. 50, no. 5, pp. 728-742, 2007.

[36] L. Ren, R. Jones and D. Howard, "Dynamic analysis of load carriage biomechanics during level walking," *Journal of Biomechanics,* vol. 38, no. 4, pp. 853-863, 2005.

[37] M. Foissac, G. Millet, A. Geyssant, P. Freychat and A. Belli, "Characterization of the mechanical properties of backpacks and their influence on the energetics of walking," *Journal of Biomechanics,* vol. 42, no. 2, pp. 125-130, 2009.

[38] L. Rome, L. Flynn and T. Yoo, "Rubber bands reduce the cost of carrying loads," *Nature,* vol. 444, pp. 1023-1024, 2006.

[39] J. Ortega and C. Farley, "Minimizing center of mass vertical movement increases metaboli cost in walking," *Journal of applied physiology,* vol. 99, pp. 2066-2017, 2005.

[40] F. Z. S. K. R. Neptune, "Muscle mechanical work requirements during normal walking: the energetic cost of raising the body's center-of-mass is significant," *Journal of Biomechanics,* vol. 37, pp. 817-825, 2004.

[41] R. Lloyd, "The oxygen consumption associated with unloaded walking and load carriage using two different backpack designs," *European Journal of Applied Physiology,* vol. 81, pp. 486-492, 2000.

[42] E. Harman, P. Frykman, J. Knapik and K. Han, "785 backpack vs. front-back pack: Differential effects of load on walking posture," *Medicine & Science in Sports & Exercise,* vol. 26, no. 5, p. S140, 1994.

[43] S. Legg and A. Mahanty, "Comparison of five modes of carrying a load close to the trunk," *Ergonomics,* vol. 28, no. 12, pp. 1653-1660, 1985.

[44] R. Johnson, J. Knapik and D. Merullo, "Symptoms during load carrying: effects of mass and load distribution during a 20-km road march," *Perceptual and Motor Skills,* vol. 82, no. 1, pp. 331-338, 1995.

[45] J. Tierney, J. Gillespie Jr., R. Stratton, M. Glenn, J. Tzeng and M. Maher, "Design and Optimization of an Exospine Structure Utilizing Lightweight Composites," in *SAMPE 2012*, Baltimore, MD, 2012.

[46] J. Gardner, L. Holmes Jr and J. Tzeng, "Fabrication of a First Article Lightweight Composite Technology Demonstrator - Exospine," Army Research Laoratory, 2014.

[47] A. Zoss, H. Kazerooni and A. Chu, "Biomechanical Design of the Berkeley Lower Extermity Exoskeleton (BLEEX)," *IEEE/ASME Transactions on Mechatronics,* vol. 11, no. 2, pp. 128-138, 2006.

[48] Spine-health, "Spine Deformities Health Center," Spine-health, [Online]. Available: http://www.spine-health.com/conditions/spinal-deformities. [Accessed 25 03 2016].

[49] "National Scoliosis Foundation," [Online]. Available: www.scoliosis.org. [Accessed 15 2 2016].

[50] S. Weinstein, L. Dolan, J. C. Cheng, A. Danielsson and J. A. Morcuende, "Adolescent idiopathic scoliosis," *Lancet,* vol. 371, pp. 1527-1537, 2008.

[51] J. Cobb, "Outline for the study of scoliosis," *The American Academy of Orthopedic Surgeons Instructional Course Lectures,* vol. 5, 1948.

[52] S. Weinstein and I. Ponseti, "Curve progression in idiopathic scoliosis," *Journal of Bone Joint Surgery,* vol. 65, pp. 447-455, 1983.

[53] J. Sevastik and I. Stokes, "Idiopathic scoliosis: Terminology," *Spine: State of the Art Reviews,* vol. 14, pp. 299-303, 2000.

[54] J. Sanders, J. Khoury and S. Kishan, "Predicting scoliosis progression from skeletal maturity: a simplified classification during adolescence," *Journal of Bone Joint Surgery,* vol. 90, pp. 540-553, 2008.

[55] J. Sanders, R. Browne, S. McConnell, S. Margraf, T. Cooney and D. Finegold, "Maturity assessment and curvee progression in girls with idiopathic scoliosis," *Journal of Bone Surgery,* vol. 89, pp. 64-73, 2007.

[56] A. Nachemson and L. Peterson, "Effectiveness of treatment with a brace in girls who have adolescent idiopathic scoliosis," *Journal of Bone Joint Surgery,* vol. 77, pp. 815-822, 1995.

[57] C. Nnadi and J. Fairback, "Scoliosis: a review," *Pediatrics and Child Health,* vol. 20, no. 5, pp. 215-220, 2009.

[58] J. Carlson, "Clinical Biomechanics of Orthotic Treatment of Idiopathic Scoliosis," *Journal of Prosthetics and Orthotics,* vol. 15, no. 4S, p. 17, 2003.

[59] R. Heary, C. Bono and S. Kumar, "Bracing for scoliosis," *Neurosurgery,* vol. 63, pp. A125-A130, 2008.

[60] S. Negrini and S. Minozzi, Braces for idiopathic scoliosis in adolescents, New York, NY: John Wiley & Sons, 2010.

[61] S. Weinstein, L. Dolan, J. Wright and M. Dobbs, "Effects of bracing in adolescents with idiopathic scoliosis," *New England Journal of Medicine,* vol. 369, no. 16, pp. 1512-1521, 2013.

[62] J. Wynne, "The boston brace system philosophy, biomechanics, design & fit," *Studies in health technology and informatics,* vol. 135, pp. 370-384, 2007.

[63] M.Rigo and H. Weiss, "The cheneau concept of bracing - biomechanical aspects," *Studies in Health Technology and Informatics,* vol. 135, pp. 303-319, 2008.

[64] C. Price, D. Scott, F. Reed and M. Riddick, "Night-time bracing for adolescent idiopathic scoliosis with the charleston bending brace: preliminary report," *Spine,* vol. 15, no. 12, pp. 1294-1299, 1990.

[65] J. Lonstein and R. Winter, "Milwaukee brace for the treatment of adolescent idiopathic scoliosis: a review of one thousand and twenty patients," *Journal of Bone Joint Surgery,* vol. 76, pp. 1207-1221, 1994.

[66] W. Blount, "The milwaukee brace in the treatment of the young child with scoliosis," *Archives of Orthopaedic and Trauma Surgery,* vol. 56, no. 4, pp. 363-369, 1964.

[67] D. Federico and T. Renshaw, "Results of treatment of idiopathic scoliosis with the Charleston bending orthosis," *Spine,* vol. 15, pp. 886-887, 1990.

[68] J. Bowen, K. Keeler and S. Pelegie, "Adolescent idiopathic scoliosis managed by a nighttime bending brace," *Orthopaedics,* vol. 24, no. 10, pp. 967-970, 2001.

[69] G. R. N. B. T. Brivas, "Night-time braces for Adolescent Idiopathic Scoliosis," *Disability and Rehabilitation: Assistive Technology,* vol. 3, no. 3, pp. 120-129, 2008.

[70] H. Watts, J. Hall and W. Stanish, "The Boston brace system for the treatment of low thoracic and lumbar scoliosis by the use of girdle without superstructure," *Clinical Orthopaedics,* vol. 126, pp. 87-92, 1977.

[71] H. Labelle, J. Dansereau, C. Bellefleur and B. Poitras, "Three-dimensional effect of the Boston brace on the thoracic spine and rib cage," *Spine,* vol. 21, no. 1, pp. 59-64, 1996.

[72] H. Weiss and M. Rigo, "The Cheneau concept of Bracing - Actual Standards," *Studies in Health Technology and Informatics,* vol. 135, pp. 291-302, 2008.

[73] M. Rigo and H. Weiss, "The cheneau concept of bracing - biomechanical aspects," *Studies in Health Technology and Informatics,* vol. 135, pp. 303-319, 2008.

[74] J. Valavanis, A. Bountis, C. Zacharious, D. Kokkonis, D. Anagnostou, D. Giahos and E. Daskalakis, "Three-Dimensional Brace Treatment for Idiopathic Scoliosis," in *Three dimensional analysis of spinal deformities*, IOS press, 1995, pp. 337-341.

[75] T. B. Grivas, A. Bountis, A. Vrasami and N. V. Bardakos, "Brace technology thematic series: the dynamic derotation brace," *Scoliosis,* vol. 5, no. 20, pp. 1-13, 2010.

[76] N. Nakamura, M. Uesugi, Y. Inaba, J. Machida, S. Okuzumi and T. Saito, "Use of dynamic spinal brace in the management of neuromuscular scoliosis: a preliminary report," *Journal of Pediatric Orthospaedics,* vol. 23, no. 3, pp. 291-298, 2014.

[77] R. J. Triolo, R. Kobetic and R. Quinn, "A hybrid neuroprosthesis for walking with SCI," Advanced Platform Technology Center, [Online]. Available: http://www.aptcenter.research.va.gov/A_Hybrid_Neuroprosthesis.asp. [Accessed 18 2 2015].

[78] "ExMS-1," ExoDynamics,LLC, [Online]. Available: www.exodynamicsmedical.com. [Accessed 20 4 2016].

[79] C. Coillard, V. Vachon, A. Circo, M. Beausejour and C. Rivard, "Effectiveness of the spinecor brace based on the new standardized criteria proposed by the scoliosis research society for adolescent idiopathic scoliosis," *Journal of Pediatric Orthopaedics,* vol. 27, no. 4, pp. 375-379, 2007.

[80] M. Wong, J. Cheng, T. Lam, B. NG, S. Sin, S. Lee-Shum, D. Chow and S. Tam, "The effect of rigid versus flexible spinal orthosis on the clinical efficacy and acceptance for the patients with adolescent idiopathic scoliosis," *Spine,* vol. 33, no. 12, pp. 1360-1365, 2008.

[81] C. Rivard, "Letters,," *Spine,* vol. 33, no. 25, p. 2837, 2008.

[82] J. Mac-Thiong, Y. Petit, C. Aubin, S. Delorme, J. Dansereau and H. Labelle, "Biomechanical evaluation of the boston brace system for the treatment of adolescent idiopathic scoliosis: relationship between strap tension and brace interface foces," *Spine,* vol. 29, no. 1, pp. 26-32, 2004.

[83] C. Aubin, H. Labelle, A. Ruszkowsk, Y. Petit, D. Gignac, J. Joncas and J. Dansereau, "Variability of strap tension in brace treatment for adolescent idiopathic scoliosis," *Spine,* vol. 24, no. 4, pp. 349-354, 1999.

[84] E. Lou, S. Venkateswaran, D. Hill, J. Raso and A. Donauer, "An intelligent active brace system for the treatment of scoliosis," *Instrumentation and Measurement, IEEE Transactions on,* vol. 53, no. 4, pp. 1146-1151, 2004.

[85] T. B. Grivas, "European Braces for Conservative Scoliosis Treatment," in *Human musculoskeletal biomechanics*, Intech, 2012, pp. 30-48.

[86] V. Vashista, S. Mustafa and S. Agrawal, "Experimental studies on the human gait using a tethered pelvic assist device (t-pad)," in *In Rehabilitation Robotics (ICORR), 2011 IEEE International Conference on*, 2011.

[87] G. Allison and T. Fujiwara, "The relationship between EMG median frequency and low frequency band amplitude changes at different levels of muscle capacity," *Clinical Biomechanics,* vol. 17, no. 6, pp. 464-469, 2002.

[88] A. Mannion and P. Dolan, "Relationship between myoelectric and mechanical manifestations of fatigue in the quadriceps femoris muscle group," *European Journal of Applied Physiology,* vol. 74, no. 5, pp. 411-419, 1996.

[89] E. Harman, K. Han, P. Frykman and C. Pandorf, "The effects of backpack weight on the biomechanics of load carriage," U.S. Army Research Institute of Environmental Medicine, 2000.

[90] A. Polcyn, C. Bensel, E. Harman, J. Obusek, C. Pandorf and P. Frykman, "Effects of Weight Carried by Soldiers: Combined Analysis of Four Studies on Maximal Performance, Physiology, and Biomechanics," US Army Research Institute of Environmental Medicine, Natick, MA, 2002.

[91] D. Bloom and A. Woodhull-McNeal, "Postural adjustments while standing with two types of loaded backpack," *Ergonomics*, vol. 30, no. 10, pp. 1425-1430, 1987.

[92] A. G. Patwardhan, R. M. Havey, K. P. Meade, B. Lee and B. Dunlap, "A Follower Load Increases the Load-Carrying Capacity of the Lumbar Spine in Compression," *Spine,* vol. 24, no. 10, pp. 1003-1009, 1999.

[93] J. Hoover and S. Meguid, "Performance assessment of the suspended-load backpack," *Int J. Mech Mater Des*, vol. 7, pp. 111-121, 2011.

[94] M. Lafiandra and E. Harman, "The distribution of forces between the upper and lower back during load carriage," *Medicine and Science in Sports and Exercise,* vol. 36, no. 3, pp. 460-467, 2004.

[95] A. Grabowski, C. Farley and R. Kram, "Independent metabolic costs of supporting body weight and accelerating body mass during walking," *Journal of Applied Physiology,* vol. 98, no. 2, pp. 579-583, 2005.

[96] H. J. Wilke, P. Neef and M. Caimi, "New in vivo measurements of pressures in the intervertebral disc in daily life," *Spine,* vol. 24, pp. 755-762, 1999.

[97] J. Costi, I. Stokes, M. Gardner-Morse and J. C. Latridis, "Frequency-dependent behavior of the intervertebral disc in response to each of six degree of freedom dynamic loading," *Spine,* vol. 33, no. 16, pp. 1731-1738, 2008.

[98] M. Gardner-Morse and I. Stokes, "Physiological axial compressive preloads increase motion segment stiffness, linearity and hysteresis in all six degrees of freedom for small displacements about the neutral pose," *Journal of Orthopaedic Research,* vol. 21, pp. 547-552, 2003.

[99] M. Gardner-Morse and I. Stokes, "Structural behavior of human lumbar spinal motion segments," *Journal of Biomechanics,* vol. 37, pp. 205-212, 2004.

[100] M. Panjabi, R. Brand and A.A.White, "Three-dimensional flexibility and stiffness properties of the human thoracic spine," *Journal of Biomechanics,* vol. 9, pp. 185-192, 1976.

[101] V.K.Goel, "Three-dimensional motion behavior of the human spine-a question of terminology," *ASME Journal of Biomechanical Engineering*, vol. 109, pp. 353-355, 1987.

[102] T. Holsgrove, S. Ghedduzzi, H. S. Gill and A. W. Miles, "The development of a dynamic, six-axis spine simulator," *Spine,* vol. 14, pp. 1308-1317, 2014.

[103] T. Holsgrove, H. Gill, A. W. Miles and S. Gheduzzi, "The dynamic, six-axis stiffness matrix testing of porcine spinal specimens," *Spine,* vol. 15, pp. 146-184, 2015.

[104] F. Tahmasebi and L.-W. Tsai, "On the stiffness of a novel six degree-of-freedom parallel minimanipulator," *Journal of Robotics System*, vol. 12, no. 12, pp. 845-856, 1995.

[105] J. Merlet, "Direct kinematics of parallel manipulators," *IEEE Transactions on Robotics and Automation*, vol. 9, no. 6, pp. 842-845, 1993.

[106] Taghirad, Parallel robots, New York, NY: Taylor & Francis Group, 2012.

[107] K. Waldron and K. Hunt, "Series-parallel dualities in actively coordinated mechanisms," *The International Journal of Robotics Research ,* vol. 10, no. 5, pp. 473-480, 1991.

[108] C. Gosselin, "Stiffness mapping of parallel manipulators," *IEEE Transactions on Robotics and Automation,* vol. 6, pp. 377-382, 1990.

[109] L. Biagiotti and C. Melchiorri, Trajectory planning for automatic machines and robots, Springer, 2008.

[110] W. Edwards, W. Hayes, I. Posner, A. White and R. Mann, "Variation of lumbar spine stiffness with load," *Journal of Biomechanical Engineering,* vol. 109, pp. 35-42, 1987.

[111] V. Goel, "Three-dimensional motion behavior of the human spine - a question of terminology," *ASME Journal of Biomechanical Engineering*, vol. 109, pp. 353-355, 1987.

[112] M. Panjabi, K. Abumi, J. Duranceau and T. Oxland, "Spinal stability and inter-segmental muscle forces: biomechanical model," *Spine,* vol. 14, pp. 194-200, 1989.

[113] J. Janevic, J. A. Ashton-Miller and A. B. Shultz, "Large compressive preloads decrease lumbar motion segment flexibility," *Journal of Orthopaedic Research,* vol. 9, no. 2, pp. 228-236, 1991.

[114] I. Stokes, M. Gardneer-Morse, D. Churchill and J. Laible, "Measurement of a spinal motion segment stiffness matrix," *Journal of Biomechanics,* vol. 35, pp. 517-521, 2002.

[115] M. Gardner-Morse and I. Stokes, "Physiological axial compressive preloads increase motion segment stiffness, linearity and hysteresis in all six degrees of freedom for small displacements about the neutral pose," *Journal of Orthopaedic Research,* vol. 21, pp. 547-552, 2003.

[116] A. Race, N. D. Broom and P. Roberson, "Effect of loading rate and hydration on the mechanical properties of the disc," *Spine,* vol. 25, no. 6, pp. 662-669, 2000.

[117] M. Gardner-Morse and I. A. Stokes, "Structural behavior of human lumbar spinal motion segments," *Journal of Biomechanics,* vol. 37, pp. 205-212, 2004.

[118] O. O'Reilly, M. Metzger, J. Buckley, D. Moody and J. Lotz, "On the stiffness matrix of the intervertebral joint: application to total disk replacement," *Journal of Biomechanical Engineering,* vol. 131, pp. 081007-1-9, 2009.

Appendix

Appendix A. The Second Spine

The Second Spine was designed to provide an alternate load pathway to transfer the backpack load from the shoulders to the waist in addition to the human spine. The aim of this design was to relieve stress on the spine and torso thereby potentially mitigating back and shoulder injuries. The secondary load pathway forms in parallel with the spine by three load bearing columns that connects shoulder pads to a waist belt, Figure A.1. Two configurations of the device are utilized, device "On" and "Off", to provide either structural stiffness to transfer the load from the shoulders to the waist, or flexibility to allow user to maintain a normal range of torso motion. This was accomplished through designing the load bearing columns with cone-shaped segments connected in series, Figure A.2. The distance between the adjoining segments is modulated by the tension of a cable that routes through them. In device "Off" configuration, the cable is not under tension and the springs interposed in between the segments separate the adjoining segments, to make the column flexible allowing a range of motion of the device. In device "On" configuration, cable is tensioned and the segments are pulled together to make the columns semi-rigid so that it can transfer the load from the shoulder pads to the waist belt.

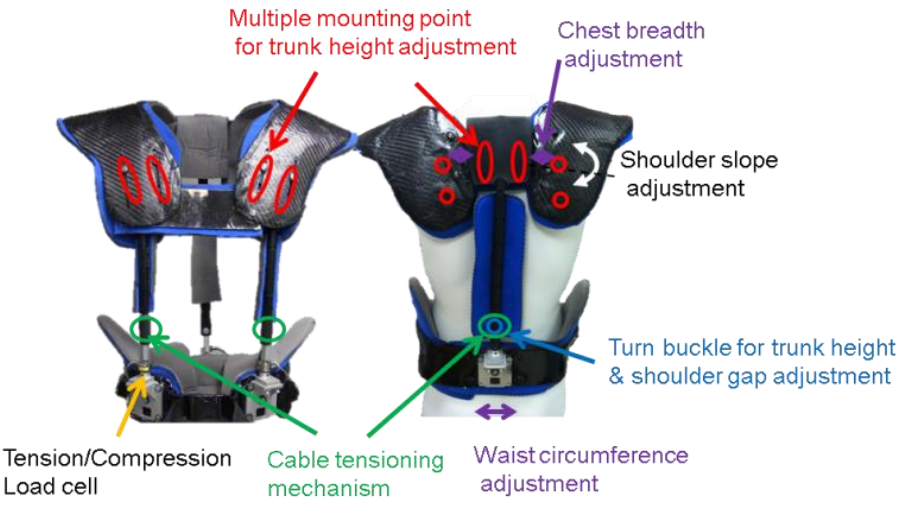

Figure A.1 Second Spine using the developed load bearing columns with added adjustability to accommodate different body shapes

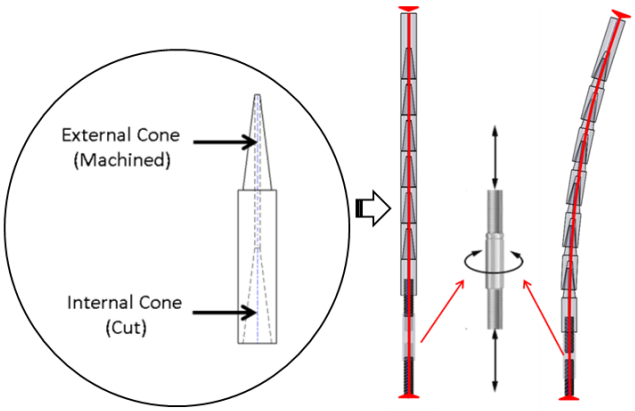

Cable:	No tension	Apply tension and lock
System:	Flexible	Becomes semi-rigid (support load)

Figure A.2 load bearing column design consists of cone-shaped joints that allows two stiffness configurations: semi-rigid ("On") and flexible ("Off")

Three different experiments were conducted to evaluate the two functionalities utilized in the Second Spine: providing a range of motion to the torso and transferring the load from the shoulders to the pelvis. The feasible range of torso motion in device "Off" configuration was

evaluated during a subject performing his maximum torso range of motion, with and without the device worn. Results show that approximately 70% of natural range of motion of torso was still achieved when the subject was wearing the device in its "Off" configuration, covering more than 30 degrees on each of trunk tilt, oblique and rotational degrees of freedom, Figure A.3 (top). Load transfer functionality of the device in its "On" configuration was evaluated using Instron® machine while the device was put on a manikin, for the static load condition (Figure A.3(middle)), and for the simulated walking condition (Figure A.3 (bottom)). For the static load condition, Instron machine applied vertical compressive load up to 1000 N while lateral deflection of the device and shoulder load were simultaneously measured using linear variable differential transformer (LVDT) and pressure sensors, respectively. Results showed that the device can successfully support up to 1000 N of vertical static load at which the 25% of applied load was measured on the manikin's shoulders, indicating a majority of load was directly transferred from the shoulders to the waist through the load bearing columns.

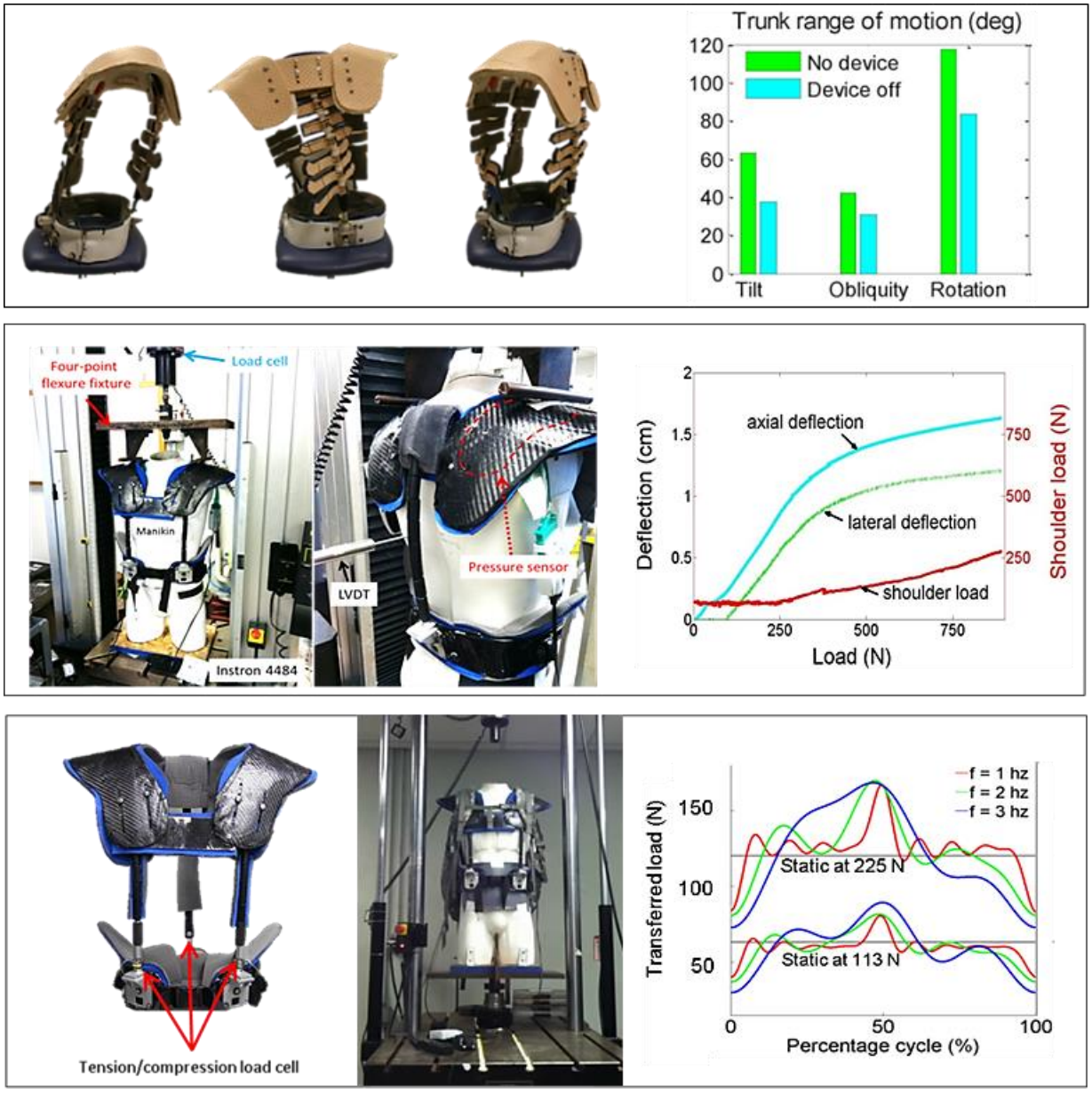

Figure A.3 (top) range of motion test in device "off" mode, (middle) static load test (0 to 1000 N) using Instron machine, and (bottom) simulated loaded walking test

The next evaluation was performed to measure the dynamic load transmission of the device in a simulated walking condition. Instron machine was used to generate base excitations similar to the pelvic vertical motion of human walking. The device was put on a manikin with the backpack placed on top of the device. Then, the manikin was fixed to the base of the Instron

machine where the base excitation was applied, Figure A.3 (bottom). Two different backpack loads were tested (113 N and 225 N), while Instron applied sinusoidal excitations to the base with 2 cm of amplitude for three different frequencies (1,2 and 3 Hz) to simulate three different walking speeds. Tension/compression load cell was mounted at the bottom of each column to measure the transmitted force from the shoulder pads to the waist belt. Load cell data were sampled at a frequency of 1 *kHz*, and post-processed with a low-pass filter (fourth order Butterworth, $f_c = 10$ *Hz*), averaged over cycle. About half of the applied load was *statically* transferred from the shoulders to the waist through the columns consistently for two load conditions and the base excitation indeed introduced dynamic load, in addition to the static load, as can be seen by the curves of both load conditions. The peaks of such dynamic loads increased with higher frequency and/or heavier mass. This implies that the magnitude of dynamic load in human load carriage will increase as the body's vertical acceleration increases. The results of these evaluations validate the two functions of the device: load transmission capability and accommodating a range of motion of torso.

Appendix B. Motorized Second Spine

A motorized Second Spine was designed that can actively modulate the vertical motion of a backpack aiming to reduce its dynamic loads. This is realized by real-time coordination of motor actuation in response to the waist vertical motion measured by an integrated motion sensor in such a way that the backpack is kept inertially stationary. The performance of this device was evaluated experimentally with an instrumented test-bed using an Instron machine, similar to evaluation done on Second Spine. Results shows that the backpack motion can be made nearly stationary with respect to the inertial frame (ground) by active modulation of motors by which the dynamic force can be minimized.

A backpack supported by the Second Spine during walking can be modeled as a mass undergoing harmonic excitation of the pelvis, $y(t) = Y \sin \omega t$. Since the connection between the mass and the moving base is rigid, motion of backpack x(t) is the same as motion of the pelvis, Figure B.1(a). The force transmitted to the pelvis R(t), therefore, is the sum of gravitational force and the accelerative force induced by pelvis vertical motion during gait. If an active component is imposed between the backpack and the waist belt, it can impose a motion to the backpack relative to the pelvis which is denoted as z(t), Figure B.1(b). Such a motion can be expressed as another sinusoidal function with controllable amplitude Z, frequency ω_z and phase ϕ. Then, the motion of backpack is the superposition of two motions, pelvic motion y(t) and the motor motion z(t). If the frequency of active component (ω_z) is preferably the same as that of pelvis (ω) to avoid the beat phenomena, the transmitted force can be explicitly expressed, Figure B.1(b). From this expression, it can be noticed that the amplitude of dynamic force is simply

$\omega^2 Y\sqrt{1+\left[\frac{Z}{Y}\right]^2+2\left[\frac{Z}{Y}\right]\cos\phi}$, which can be modulated by the amplitude ratio $\left(\frac{Z}{Y}\right)$ and the phase (ϕ) between the two motions. Simulation of force transmissibility $F_{a/b}$ (the ratio of transmitted force R between the Second Spine to the Motorized Second Spine) over different amplitude ratio and phase showed that the force transmitted to the pelvis can be less than that of rigid transmission (i.e., $F_{a/b} < 1$, below dashed line in Figure B.2) by modulating the phase of the backpack motion with respect to the pelvis motion between $5\pi/6$ and $7\pi/6$. Force transmissibility reaches its minima ($F_{a/b} = 0$) when $[Z,\phi] = [Y,\pi]$, indicating the dynamic force is minimized when z(t) has the same amplitude as that of pelvis vertical excitation with phase π (anti-phase). This simulation result provides the guideline for proper modulation of motor needed to reduce the dynamic force component with respect to the vertical motion of the pelvis.

	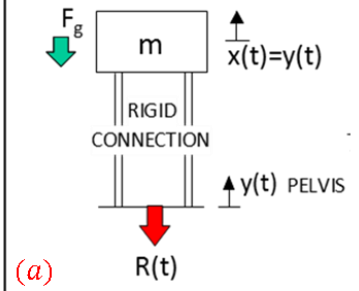	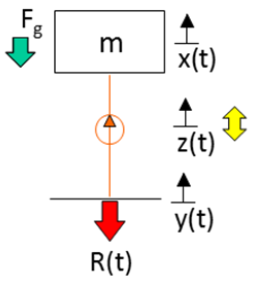
$x(t)$	$Y\sin\omega t$	$Y\sin\omega t + Z\sin(\omega_z t+\phi)$
$R(t)$	$m[g+\omega^2 Y\sin\omega t]$	$m\left[g+\omega^2\left\{Y\sqrt{1+\left[\frac{Z}{Y}\right]^2+2\left[\frac{Z}{Y}\right]\cdot\cos\phi}\right\}\sin(\omega t+\Phi)\right]$ where $\omega_z=\omega,\quad \Phi=tan^{-1}\left[\frac{Z\sin\phi}{Y+Z\cos\phi}\right]$

Figure B.1 schematics of (a) passive Second Spine model and (b) motorized Second Spine model

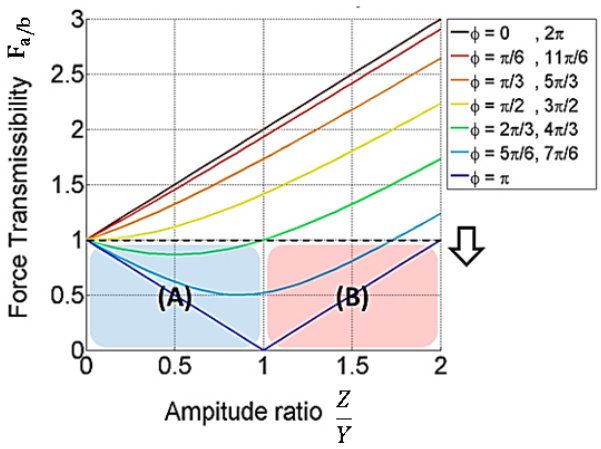

$$where\ \mathrm{F_{a/b}} = \frac{R_{(a)}}{R_{(b)}}$$

Figure B.2 simulation results of force transmissibility ($\mathrm{F}_{a/b}$) of motorized second Spine with amplitude ratio (Z/Y) for different phase values (ϕ)

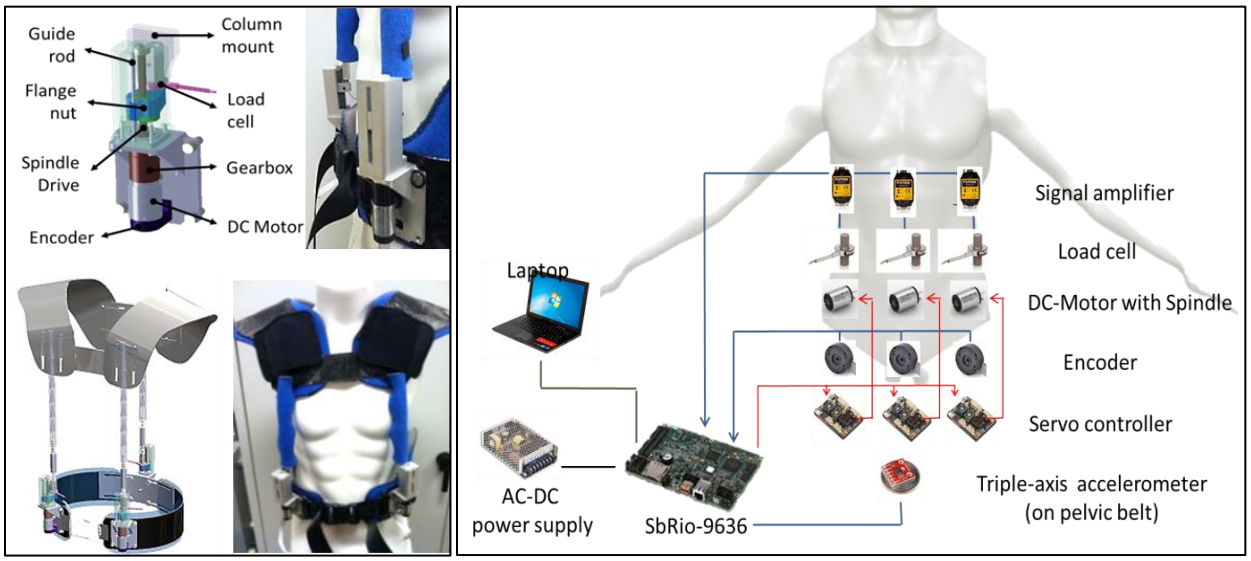

Figure B.3 (left) CAD and physical model of linear actuator and motorized Second Spine, and hardware configuration; (right) schematic of motion controller implemented in motorized Second Spine

The design of the Motorized Second Spine is shown in Figure B.3(left), and the hardware configuration is shown in Figure B.3(right). Implementation of motors, sensors, and real-time

controller on the Second Spine was carried out. The linear actuator was designed, fabricated, and placed on the pelvic belt that connects to the bottom of each load-bearing column. The tension/compression load cells are placed in between the motor and the column to measure the transmitted force. A tri-axis accelerometer is placed at the belt to measure the vertical acceleration of the pelvis during walking, Figure B.3(right). The measured acceleration is low pass filtered (Butterworth 4th order, fc = 5 *Hz*) to filter out the sensor noise then integrated twice to obtain the vertical displacement of the body. A Bessel high pass filter with a cut off frequency of 0.75 *Hz* is applied to discard the low frequency vertical displacement that is not generated by human motion and to avoid saturation over time. The controller then simultaneously actuates three motors using proportional-integral-derivative (PID) controller to negate this filtered displacement, which in turn, is expected to reduce the backpack motion in inertial frame, Figure B.4. The PID gains for each motor were tuned empirically during the instrumented test-bed testing.

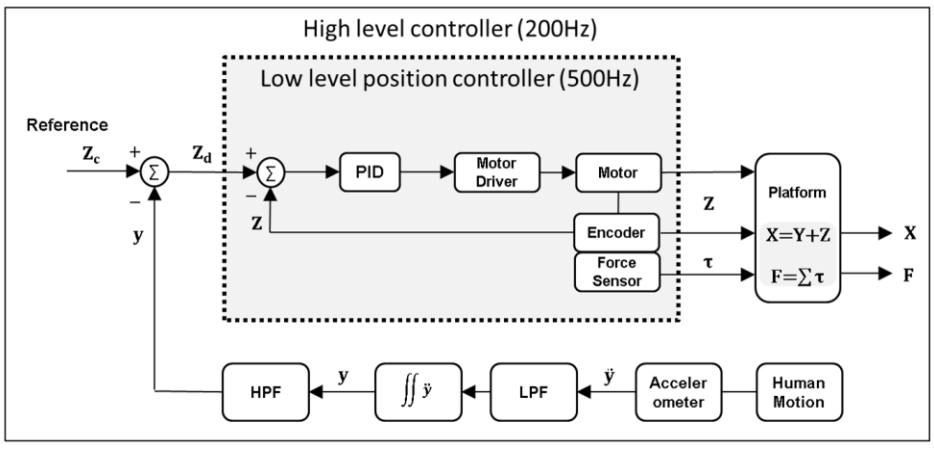

Figure B.4 Position controller implemented in the motorized Second Spine

The experiment evaluation on dynamic load compensation of the Motorized Second Spine was carried out through simulated test-bed using Instron® machine. Two linear variable differential transformers (LVDT) were mounted on Instron frame that simultaneously measure the vertical displacement of the base and the mass (on shoulder pads) relative to inertial frame Figure B.5. The device was mounted on the base and a 4.5kg mass was fixed on the top of the shoulder pads. This particular setting was used to prevent any unmodeled disturbances during experiment, such as friction between the device and the manikin or posterior load offset from a use of a backpack. Sinusoidal base excitation of 2 *Hz* frequency and 0.5 cm amplitude was simulated under three different configurations: motor-off ($z(t) = 0$), motor-on with anti-phase ($\phi = \pi$), motor-on with in-phase ($\phi = 0$). Figure B.6 plots the vertical displacement of the base and the mass with respect to the inertial frame and the force transmitted to the belt.

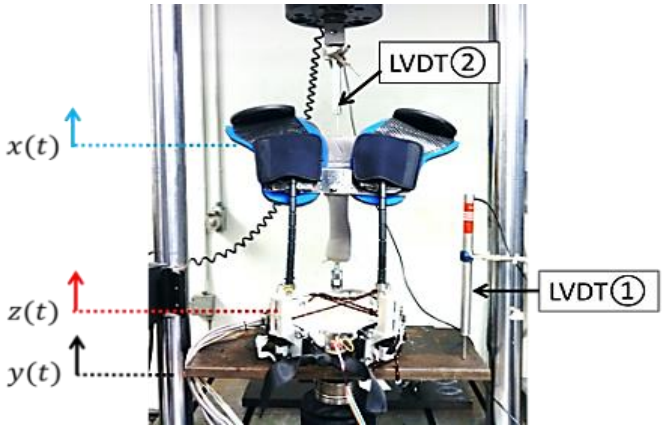

Figure B.5. Experiment setup of the Motorized Second Spine

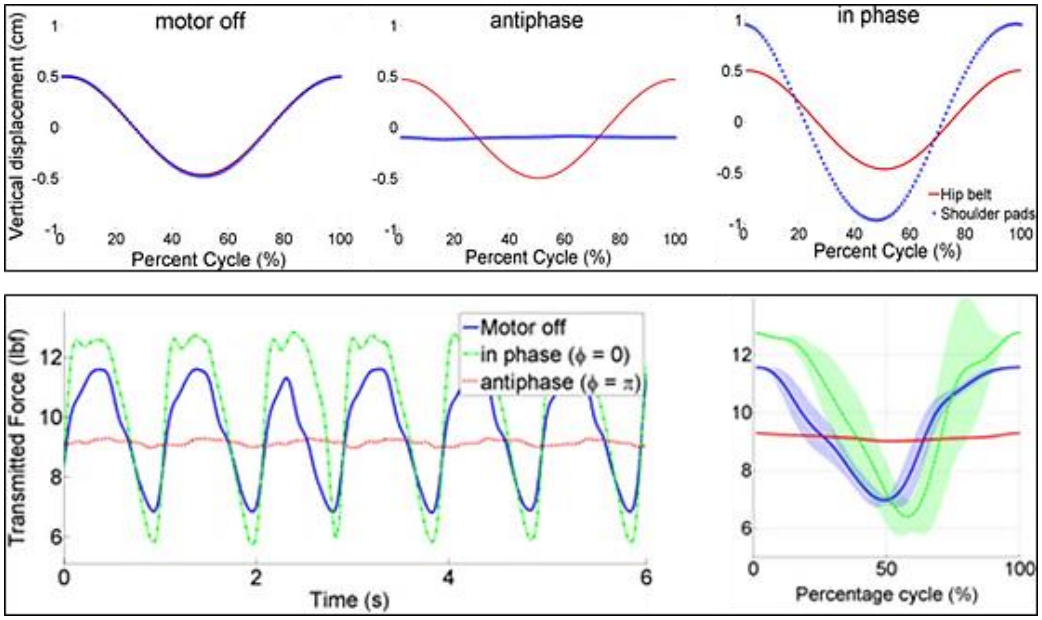

Figure B.6 (top) vertical displacement of the waist belt and the shoulder pads for three different configurations: motor-off, motor-on actuated anti-phase to the base motion, and motor-on actuated in-phase with the base motion; and (bottom) force transmitted to the waist belt corresponding to each configuration

Results on vertical displacement of three configurations showed that the motion of mass with respect to the inertial frame is the same for motor-off configuration, nearly stationary for motor-on with anti-phase configuration, amplified to double of the base motion for motor-on with in-phase configuration, Figure B.6 (top). This result validates that the controller can modulate the motion of the shoulder pads (corresponding to the backpack to which it is rigidly connected) nearly inertially stationary with respect to the ground, by controlling the motion of the motor anti-phase to the motion of the base with the same amplitude. The transmitted force measured from the load sensors in three configurations is in a good agreement to what we anticipated. In motor-off condition, dynamic force are induced which is reflected in the curves of the measured load synchronized with the base motion, Figure B.6 (bottom). In motor-on with anti-phase configuration, the amplitude of such curves is significantly attenuated indicating

reduction in dynamic forces transferred to the waist belt. In motor-on with in-phase configuration, the amplitude of curves is even higher than the motor-off configuration indicating the dynamic forces are increased due to the larger motion of mass than the motor-off configuration, which consequently generates higher acceleration of mass. These results validates the concept of dynamic load compensation by minimizing the motion of backpack with respect to the ground, by use of motors in the Motorized Second Spine that can actively modulate the backpack motion in response to the pelvic vertical motion.

Appendix C. Hardware specifications

Appendix C. 1 Hardware configurations of the Wearable upper Body Suit

The shoulder pads and load-bearing columns of the passive module were fabricated from a carbon fiber composite to meet the required stiffness to support up to 90 kg load. The cable actuator is comprised of a brushless EC motor, motor housing, and two Bowden cable mounts. It is a 100 W motor equipped with 111:1 planetary gearhead and a 5 cm diameter winch is connected to the motor shaft to reel in the cable. The nominal pulling force of the actuator is 371N @ 31cm/s and the maximum performance is 687N @ 13cm/s. The nominal current is 5.69A under 24V input. The motor is driven by a motor driver (ESCON 50/5, Maxon motor) which regulates the current to the motor based on the controller command. The micro controller (National Instrument, NI-myRio-1900) equipped with 667 *Mhz* dual core processor was used for real-time control on the cable force. It receives the sensor signals as a feedback and outputs the motor command based on the developed control law. It also has wi-fi communication through which the host computer (laptop) monitors the system and controls the motor wirelessly.

Load sensors (LTH300, Futek) are integrated at the end of the passive and active cables to measure the cable tension and strain gage amplifiers (CSG110, Futek) are paired with each load sensor to transmit the amplified signal from the sensors to the controller. A tri-axis accelerometer (ADXL335, Analog Devices, Norwood, MA) was attached to the belt and its axes aligned to the trunk coordinate frame to measure the vertical accelerations of the pelvis, Figure C.1 (d), from which the vertical velocity and displacement are also computed through integration. A DB15 connector is used to bundle the electric wires from the passive module and is connected to the active module via single 15-wire serial cable. This cable is used to power the sensors and

to accommodate the signal communications between passive and active module. Connecting/disconnecting of this cable is easily done in seconds. Sensor data, motor command, current draw, and other system parameters are logged in real time in a micro SD card at 200Hz frequency. The stored data are later synchronized with external biomechanical and physiological measurement devices (e.g., motion capture, electromyography, metabolic, etc.) for post-processing. A 7-cell Lithum polymer battery (25.9V, 9Ah) was used as a main power source to run all the electronics, except for the micro controller which uses a separate battery (7.4V 2Ah). It can provide power to continuously run the system up to three hours while outputting 70 Watt of assistive force into the passive module.

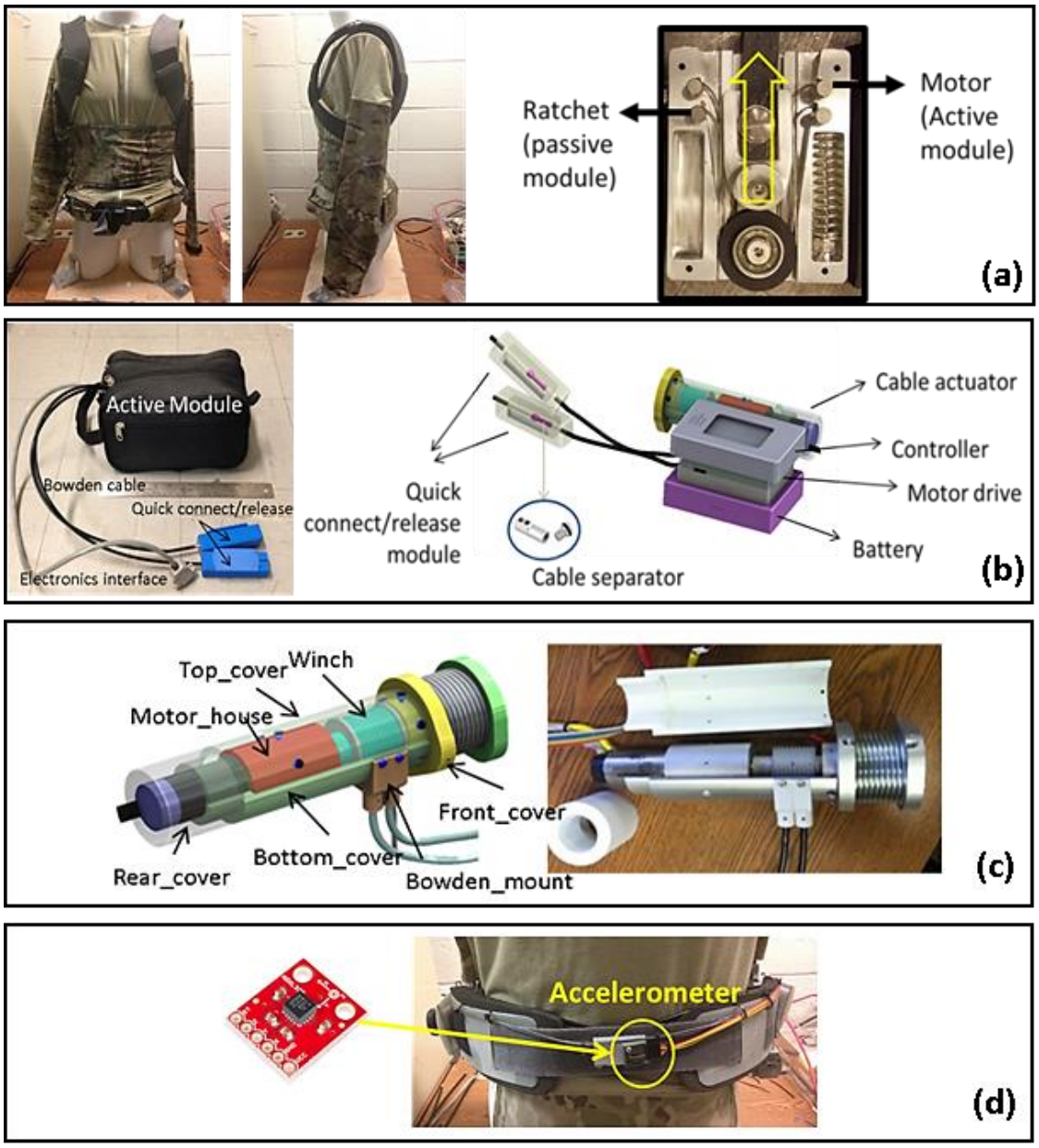

Figure C.1 (a) passive module and lifting mechanism, (b) active module, (c) cable actuator, and (d) accelerometer placed on the belt

Appendix C. 2 Hardware configurations of ROSE

Each ring of the ROSE is made using semi-rigid 0.25 cm fused deposition modeling (FDM) ABS, separated by a 4 cm gap in the neutral position. Each segment has a series of holes along the circumference at 10 increments. This allows flexibility in the placement of the actuator mounts which attach to some of the holes. The actuator mounts were also made from FDM ABS. The linear actuators are capable of a peak force of 50 N at speed of 16 mm/s with a 5 cm stroke length (Firgelli, L16-50-35-12-P). At the base of each actuator, a load cell (Futek, LCM200) and a conditioning board (Mantracourt, ICA6H) are mounted. Each actuator has a universal joint at the base and a spherical joint at the top. The brace is lined with plastazote polyethylene foam for comfort. The actuator's position feedback and load cell voltage are multiplexed and sent to the control board (National Instruments, sbRio-9626). The motors are driven at 12 V using a 1000Hz PWM signal through a small driver (Toshiba, TB6612FNG). A 5-cell Lithum polymer battery (18.5V, 2.2Ah) was used as a main power source to run all the electronics, except for the micro controller which uses a separate battery (7.4V 2Ah). It is capable of translating and rotating in 3 dimensions (maximum ±2 cm in translation and ±10 degrees in rotations). It also can exert 3 dimensional forces and moments (±100 N in forces and ±10 Nm in moments).

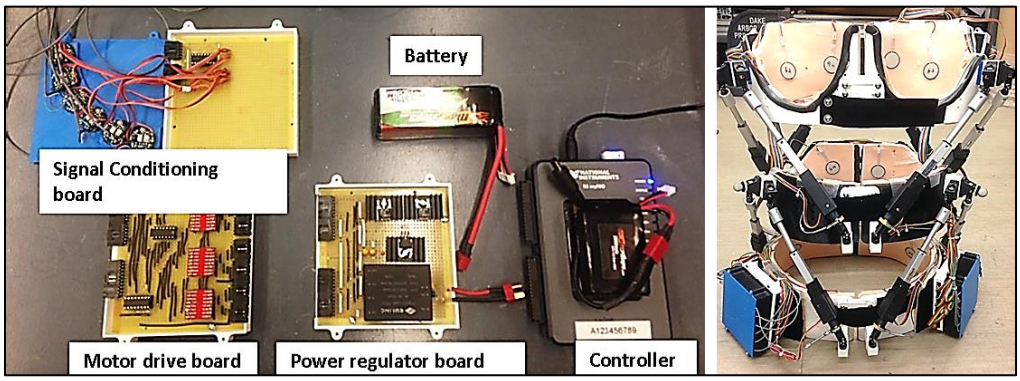

Figure C.2 Portable electronics development (right) and fully portable Robotic Spine Exoskeleton prototype (left)

Appendix D. Parameterization, kinematics, and trajectory planning of the ROSE

The Robotic Spine Exoskeleton consists of two parallel platforms connected in series. It has a total of twelve active degrees-of-freedom controlled by twelve linear actuators. The architecture of each parallel platform follows the kinematic structure of a 6-6 Stewart-Gough platform where all the limbs share identical kinematic chains of UPS, Figure D.1.

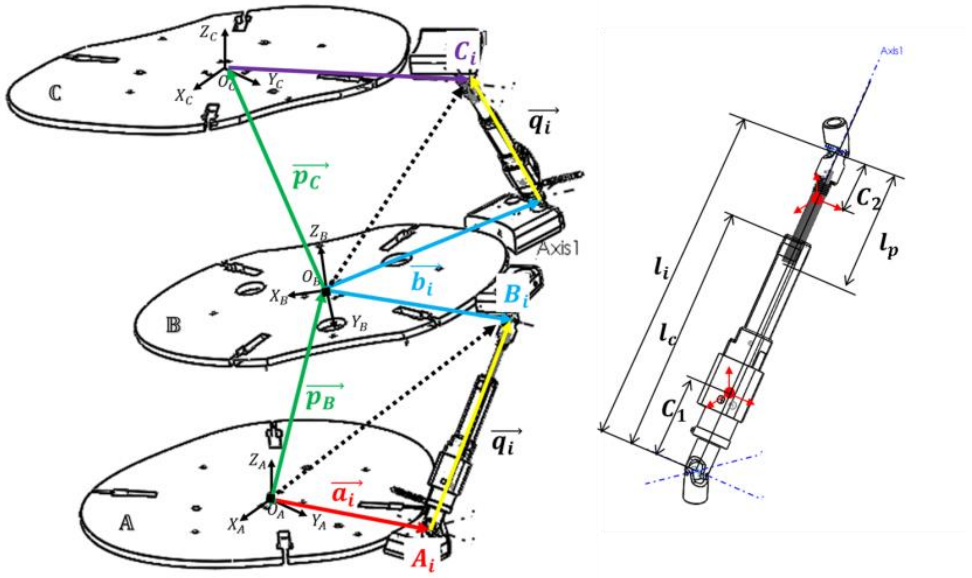

Figure D.1 Schematics of the robotic spine brace and model and the limb model

The parameterization and dynamics will be presented for only the lower parallel platform, which can also be extended to the top platform. Each limb connecting the fixed base $\mathbb{A}$ to the moving platform $\mathbb{B}$ forms a kinematic loop, which can be expressed in the vector form as

$$\mathbf{q_i} = \boldsymbol{P_B} - \boldsymbol{a_i} + R_B \boldsymbol{b_i}, \quad i = 1, \dots, 6$$

with $\mathbf{P_B} = [P_{Bx}, P_{By}, P_{Bz}]^T$ a position vector and R_B a rotation matrix formed by three rotation angles $(\psi_B, \theta_B, \phi_B)$. $\mathbf{q_i}$ is a vector with magnitude l_i, along a unit vector along the leg. $\mathbf{q} = [\mathbf{q_i}, \boldsymbol{q_2}, \dots, \boldsymbol{q_6}]^T$ is the vector of actuated joint coordinates and $\mathbf{X_B} = [P_{Bx}, P_{By}, P_{Bz}, \psi_B, \theta_B, \phi_B]^T$ is the vector of moving platform motion variables.

$$R_B = \begin{bmatrix} c\theta c\phi & s\psi s\theta c\phi - c\psi s\phi & c\psi s\theta c\phi + s\psi s\phi \\ c\theta s\phi & s\psi s\theta s\phi + c\psi c\phi & c\psi s\theta s\phi - s\psi c\phi \\ -s\theta & s\psi c\theta & c\psi c\theta \end{bmatrix}$$

is the rotation matrix relating the moving platform's coordinate system to the base coordinate system which is defined using pitch-roll-yaw angle rotations[1] where $s(\cdot)$ and $c(\cdot)$ stand for the sine and cosine of the argument, respectively. For inverse kinematic analysis, the moving platform position $\mathbf{P_B}$ and orientation R_B are given and the problem is to solve for the joint variables, $L = [l_1, l_2, \dots, l_6]^T$. The length of each limb l_i can be expressed as a norm of vector $\mathbf{q_i}$

$$l_i^2 = \boldsymbol{q_i^T q_i} = [\boldsymbol{P_B} - \boldsymbol{a_i} + R_B \boldsymbol{b_i}]^T [\boldsymbol{P_B} - \boldsymbol{a_i} + R_B \boldsymbol{b_i}]$$

Hence, each limb length can be uniquely determined for given position and orientation of the moving platform. For forward kinematic analysis, the joint variables l_i are given and the problem is to solve for X_B of the moving platform. In this study, an iterative numerical solver is used with screw axis representation of the rotation matrix [105, 106]. X_B is redefined with screw coordinates as

$$X_B = [P_{Bx}, P_{By}, P_{Bz}, s_x, s_y, s_z, \Theta]^T$$

in which s_x, s_y, s_z and Θ are obtained from rotation matrix as

[1] pitch-roll-yaw angle is defined as first rotation about fixed x axis by ψ, followed by rotation about fixed y axis by θ, followed by rotation about fixed z axis by ϕ

$$\Theta = \cos^{-1}\frac{r_{11} + r_{22} + r_{33} - 1}{2}, s_x = \frac{r_{32} - r_{23}}{2\sin\Theta}, s_y = \frac{r_{13} - r_{31}}{2\sin\Theta}, s_z = \frac{r_{21} - r_{12}}{2\sin\Theta}$$

where r_{ij} represents the i^{th} row and j^{th} column component of R_B. The seven equations to solve for forward kinematics are

$$\begin{cases} E_i = -l_i^2 + \boldsymbol{q_i^T q_i} = -l_i^2 + [\boldsymbol{P_B} - \boldsymbol{a_i} + R_B \boldsymbol{b_i}]^T [\boldsymbol{P_B} - \boldsymbol{a_i} + R_B \boldsymbol{b_i}] = 0, \ \ i = 1, \dots, 6 \\ E_7 = \hat{s} \cdot \hat{s} = s_x^2 + s_y^2 + s_z^2 = 1 \end{cases}$$

The nonlinear least-square optimization routines were used to minimize $\frac{1}{2}\sum_{i=1}^{7} E_i$. The multiplicity of the solution is resolved by iteratively comparing the solution to the one obtained from a previous step. If the error is within a prescribed threshold, that solution is chosen. The Jacobian matrices are computed from velocity loop closures which are directly obtained by differentiating the vector loop closure equation as follows

$$\dot{P_B} = \dot{q_i} - \omega_B \times R_B b_i \qquad for\ i = 1, \dots, 6$$

in which angular velocity ω_B of $\mathbb{B}$ with respect to $\mathbb{A}$ is

$$\omega_B = \begin{bmatrix} \omega_1 \\ \omega_2 \\ \omega_3 \end{bmatrix} = \begin{bmatrix} 1 & 0 & -s\theta \\ 0 & c\psi & s\psi c\theta \\ 0 & -s\psi & c\psi c\theta \end{bmatrix} \begin{bmatrix} \dot{\psi} \\ \dot{\theta} \\ \dot{\phi} \end{bmatrix}$$

The velocity of the end effector (or twist) defined as $\dot{\boldsymbol{X}}_{\boldsymbol{B}} = [\dot{P}_{Bx}, \dot{P}_{By}, \dot{P}_{Bz}, \omega_1, \omega_2, \omega_3]$ is mapped into the joint velocity vector by Jacobian as follows

$$\dot{\mathbf{q}} = \mathrm{J}\,\dot{\boldsymbol{X}}_{\boldsymbol{B}}, \quad J = \begin{bmatrix} \hat{q}_1^T & (b_1 \times \hat{q}_1)^T \\ \hat{q}_2^T & (b_2 \times \hat{q}_2)^T \\ \hat{q}_3^T & (b_3 \times \hat{q}_3)^T \\ \hat{q}_4^T & (b_4 \times \hat{q}_4)^T \\ \hat{q}_5^T & (b_5 \times \hat{q}_5)^T \\ \hat{q}_6^T & (b_6 \times \hat{q}_6)^T \end{bmatrix}$$

From the principle of duality of kinematics and statics [107, 108], the forces and moments applied at the end effector at static configuration are related to the joint forces required at the actuators to maintain the equilibrium by the transpose of the Jacobian matrix, under the assumption that the limb applies a force only along the limb axis. (The static wrench of the moving platform can be also obtained using Jacobian and applying principle of virtual work, assuming the limb applies a force only along the limb axis.)

$$\mathbf{F} = \mathrm{J}^{\mathrm{T}}\boldsymbol{\tau}$$

$$\begin{bmatrix} fx \\ fy \\ fz \\ Mx \\ My \\ Mz \end{bmatrix} = \begin{bmatrix} \hat{\mathrm{q}}_1 & \hat{q}_2 & \dots & \hat{q}_6 \\ b_1 \times \hat{q}_1 & b_2 \times \hat{q}_2 & \dots & b_6 \times \hat{q}_6 \end{bmatrix} \cdot \begin{bmatrix} \tau_1 \\ \tau_2 \\ . \\ . \\ . \\ \tau_6 \end{bmatrix}$$

in which $\boldsymbol{\tau} = [\tau_1, \tau_2, \dots, \tau_6]^T$ is the vector of forces experienced by the limbs (actuator force vector), and $\mathrm{F} = \left[\mathrm{F}_x, F_y, F_z, M_x, M_y, M_z\right]^T$ is the end effector wrench.

The trajectory planner is implemented to generate the desired motion, which employs a common trajectory generation method used in multivariable space [109]. Such computed trajectory describes the desired motion of moving platform for each degree-of-freedom in task space. A fifth-order polynomial curve-fitting method is used to generate the desired motion trajectories for all six pose variables that satisfy the six initial and final conditions: positions and

velocities at the initial and final times with continuities in acceleration, i.e., $\mathbf{X}(\mathrm{t}_0) = \mathbf{X}_0, \dot{\mathbf{X}}(\mathrm{t}_0) = \dot{\mathbf{X}}_0, \ddot{\mathbf{X}}(\mathrm{t}_0) = \ddot{\mathbf{X}}_0, \mathbf{X}(\mathrm{t}_\mathrm{f}) = \mathbf{X}_\mathrm{f}, \dot{\mathbf{X}}(\mathrm{t}_\mathrm{f}) = \dot{\mathbf{X}}_\mathrm{f}$ and $\ddot{\mathbf{X}}(\mathrm{t}_\mathrm{f}) = \ddot{\mathbf{X}}_\mathrm{f}$. Trajectory planning is implemented for each degree-of-freedom independently in the following manner:

$$\mathrm{X_i(t)} = \mathrm{a_{0_i}} + a_{1_i} t + a_{2_i} t^2 + a_{3_i} t^3 + a_{4_i} t^4 + a_{5_i} t^5$$

where **X(t)** is a position vector describing the positions and orientations of one ring with respect to the other ring. Substituting the initial and final constraints and its derivatives, six equations are obtained in a matrix form.

$$\begin{bmatrix} 1 & t_0 & t_0^2 & t_0^3 & t_0^4 & t_0^5 \\ 1 & t_f & t_f^2 & t_0^3 & t_0^4 & t_0^5 \\ 0 & 1 & 2t_0 & 3t_0^2 & 4t_0^3 & 5t_0^4 \\ 0 & 1 & 2t_f & 3t_0^2 & 4t_0^3 & 5t_0^4 \\ 0 & 0 & 2 & 6t_0 & 12t_0^2 & 20t_0^3 \\ 0 & 0 & 2 & 6t_0 & 12t_0^2 & 20t_0^3 \end{bmatrix} \begin{bmatrix} a_{0_i} \\ a_{1_i} \\ a_{2_i} \\ a_{3_i} \\ a_{4_i} \\ a_{5_i} \end{bmatrix} = \begin{bmatrix} X_{0_i} \\ X_{f_i} \\ \dot{X}_{0_i} \\ \dot{X}_{f_i} \\ \ddot{X}_{0_i} \\ \ddot{X}_{f_i} \end{bmatrix}, \qquad for\ i = 1 \cdots 6$$

The determinant of left most matrix is $4(\mathrm{t}_0 - t_f)^9$ thus this matrix is invertible provided $\mathrm{t}_0 \neq \mathrm{t}_\mathrm{f}$, from which a unique solution for the polynomial coefficients can be determined. Such coefficients can be further simplified if we consider the velocities and accelerations of all degrees of freedom at initial and final times are equal to zero (rest), i.e., $\dot{\mathrm{X}}_{\mathrm{o_i}} = \dot{\mathrm{X}}_{\mathrm{f_i}} = \ddot{\mathrm{X}}_{\mathrm{0_i}} = \ddot{\mathrm{X}}_{\mathrm{f_i}} = 0$ for $\mathrm{i} = 1 \ldots 6$, such that

$$\mathrm{X_i(t)} = \mathrm{X_{i\,0}} - 10\left(X_{i_0} - X_{i_f}\right)t^3 - 15\left(X_{i_0} - X_{i_f}\right)t^4 - 6\left(X_{i_0} - X_{i_f}\right)t^5$$

$$\dot{\mathrm{X}}_\mathrm{i}(t) = -30\left(X_{i_0} - X_{i_f}\right)t^2 - 60\left(X_{i_0} - X_{i_f}\right)t^3 - 30\left(X_{i_0} - X_{i_f}\right)t^4$$

$$\ddot{\mathrm{X}}_\mathrm{i}(t) = -60\left(X_{i_0} - X_{i_f}\right)t - 180\left(X_{i_0} - X_{i_f}\right)t^2 - 120\left(X_{i_0} - X_{i_f}\right)t^3$$

Using above equations, task space motion trajectories are generated based on the given desired initial and final pose of the platform.

Appendix E. In vitro spine stiffness measurement and its implication

There have been a number of studies conducted to experimentally investigate the stiffness of the spinal motion segments, consisting of two vertebrae connected with intervertebral disk. Though the stiffness of the spine motion segment may not have direct implication on the torso stiffness, we hypothesize that there is a correlation between the stiffness of two bodies as one (spine) is a sub-part of the other body (torso). Moreover, spine is presumably stiffer than any of other soft tissues and muscles surrounding the spine, knowing the material properties and stiffness characteristics of the torso would provide an insight into the spine stiffness since the spine may have significant contribution to the overall characteristic of the torso stiffness.

The human spine has a very distinct feature compared to other skeletal structures in the human body. It is comprised of a series of intervertebral joint (disk) which has all six degrees-of-freedom capability and are interconnected by vertebrae, ligament, and muscles which all has different stiffness characteristics. It also exhibits visco- and poro- elastic properties, which are time, force, and pose dependent. Because of these properties it is hard to obtain the accurate model of the spine mathematically. Therefore, the stiffness of the spine vertebrae was typically obtained experimentally from a load-displacement measurement [100, 110, 111, 112, 113]. The direct measurement of spinal motion segment stiffness matrix with all six degrees of freedom taken into account has been only realized recently from the work presented in [114] by designing a Stewart-platform type test machine that can displace the upper end of the spinal motion segment to any specified 6-DOF position relative to the immobilized lower vertebra, Figure E.1(left). The use of 6-DOF load cell attached to the upper end of the specimen made it possible for the load-displacement measurement for all 6 DOF. Similar test-bed was developed by [102],

a dynamic, six-axis spine simulator that consists of independently controlled mechanism that allows translation along and rotation about each of the three dimensional axis Figure E.1(right). The stiffness coefficients are typically determined using a linear regression (least-squares method) of the load-displacement measurements.

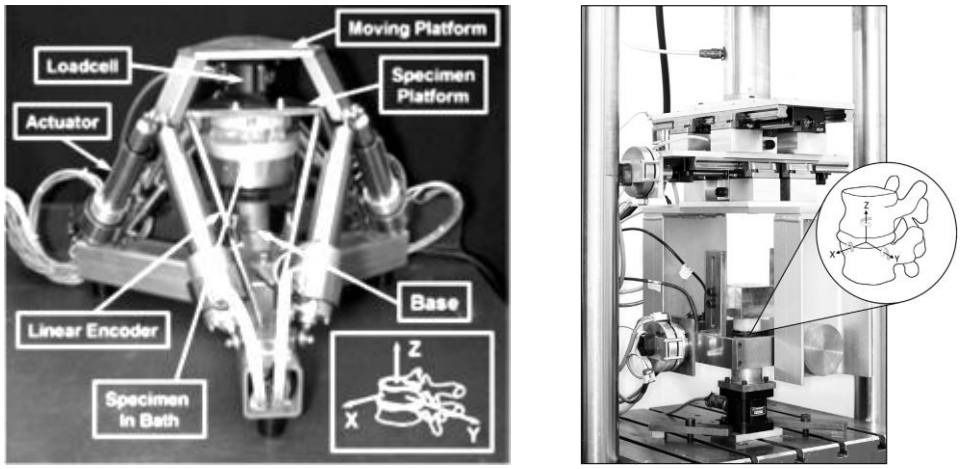

Figure E.1 (left) A "hexapod" spine testing machine developed by Stokes *et al*. [114], and (right) a dynamic six-axis spine simulator developed by Holsgrove *et al*. [102]

Each coefficient comprising the stiffness matrix can be interpreted as either the translation or rotation about the coordinate axis in response to the single dimensional force (either force or moment). Such a displacement response is not only a function of the magnitude and direction of the applied force, but also the point of application as well. It has been a common experimental setting to match the point of force (or displacement) application to the geometric center of the cross section of the intervertebral disk such that the six-dimensional stiffness is calculated at the vertebra center. The three-dimensional motion behavior of the human spine was studied by static analyses with a geometric model of the spine and inter-vertebra discs [102, 103].

Goel have used the term "primary (or principal or major)" motion to indicate the two displacement response (linear and angular displacement) of the spine in the plane of the applied

load while the other four motions are denoted as "secondary (or minor or coupled)" [111]. For example, the primary motions subjected to the force along positive y axis (+Fy) are a translation along positive y axis (+Ty) and rotation about x axis (-Rx) while the secondary motions are the other four out-of-plane motions namely Tx, Tz, Ry, Rz. This behavior corresponds to the model depicted in Figure E.2(a), wherein the spine is considered as a simplified truss structure that is fixed at the center of the bottom vertebrae in all directions subjected to the external force at the center of the top vertebrae. Later studies done by Gardner-Morse *et al.* [98] developed more realistic model that consisting of a truss (vertebra) and a shear beam (motion segment) with a rigid posterior offset δ. Such a model was used to identify several primary off-diagonal axis terms of stiffness matrix which are inherited by the effects of added beam that is posteriorly offset to the truss, e.g., anterior-posterior shear translation (Fy) and flexion/extension rotation (Mx) due to the applied axial force (Fz). These spine models can be adopted to study the load-displacement relationship of the torso due to the similarity in their structural composition: muscles and soft tissues analogous to intervertebral disk as a truss structure, and the spine analogous to motion segment (facet joints, ligaments, and tendons) as a beam structure, Figure E. 2(b).

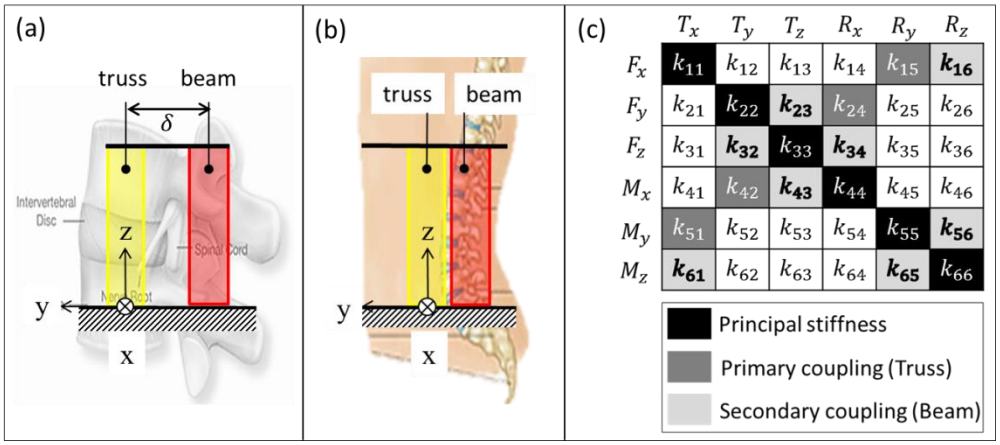

Figure E.2 (a) spine vertebrae modeled as an equivalent truss/beam structure; (b) human torso model as an equivalent truss/beam structure analogous to (a); and (c) A 6x6 stiffness matrix

In earlier research on spine motion segment stiffness analyses, people have assumed that the stiffness matrix is symmetric under the assumption of the conservation of energy and linear elasticity [100, 110, 111, 112, 113, 114, 115, 116, 117]. Such an assumption reduces the number of independent stiffness coefficient from 36 to 21. Some studies have also assumed the symmetrical behavior about the sagittal plane at which the number of independent stiffness coefficient is even more reduced from 21 to 12 [100, 99]. The nine terms that become zero under this sagittal plane symmetry assumption are the forces associated with the displacements within the sagittal plane, e.g., no lateral force ($k_{13} = k_{31} = 0$), no coronal lateral bending rotation ($k_{35} = k_{53} = 0$) associated with axial compression. Although a great amount of research has been done to experimentally characterize the stiffness of the spinal segments, it is only recent that the non-conservative nature of the spine motion segment was validated in vitro that have led to obtain the non-symmetric stiffness matrix [97, 118, 102, 103]. The non-conservative nature of the joint caused by the loss of energy due to poro- and visco- elastic effects of the disc, facet joints, and ligaments was first considered in [118] where the stiffness matrix obtained was non-symmetric. The stiffness matrices obtained in [97, 118, 102, 103] were also not symmetrical

about the diagonal stiffness, which was controversial to the symmetric assumption that had governed in many earlier studies. The presence of non-conservative forces and moments cannot ensure the symmetry of the stiffness matrix, which is well known in structural dynamics (explained in next paragraph). Based on the previously established theory on spine force-motion behavior applied onto the model considered in Figure E.2 (b), each stiffness matrix term can be interpreted in a more physical sense.

Asymmetric property of stiffness matrix

In a linear elastic conservative system, the stiffness matrix is symmetric on the basis of Maxwell's Reciprocity Theorem[2], which states that the displacement at point i due to a unit load at another point j is equal to the displacement at j due to a unit load at i. Infinitesimal strain theory also supports the symmetric property of the stiffness matrix, which states that the constitutive properties of the material (stiffness) at each point of space can be assumed to be unchanged by the deformation. Maxwell's Reciprocity Theorem guarantees existence of potential function Φ for the conservative vector field $F(\Delta x, \dots \Delta\phi)$ such that $\nabla\Phi(\Delta x, \dots \Delta\phi) = F(\Delta x, \dots \Delta\phi)$. Potential function is continuous and continuously differentiable function which should obey under the Maxwell's Reciprocity, $\frac{\partial}{\partial X_i}\left(\frac{\partial \Phi}{\partial X_j}\right) = \frac{\partial}{\partial X_j}\left(\frac{\partial \Phi}{\partial X_i}\right)$. Each element of stiffness matrix has the form of $K_{ij} = \frac{\partial^2 \Phi}{\partial X_i \partial X_j}$ and using the above relation, we have $K_{ij} = K_{ji}$, i.e., matrix is symmetric. However, if the system is non-linear elastic and/or non-conservative, the Maxwell's Reciprocity Theorem is not applicable from which, consequently, the symmetric property of the stiffness matrix is no longer guaranteed.

[2] Maxwell's Reciprocity Theorem states that the displacement at point i due to a unit load at another point j is equal to the displacement at j due to a unit load at i.